17th International Workshop on Seismic Anisotropy, Expanded Abstracts

Table of Contents

17th International Workshop on Seismic Anisotropy

_____

Session 5 – Rock Physics and Attenuation

Session 6 – Modeling, Velocities and Imaging

Muir-Dellinger parameters for analysis of anisotropic signatures

Yanadet Sripanich[1], Sergey Fomel[1], Paul Fowler[2], Alexey Stovas[3], and Kyle Spikes[1]
[1] *The University of Texas at Austin* , [2] *Fowler Geophysical Consulting* , [3] *NTNU*

SUMMARY

We revisit the Muir-Dellinger (MD) anisotropic parameterization and conduct its analysis based on several criteria for good anisotropic parameterization. Our results suggest that MD parameters represent an attractive parameterization for studies on qP waves and inversion of anisotropic parameters under these criteria. Additionally, MD parameters exhibit a strong linear relationship that depends on lithology.

MUIR-DELLINGER ANISOTROPIC PARAMETERS

Thomsen parameters (Thomsen, 1986) are commonly adopted for studying seismic anisotropy in VTI media and represent combinations of stiffness coefficients, believed to govern the most important anisotropic signatures. An extension of Thomsen parameters to orthorhombic media proposed by Tsvankin (1997) has an undesirable property of strong variance due to different choices of coordinate labeling (Fowler, 2015), which results from its emphasis on the vertical symmetry axis for a stack of thin beds. This may not be optimal for orthorhombic media in which all three symmetry axes are of equal importance. Several other schemes are discussed by Sripanich et al. (2016). In general, good anisotropic parameters should have a clear physical meaning and allow complex formulas of wave attributes to be expressed in a concise manner with the complexity hidden inside the notation. Other important features may also include easy pseudoacoustic simplifications for qP waves, straightforward extension to orthorhombic media, and relative orthogonality for parameter estimation.

In this paper, we consider an alternative set of anisotropic parameters that addresses the aforementioned requirements for good parameterization. The basis for our construction is the Muir-Dellinger (MD) parameters, originally proposed by Muir and Dellinger (1985) and extended to TI media by Fomel (2004) and orthorhombic media by Sripanich and Fomel (2015). In 2D case suitable for the analysis of qP waves in TI media, the set consists of four parameters: $w_1 = c_{11}$, $w = c_{33}$, q_1, and q_3. The first two parameters constitute the qP-wave velocity squared along the horizontal (n_1) axis and the vertical (n_3) axis. The remaining two (q_1 and q_3) are anelliptic parameters that govern the deviation from an elliptical phase velocity and are defined as follows:

$$q_1 = \frac{c_{55}(c_{11} - c_{55}) + (c_{55} + c_{13})^2}{c_{33}(c_{11} - c_{55})} , \qquad (1)$$

$$q_3 = \frac{c_{55}(c_{33} - c_{55}) + (c_{55} + c_{13})^2}{c_{11}(c_{33} - c_{55})} . \qquad (2)$$

They can be found from fitting the velocity curvatures along the horizontal (n_1) axis and the vertical (n_3) axis as denoted by the subscript. Their straightforward extension to orthorhombic media has similar definitions with appropriate changes in indices (Sripanich and Fomel, 2015). Under MD parameters, the exact phase velocity of qP waves in VTI media is given by (Sripanich and Fomel, 2015):

$$
\begin{aligned}
v_{qP}^2(\theta) = {} & \frac{1}{2}(w_1 \sin^2\theta + w_3 \cos^2\theta + \tau) + \\
& \frac{1}{2}\sqrt{(w_1 \sin^2\theta + w_3 \cos^2\theta - \tau)^2 + 4w_1 w_3 \lambda \sin^2\theta \cos^2\theta} ,
\end{aligned} \qquad (3)
$$

where θ is the phase angle measured from the vertical axis

$$\tau = \frac{(q_1 - q_3)w_1 w_3}{w_3(q_1 - 1) - w_1(q_3 - 1)} \quad \text{and} \quad \lambda = \frac{(q_1 - 1)(q_3 - 1)(w_3 - w_1)}{w_3(q_1 - 1) - w_1(q_3 - 1)} .$$

Assuming $q_1 = q_3$ results in $\tau = 0$ and $\lambda = q_1 - 1 = q_3 - 1$ and reduces equation 3 to the pseudoacoustic approximation studied by Alkhalifah (1998). Therefore, pseudoacoustic approximation is equivalent to setting $q_1 = q_3$ under MD parameterization, which implies equal phase velocity curvatures along vertical and horizontal axes.
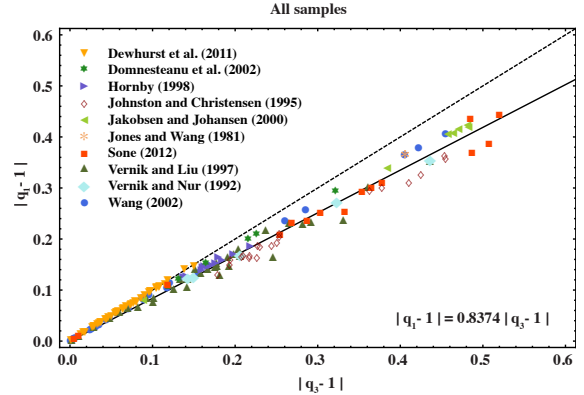
Figure 1: Plot of the linear relationship (equation 4) between q_1 and q_3 from shale samples. The dashed line denotes the line of slope = 1. Similar plots are observed for sandstones and carbonates (Sripanich and Fomel, 2015).

THE EMPIRICAL LINEAR RELATIONSHIP

Instead of using $q_1 = q_3$ as suggested by the pseudoacoustic approximation, Sripanich and Fomel (2015) showed that there existed a strong linear correlation (Figure 1) between q_1 and q_3 found from laboratory measurements on stiffnesses (c_{ij}) in TI media for different rock samples. This correlation can be used to reduce the number of dependent parameters in velocity approximations for qP waves while still maintaining a high level of approximation accuracy (Sripanich and Fomel, 2015). The empirical linear relationship between q_1 and q_3 takes the form

$$q_1 - 1 = s\,(q_3 - 1) , \qquad (4)$$

Muir-Dellinger anisotropic parameters

which can be translated to an equivalent expression

$$\frac{v_{S0}^2}{v_{P0}^2} = \frac{(s-1)(1+2\varepsilon)}{s-(1+2\varepsilon)}, \qquad (5)$$

where v_{S0} and v_{P0} denote the verical qS and qP velocities respectively and $s = (1-c_{55}/c_{33})/(1-c_{55}/c_{11})$. Figure 1 shows the plot of equation 4 with the data from various laboratory measurements in the literature (e.g, Johnston and Christensen, 1995; Vernik and Liu, 1997; Hornby, 1998; Jakobsen and Johansen, 2000; Wang, 2002; Dewhurst et al., 2011). An analogous linear trend was observed for samples of other rock types including sandstones and carbonates (Sripanich and Fomel, 2015). Equations 4 and 5 suggest possible use of this empirical linear relationship for reduction in parameter number in any expression of different anisotropic signatures, for prediction of ε or other parameters related to the horizontal direction from information in the vertical direction, and for further insight to the degree of subsurface anisotropy from the deviation of slope value from one.

Figures 2 shows a comparison of resultant slope values computed from self-consistent rock physics modeling (SCA) and Backus averaging for a synthetic shale. The slope values vary in a small amount despite a significant variation in mineral composition. Moreover, both methods also produce results with similar variational trends. These outcomes partially validate the global linear trend observed empirically in Figure 1 based on measurements from different shale samples that were subjected to various conditions in the lab.
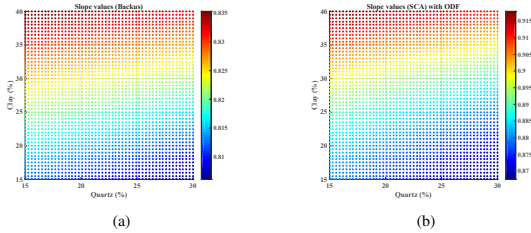

Figure 2: Comparison between resultant slope values from a) Backus averaging and b) SCA based on a synthetic shale. A general trend is observed in the change of slope values with the change in mineral proportions.

SENSITIVITY ANALYSIS

To compare relative orthogonality of different parameterizations, Sripanich et al. (2016) proposed to apply the general formula of a resolution matrix, which is an approximation to the Hessian of the linearized inversion of phase velocity squared, with respect to different parameterizations and therefore, an approximation to the inverse covariance matrix for these parameters. One indicator of a well-behaved parameterization is a small condition number of the Hessian, which corresponds to the smallest ratio of largest and smallest eigenvalues ($\lambda_{max}/\lambda_{min}$). As indicated in Figure 3, among four different parameterizations, the optimal parameterization associated with the smallest condition number is the Muir-Dellinger scheme.
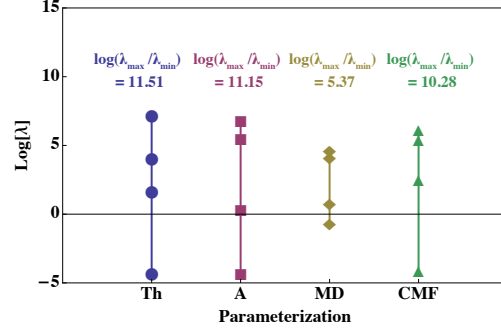
Figure 3: Distribution of eigenvalues of the sensitivity matrix for qP phase velocity in Greenhorn shale TI model. The plot indicates that MD has the lowest condition number.

REFERENCES

Alkhalifah, T., 1998, Acoustic approximations for processing in transversely isotropic media: Geophysics, **63**, 623–631.

Dewhurst, D. N., A. F. Siggins, J. Sarout, M. D. Raven, and H. M. Nordgård-Bolås, 2011, Geomechanical and ultrasonic characterization of a Norwegian Sea shale: Geophysics, **76**, no. 3, WA101–WA111.

Fomel, S., 2004, On anelliptic approximations for qP velocities in VTI media: Geophysical Prospecting, **52**, 247–259.

Fowler, P., 2015, Some pitfalls in orthorhombic parameter estimation: 85th Meeting Expanded Abstracts, SEG, 493–497.

Hornby, B. E., 1998, Experimental laboratory determination of the dynamic elastic properties of wet, drained shales: Journal of Geophysical Research, **103**, 29945–29964.

Jakobsen, M., and T. A. Johansen, 2000, Anisotropic approximations for mudrocks: A seismic laboratory study: Geophysics, **65**, no. 6, 1711–1725.

Johnston, J. E., and N. I. Christensen, 1995, Seismic anisotropy of shales: Journal of Geophysical Research, **100**, 5991–6003.

Muir, F., and J. Dellinger, 1985, A practical anisotropic system: SEP, **44**, 55–58.

Sripanich, Y., and S. Fomel, 2015, On anelliptic approximations for qP velocities in transversely isotropic and orthorhombic media: Geophysics, **80**, no. 5, C89–C105.

Sripanich, Y., S. Fomel, and P. Fowler, 2016, A comparison of anisotropic parameterizations for TI and orthorhombic media and their sensitivity with respect to qP velocities: Presented at the 86th Meeting Expanded Abstracts, SEG. (Accepted).

Thomsen, L., 1986, Weak elastic anisotropy: Geophysics, **51**, 1954–1966.

Tsvankin, I., 1997, Anisotropic parameters and P-wave velocity for orthorhombic media: Geophysics, **62**, 1292–1309.

Vernik, L., and X. Liu, 1997, Velocity anisotropy in shales: A petrophysical study: Geophysics, **62**, no. 2, 521–532.

Wang, Z., 2002, Seismic anisotropy in sedimentary rocks, Part 2: Laboratory data: Geophysics, **67**, no. 5, 1423–1440.

S-waves normal moveout velocity ellipse in vicinity of the singularity point in tilted ORT media

Yuriy Ivanov* and Alexey Stovas, Norwegian University of Science and Technology

SUMMARY

Quasi shear wave propagation in orthorhombic media is complicated by the existence of so-called point singularities – the points where slowness surfaces of the split shear waves cross each other. In vicinity of these points, the slowness surfaces have a conical shape. In tilted orthorhombic (TOR) medium, the point singularities can occur along the vertical, distorting the traveltime parameters that are defined at zero-offset. We analyze the influence of the singularities on the normal moveout (NMO) velocity ellipse by analyzing the second order derivatives of the slowness surface. Using numerical model, we demonstrate how the NMO ellipses of the split S-waves are affected by the singularity.

INTRODUCTION

Crampin (1981) showed that there should exist at least one point singularity in one of the symmetry planes of an orthorhombic medium. In the vicinity of the singularity, slowness surfaces of both S-waves have anomalous curvature, and polarization directions can change rapidly. Many publications address the issue of the point-singularities in orthorhombic and lower symmetry anisotropic media (Crampin, 1991; Brown et al., 1993; Grechka and Obolentseva, 1993; Vavryuk, 2001). We address the practically important situation when the symmetry planes of the orthorhombic medium are tilted such a way the singularity point is moved close to the vertical axis. In this case, the behavior of the NMO ellipse (Grechka and Tsvankin, 1998) complicates a lot leading to the ellipse degeneration.

THEORY

In horizontal homogeneous anisotropic layer, the series for the one-way traveltime squared with respect to the horizontal offset projections x and y expressed through the offset r along the azimuth α (the source is located at the origin) read

$$t^2(r,\alpha) = t_0^2 + \frac{r^2}{V_{nmo}^2(\alpha)} + ..., \qquad (1)$$

where radial offset r is calculated from the traveltime surface apex at (x_0, y_0), α is the azimuth along which (with respect to the apex) the one-way traveltime is measured, t_0 is the one-way traveltime at the apex, $V_{nmo}^2(\alpha)$ is the NMO ellipse (Grechka and Tsvankin, 1998). The NMO ellipse is obtained from the derivatives of the vertical slowness with respect to the horizontal slownesses evaluated at zero horizontal slownesses, and it can be explicitly obtained from the Christoffel equation. We use the following notation for the derivatives $q_{ij}^{(N)}$, $N = S1, S2$ of the Nth wave mode:

$$q_{ij}^{(N)} = \frac{1}{(i+j)!} \frac{\partial^j}{\partial p_2^j} \frac{\partial^i}{\partial p_1^i} p_3^{(N)}\bigg|_{p_{1,2}=0}, \quad i,j \geq 0, \qquad (2)$$

where $\mathbf{p}^{(N)} = (p_1, p_2, p_3^{(N)})^T$ is the slowness vector of the wave mode under consideration. In order to obtain the TOR medium, we rotate the slowness surface in the orthorhombic medium at three Euler angles: the azimuth ϕ, the tilt θ, and the azimuth ψ (Lapilli and Fowler, 2013). The azimuth ϕ controls the orientation of the ellipse and not its shape, hence we set $\phi = 0$. In terms of traveltimes, the zero order derivative q_{00} controls the value t_0 at the apex of the traveltime surface, the first-order derivatives q_{10} and q_{01} control the position of the apex ($x_0 = -z q_{10}$, $y_0 = -z q_{01}$), and the second-order derivatives q_{20}, q_{11}, and q_{02} control the NMO-ellipse. We distinguish the wave modes based on their velocity along the vertical in unrotated ORT medium: $V_{S1} = \sqrt{c_{55}}$ and $V_{S2} = \sqrt{c_{44}}$, where c_{44} and c_{55} are the corresponding stiffness coefficients of the orthorhombic (before the rotation) medium.

If the TOR symmetry planes are rotated such a way that singularity point is moved close to the vertical, the behavior of the NMO ellipse complicates a lot, leading to the ellipse degeneration. In terms of the derivatives q_{ij}, the occurrence of the S-wave singularity in the vicinity of the vertical axis leads to:

1. The S-waves zero-order coefficients are getting close in value: $\left| q_{00}^{(S1)} - q_{00}^{(S2)} \right| \to 0$.

2. First-order coefficients $q_{10}^{(N)}$ and $q_{01}^{(N)}$ undergo an abrupt change, and reach infinity at the singularity point.

3. Values of the second order coefficients $q_{20}^{(N)}$ and $q_{02}^{(N)}$ sharply increase reaching the infinity at the singularity point. Value of the mixed derivative $q_{11}^{(N)}$ changes abruptly and reaches infinity if the singularity occurs outside the symmetry planes, and zero if it occurs in one of the symmetry planes.

4. The NMO ellipses of both S-waves do not exist at the singularity. However, in the vicinity of the singularity, the S2-wave NMO-ellipse degenerates into hyperbola and the S1-wave NMO ellipse preserve its elliptical shape although it is elongated along one of the semi-axes.

As can be seen from above, due to discontinuity in solutions for $q_{00}^{(N)}$ through a singularity point, derivatives $q_{ij}^{(N)}$ are not defined at the singularity. The singularity points can be located in (θ, ψ)-space (there is no dependence of $q_{00}^{(N)}$ on angle ϕ). At the singularity point, the discriminant $\Delta(\theta, \psi)$ in bi-cubic equation for q_{00} is equal to zero. In a sense, $\Delta(\theta, \psi)$ is a measure of closeness of the two solutions of the cubic equation.

In order to analyze the concaveness of the slowness surface in vicinity of the singularity points, we calculate the Gaussian curvature $K_p(\theta, \psi)$. The curve $K_p(\theta, \psi) = 0$ separates the hyperbolic $K_p < 0$ and elliptical $K_p > 0$ areas of the slow, S2-wave, slowness surface. Hyperbolic area corresponds to concave part of the slowness surface, and the NMO-ellipse in this area is degenerate. The Gaussian curvature of the fast, S1-wave, slowness surface is always positive in the vicinity of

S-waves NMO ellipse in vicinity of the singularity points in TOR

the singularity (apart from situations when there exist triplications), and it can reach high values due to high curvature of the slowness surface. At the singularity point, the Gaussian curvature of both waves is infinite due to discontinuity of the $q_{00}^{(N)}$. We should further refer to the Gaussian curvature K_p as that of the S2-wave. For the numerical tests we use the values of the density normalized stiffnesses (in $km^2 s^{-2}$) of the Phenolic CE, taken from Brown et al. (1993): $c_{11} = 12.8$, $c_{22} = 11.3$, $c_{33} = 8.6$, $c_{44} = 2.3$, $c_{55} = 2.6$, $c_{66} = 2.8$, $c_{12} = 5.3$, $c_{23} = 4.7$, and $c_{13} = 4.9$. This model contains a point singularity in the $[x, z]$ plane at $\theta \approx 64°$. For this model, the curve $K_p = 0$ and the corresponding region in the $[x, y]$-plane are shown in Figure 1.
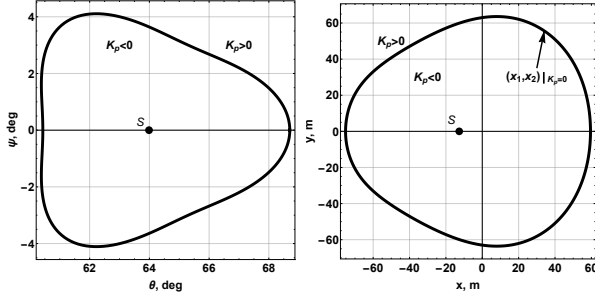

Figure 1: The curve $K_p(\theta, \psi) = 0$ (left) and a corresponding region of the positions of the extremum of the traveltime surface (right).

The second order derivatives of the slowness surfaces calculated as a function of θ in the vicinity of the singularity point are shown in Figure 2. At the singularity ($\theta \approx 64°$, $\psi = 0$), both $q_{20}^{(N)}$ and $q_{02}^{(N)}$ are discontinuous and infinite; $q_{11}^{(N)}$ is zero if the singularity is located within the symmetry plane. The NMO ellipses for both S-waves are shown in Figure 3.
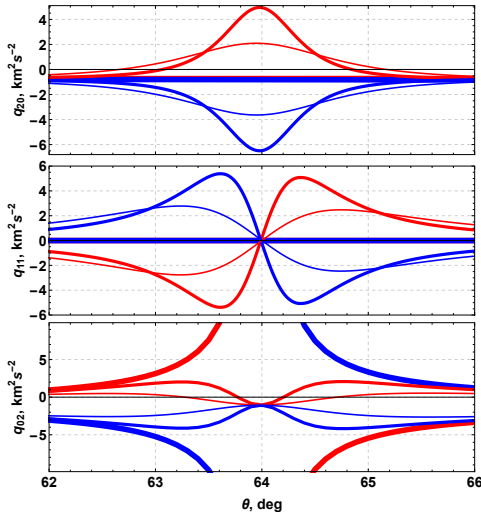
Figure 2: The second order derivatives $q_{20}^{(N)}$ (top), $q_{11}^{(N)}$ (middle), and $q_{02}^{(N)}$ (bottom) in vicinity of the singularity point ($\theta \approx 64°$, $\psi = 0$). Values for the S2-wave are shown in red, for the S1-wave in blue. Thickness represents different values of ψ: 0 (thick), 0.5° (medium), and 1° (thin).
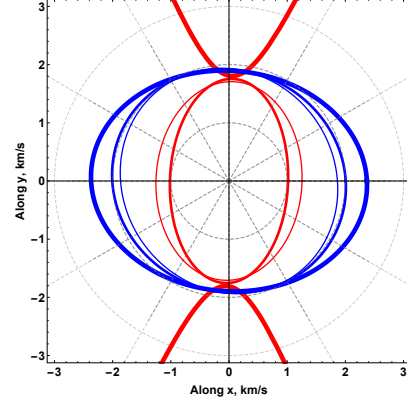
Figure 3: The NMO ellipses for S2- (red) and S1-waves (blue) in vicinity of the singularity point. Thickness represents different values of ψ: 3° (thick), 6° (medium), and 9° (thin).

CONCLUSIONS

We investigate the influence of the point singularity on the NMO ellipse in tilted orthorhombic media when the singularity occurs close to the vertical. We show that the NMO ellipse of the S2-wave degenerates into hyperbola for all the points on slowness surface where the Gaussian curvature is negative. The S1-wave NMO ellipse is elongated along one of its semi axes in vicinity of the singularity point.

ACKNOWLEDGMENTS

REFERENCES

Brown, R. J., S. Crampin, E. V. Gallant, and R. W. Vestrum, 1993, Modelling shear-wave singularities in an orthorhombic medium: Special issue; papers presented at the Fifth international workshop on Seismic anisotropy, **29**, 276–284.

Crampin, S., 1981, A review of wave motion in anisotropic and cracked elastic-media: Wave Motion, **3**, 343–391.

———, 1991, Effects of point singularities on shear-wave propagation in sedimentary basins: Geophysical Journal International, **107**, 531–543.

Grechka, V., and I. Tsvankin, 1998, 3-D description of normal moveout in anisotropic inhomogeneous media: Geophysics, **63**, 1079–92.

Grechka, V. Y., and I. R. Obolentseva, 1993, Geometrical structure of shear wave surfaces near singularity directions in anisotropic media: Geophysical Journal International, **115**, 609–616.

Lapilli, C., and P. Fowler, 2013, Rotation parameters for model building and stable parameter inversion in orthorhombic media: SEG Technical Program Expanded Abstracts 2013, 4656–4660.

Vavryuk, V., 2001, Ray tracing in anisotropic media with singularities: Geophysical Journal International, **145**, 265–276.

Elastic wave extrapolation in strongly heterogeneous anisotropic media

Junzhe Sun[*1], *Sergey Fomel*[1], *Yanadet Sripanich*[1] *and Paul Fowler*[2]
[1]*The University of Texas at Austin,* [2]*Fowler Geophysical Consulting*

SUMMARY

Conventional approaches to wave-mode separation assume that the medium properties are sufficiently smooth so that their spatial derivatives can be ignored. However, in strongly heterogeneous media, e.g., at medium interfaces, these terms can become significant and should be taken into account when wavefield extrapolation and wave-mode separation are performed simultaneously. In this work, we derive a general solution to the elastic anisotropic wave equation that is capable of accounting for strong heterogeneity of the model, and therefore providing accurate wavefields. We employ lowrank approximation for efficient application of the proposed operator. Numerical examples demonstrate 3D wave propagation in a two-layer orthorhombic model.

INTRODUCTION

Elastic wave extrapolation accounts for elastic properties of the Earth, which is crucial for seismic imaging of subsurface. Recently, recursive integral time extrapolation (RITE) methods (Du et al., 2014) have been introduced for stable and dispersion-free time extrapolation of elastic waves in isotropic (Chu and Stoffa, 2011; Firouzi et al., 2012) and anisotropic media (Hou et al., 2014; Cheng et al., 2016). Wave-mode separation is often needed to mitigate cross-talk between P- and S-waves in elastic imaging. In isotropic media, this can be achieved using the divergence and curl operators (Aki and Richards, 1980). In anisotropic media, wave-mode separation requires projecting the vector wavefield onto the polarization directions of different wave modes (Dellinger and Etgen, 1990). Most existing methods assume the medium property to be sufficiently smooth so that their spatial derivatives can be neglected (Dellinger and Etgen, 1990; Yan and Sava, 2009, 2012; Zhang and McMechan, 2010; Cheng and Fomel, 2014; Sripanich et al., 2015).

However, the Earth model can be strongly heterogeneous and contain discontinuities, e.g., at salt/sediment boundaries. In such cases, the assumption about the smoothness of the Earth model is no longer valid and could lead to inaccurate calculation of polarization directions. More importantly, simultaneous wave extrapolation and wave-mode separation based on such an assumption (Hou et al., 2014; Cheng et al., 2016) may fail to provide reliable phase and amplitude information. In this paper, we introduce a general framework for elastic wave extrapolation in strongly heterogeneous and anisotropic media without the assumption of the smoothness of the medium. The proposed method uses Fourier Integral Operator (FIO) which allows accurate and stable wave extrapolation to be performed without explicit wave-mode separation. We derive one-step elastic wave extrapolation based on the form of the analytical solution in the homogeneous case. Lowrank approximation is used for efficient calculation of the proposed FIO in heterogeneous media. Numerical examples demonstrate that the proposed method can provide a stable and dispersion-free solution to the elastic wave equation in heterogeneous anisotropic media.

THEORY

Following the notation of Du et al. (2014), the generic wave equation can be expressed in the following form:

$$\left(\frac{\partial^2}{\partial t^2} + \mathbf{A}\right)\mathbf{u}(\mathbf{x},t) = 0 , \qquad (1)$$

where $\mathbf{u}$ is the wavefield, $\mathbf{x}$ is the spatial location, t is time, and $\mathbf{A}$ is the a matrix operator containing material parameters and spatial derivative operators.

The analytical solution to equation 1 can be expressed in a one-step time stepping form

$$\hat{\mathbf{u}}(\mathbf{x},t+\Delta t) = e^{i\Phi\Delta t}\hat{\mathbf{u}}(\mathbf{x},t) , \qquad (2)$$

where $\hat{\mathbf{u}} = (\mathbf{u} - i\Phi^{-1}\mathbf{u}_t)/\sqrt{2}$ is a complex-valued wavefield and $\Phi \equiv \sqrt{\mathbf{A}}$.

For elastic anisotropic wave equations, the matrix operator $\mathbf{A}$ corresponds to the matrix $-\Gamma/\rho = -\mathbf{D}\mathbf{C}\mathbf{D}^{\mathsf{T}}/\rho$, where Γ is the Christoffel matrix, ρ is density, $\mathbf{C}$ is the elastic stiffness tensor expressed in Voigt notation as a 6×6 matrix, and $\mathbf{D}$ is the derivative matrix operator given by

$$\mathbf{D} = \begin{bmatrix} \partial_x & 0 & 0 & 0 & \partial_z & \partial_y \\ 0 & \partial_y & 0 & \partial_z & 0 & \partial_x \\ 0 & 0 & \partial_z & \partial_y & \partial_x & 0 \end{bmatrix} . \qquad (3)$$

In the Fourier (wavenumber) domain, $\mathbf{A}$ takes the form $\tilde{\Gamma}/\rho$ after i^2 cancels the negative sign, i.e., $-\Gamma \xrightarrow{\mathscr{F}} \tilde{\Gamma}$. In orthorhombic media, using the chain rule, $\tilde{\Gamma}$ can be expressed as follows:

$$\tilde{\Gamma} = \begin{bmatrix} C_{11}k_x^2 + C_{66}k_y^2 + C_{55}k_z^2 & (C_{12}+C_{66})k_xk_y & (C_{13}+C_{55})k_xk_z \\ (C_{12}+C_{66})k_xk_y & C_{66}k_x^2 + C_{22}k_y^2 + C_{44}k_z^2 & (C_{23}+C_{44})k_yk_z \\ (C_{13}+C_{55})k_xk_z & (C_{23}+C_{44})k_yk_z & C_{55}k_x^2 + C_{44}k_y^2 + C_{33}k_z^2 \end{bmatrix} - \qquad (4)$$

$$i \begin{bmatrix} \partial_x C_{11}k_x + \partial_y C_{66}k_y + \partial_z C_{55}k_z & \partial_x C_{12}k_y + \partial_y C_{66}k_x & \partial_x C_{13}k_z + \partial_z C_{55}k_x \\ \partial_y C_{12}k_x + \partial_x C_{66}k_y & \partial_x C_{66}k_x + \partial_y C_{22}k_y + \partial_z C_{44}k_z & \partial_y C_{23}k_z + \partial_z C_{44}k_y \\ \partial_z C_{13}k_x + \partial_x C_{55}k_z & \partial_z C_{23}k_y + \partial_y C_{44}k_z & \partial_x C_{55}k_x + \partial_y C_{44}k_y + \partial_z C_{33}k_z \end{bmatrix} .$$

When the Earth model is smooth, i.e., the derivatives of stiffnesses can be dropped, matrix $\tilde{\Gamma}$ is real-valued and symmetric positive definite. It can be diagonalized with its eigenvalues corresponding to the squared phase velocities of separate wave modes and its orthogonal eigenvectors corresponding to the polarization directions. In strongly heterogeneous media, both the eigenvalues and eigenvectors of Γ become complex-valued. Writing the eigendecomposition of $\mathbf{A}$ as follows:

$$\mathbf{A} = \mathbf{Q}\mathbf{V}\mathbf{Q}^{-1} = \begin{bmatrix} \mathbf{a}_1 & \mathbf{a}_2 & \mathbf{a}_3 \end{bmatrix} \begin{bmatrix} v_1^2 & 0 & 0 \\ 0 & v_2^2 & 0 \\ 0 & 0 & v_3^2 \end{bmatrix} \begin{bmatrix} \hat{\mathbf{a}}_1^* \\ \hat{\mathbf{a}}_2^* \\ \hat{\mathbf{a}}_3^* \end{bmatrix} , \qquad (5)$$

elastic wave extrapolation

Φ can be found by taking the square root of the eigenvalues in the diagonal matrix. Analogously, the wave extrapolation operator, $e^{i\Phi\Delta t}$, can be computed as:

$$e^{i\Phi\Delta t}\hat{\mathbf{u}}(k) = \sum_{i=1,2,3} e^{iv_i\Delta t}\mathbf{a}_i\hat{\mathbf{a}}_i^*\hat{\mathbf{u}} \qquad (6)$$

$$= \begin{bmatrix} \mathbf{a}_1 & \mathbf{a}_2 & \mathbf{a}_3 \end{bmatrix} \begin{bmatrix} e^{iv_1\Delta t} & 0 & 0 \\ 0 & e^{iv_2\Delta t} & 0 \\ 0 & 0 & e^{iv_3\Delta t} \end{bmatrix} \begin{bmatrix} \hat{\mathbf{a}}_1^* \\ \hat{\mathbf{a}}_2^* \\ \hat{\mathbf{a}}_3^* \end{bmatrix} \hat{\mathbf{u}}$$

$$= \begin{bmatrix} \hat{s}_{xx} & \hat{s}_{xy} & \hat{s}_{xz} \\ \hat{s}_{yx} & \hat{s}_{yy} & \hat{s}_{yz} \\ \hat{s}_{zx} & \hat{s}_{zy} & \hat{s}_{zz} \end{bmatrix} \hat{\mathbf{u}},$$

In heterogeneous media, the eigenvalues and eigenvectors depend on both space and wavenumber. We propose to apply the lowrank decomposition (Fomel et al., 2013) on the mixed-domain components $\hat{s}_{ij}$, without explicitly decomposing the wavefield into different wave-modes. One-step lowrank method can handle complex-valued propagation operator (Sun et al., 2016).

NUMERICAL EXAMPLES
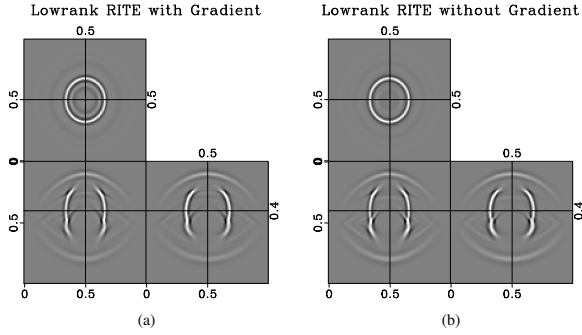
Figure 1: Wavefield snapshot of wavefield propagation in a two-layer orthorhombic model using the lowrank RITE method with (a) and without (b) accounting for the gradient of stiffnesses.

To test the proposed method, we construct a two-layer orthorhombic model on a $100 \times 100 \times 100$ grid with the density-normalized stiffness tensor of the first layer given by Schoenberg and Helbig (1997), and the second layer having twice the stiffness values of the first layer. The spatial sampling rate in all directions of the grid is $10\ m$. A displacement source is oriented at $45°$ tilt and $45°$ azimuth and injected at $x = 0.5\ km$, $y = 0.5\ km$, $z = 0.4\ km$. The source wavelet has a peak frequency of $35\ Hz$. Figure 1 shows wavefield snapshots taken at $t = 0.15\ s$. Because of the strong contrast at the medium interface, the transmitted and reflected waves calculated by the proposed method considering the stiffness gradient demonstrates noticeable amplitude and phase differences compared with the waves calculated by ignoring the gradient terms.

CONCLUSIONS

We have presented a general formulation for accurate and stable elastic wave extrapolation in strongly heterogeneous and anisotropic media. The proposed method employs a one-step lowrank approximation to efficiently apply the FIO defined by the complex-valued eigenvalues and eigenvectors of the Christoffel matrix. Numerical examples show that the proposed method improves wave extrapolation accuracy by considering gradients of the model stiffnesses.

ACKNOWLEDGMENTS

REFERENCES

Aki, K., and P. G. Richards, 1980, Quantitative seismology: W.H. Freeman & Co.

Cheng, J., T. Alkhalifah, Z. Wu, P. Zou, and C. Wang, 2016, Simulating propagation of decoupled elastic waves using low-rank approximate mixed-domain integral operators for anisotropic media: Geophysics, **81**, T63–T77.

Cheng, J., and S. Fomel, 2014, Fast algorithms for elastic-wave-mode separation and vector decomposition using low-rank approximation for anisotropic media: Geophysics, **79**, no. 4, C97–C110.

Chu, C., and P. L. Stoffa, 2011, Application of normalized pseudo-Laplacian to elastic wave modeling on staggered grids: Geophysics, **76**, T113–T121.

Dellinger, J., and J. Etgen, 1990, Wave-field separation in two-dimensional anisotropic media: Geophysics, **55**, no. 7, 914–919.

Du, X., P. J. Fowler, and R. P. Fletcher, 2014, Recursive integral time-extrapolation methods for waves: A comparative review: Geophysics, **79**, no. 1, T9–T26.

Firouzi, K., B. T. Cox, B. E. Treeby, and N. Saffari, 2012, A first-order k-space model for elastic wave propagation in heterogeneous media: The Journal of the Acoustical Society of America, **132**, 12711283.

Fomel, S., L. Ying, and X. Song, 2013, Seismic wave extrapolation using lowrank symbol approximation: Geophysical Prospecting, **61**, no. 3, 526–536.

Hou, S., Q. Du, and G. Fang, 2014, Elastic wavefield extrapolation based on wavefield vector decomposition and lowrank decomposition: 84th Annual International Meeting, SEG, Expanded Abstracts, 3411–3416.

Schoenberg, M., and K. Helbig, 1997, Orthorhombic media: Modeling elastic wave behavior in a vertically fractured earth: Geophysics, **62**, no. 6, 1954–1974.

Sripanich, Y., S. Fomel, J. Sun, and J. Cheng, 2015, Elastic wave-vector decomposition in orthorhombic media: 85th Annual International Meeting, SEG, Expanded Abstracts, 498–503.

Sun, J., S. Fomel, and L. Ying, 2016, Lowrank one-step wave extrapolation for reverse-time migration: Geophysics, **81**, no. 1, S39–S54.

Yan, J., and P. Sava, 2009, Elastic wave-mode separation for VTI media: Geophysics, **74**, no. 5, WB19–WB32.

——, 2012, Elastic wave mode separation for tilted transverse isotropic media: Geophysical Prospecting, **60**, 29–48.

Zhang, Q., and G. A. McMechan, 2010, 2D and 3D elastic wavefield vector decomposition in the wavenumber domain for VTI media: Geophysics, **75**, no. 3, D13–D26.

Simulation of anisotropic wave propagation with anisotropic attenuation

Tieyuan Zhu
Department of Geosciences, Pennsylvania State University

SUMMARY

I present a time-domain velocity-stress formulation of the viscoelastic anisotropy wave equation, which holds for arbitrarily anisotropic velocity and attenuation. Using the frequency-independent Q model, anisotropic attenuation is mathematically expressed via factional time derivatives. Fractional time derivatives are solving using the Grünwald-Letnikov approximation. I validate numerical solutions by comparing with theoretical attenuation values. Simulations in 2D and 3D models are presented.

INTRODUCTION

Modeling wave propagation in anisotropic media is the fundamental element of full-waveform inversion/imaging of anisotropy parameters. Considering only velocity anisotropy, wave propagation are well described by the anisotropic elastic wave equation. In the past decades, this has been extensively studied, e.g. the most simple transversely isotropy (TI), the practical acoustic TI (Alkhalifah, 2000), and general anisotropy (Carcione et al., 1992). In addition, the medium usually exhibits anisotropic attenuation behavior, which has been observed in lab experiments (e.g., Tao and King, 1990) and some field case studies (e.g., Liu et al., 1993; Lynn et al., 1999). To numerically modeling such a wave behavior (attenuation is directional-dependent), a wave equation is needed.

Carcione (1992) generalize Backus averaging to the anelastic case, obtaining the first model for Q-anisotropy. The constant-Q anelastic behavior is approximately described by a set of standard linear solid elements. Similarly, Bai and Tsvankin (2016) use the generalized standard linear solid model to produce nearly constant values of all components of the quality-factor matrix within a specified frequency band. But they replace isotropic relaxation times τ by anisotropic relaxation times τ_{ij} that explicitly represent anisotropic attenuation. The corresponding wave equation is based on a set of anisotropic viscoelastic wave equations parameterized by memory variables.

Alternatively, the frequency-independent Q model (Kjartansson, 1979) is simpler and can be used to represent the attenuation behavior in wave equation (Carcione et al., 2002; Zhu and Harris, 2014). Carcione et al. (2002) and Carcione (2009) derived a viscoacoustic wave equation for P-wave and a viscoelastic wave equation for simulating P-wave and S-wave attenuation. In this study, I extend the formulation to the general viscoelastic anisotropic wave equation. I use the elastic stiffness tensor along with the anisotropic Q_{ij} matrix to define a complex stiffness matrix. Based on the property of the fractional derivative, the convolution is replaced by the fractional time derivatives in the constitutive relation. The derived time-domain velocity-stress formulation of viscoelastic anisotropic wave equation holds for arbitrarily anisotropic velocity and attenuation. I investigate the accuracy of the proposed wave equation by comparing with exact solutions. Finally I show simulations with 2D VTI and 3D orthorhombic attenuation.

CONSTITUTIVE RELATION

The generalized time-domain constitutive relation for the viscoelastic anisotropic medium is introduced (Carcione, 2014)

$$\sigma_{ij}(\mathbf{x},t) = \psi_{ijkl}(\mathbf{x},t) * \partial_t \varepsilon_{kl}(\mathbf{x},t) \tag{1}$$

where t is the time variable, $\mathbf{x}$ is the position vector, $*$ denotes time convolution, ψ are the components of the relaxation function tensor, and ε is the strain tensor. $i,j,k,l = 1,2,3$. The fourth-rank tensor ψ_{ijkl} contains all the information about the behavior of the medium under infinitesimal deformations. In the most general case, the number of components is 21.

Considering the frequency-independent (constant-Q) model (Kjartansson, 1979), the relaxation function is defined

$$\psi(t) = \frac{M_0}{\Gamma(1-t)} \frac{t}{t_0}^{-2\gamma} H(t) \tag{2}$$

where M_0 is a bulk moduls. Γ is Euler's Gamma function, $t_0 = 1/\omega_0$ where ω_0 is a reference frequency, γ is a dimensionless parameter, and H is the Heaviside step function. Therefore, in isotropic acoustic media, the constitutive equation is written as in terms of fractional derivative (Caputo and Mainardi, 1971; Carcione et al., 2002)

$$\sigma(t) = M_0 \omega_0^{-2\gamma} \partial_t^{2\gamma} \varepsilon(t) \tag{3}$$

where $\gamma = \arctan(1/Q)/\pi$. The fractional time derivatives is solved by the Grünwald-Letnikov approximation

$$\partial_t^\gamma \varepsilon(t) \approx \Delta t^{-\gamma} \sum_{m=0}^{\gamma} (-1)^m \binom{N}{j} \varepsilon(t - m\Delta t) \tag{4}$$

The fractional derivative of wavefield variable ε at time t depends on all the previous values of ε. This memory property of the fractional derivative is, associated to field attenuation, increase the computational costs, especially saving 4D (x,y,z,t) field variables in the three-dimensional problem. One strategy of reducing the costs is to truncate the binomial coefficients for m exceeding an integer N (total time step) (Podlubny, 1999). This allows truncation of the sum at $m = L$, $L \ll N$, where L is the effective memory length.

ANISOTROPIC Q

In transversely isotropic (TI) media, the elastic model is fully characterized by five elastic parameters and density. To consider the medium anelasticity, I adopt the definition: anisotropy

Q is defined as the ratio of the real and the imaginary parts of the corresponding stiffness coefficient (Carcione, 1992; Zhu and Tsvankin, 2006), $Q_{ij} = \frac{Re(p_{ij})}{Im(p_{ij})}$, where p_{ij} is the complex stiffness tensor. Therefore, five additional anelastic parameters are needed to characterize the viscoelastic behavior. In orthorhombic media, nine additional anelastic parameters are needed to describe the viscoelastic behavior.

With the stiffness matrix, using equations 2 and 3 yields the constitutive relation of 3-D viscoelastic-anisotropic media

$$
\begin{bmatrix} \sigma_{11} \\ \sigma_{22} \\ \sigma_{33} \\ \sigma_{23} \\ \sigma_{13} \\ \sigma_{12} \end{bmatrix} = \begin{bmatrix} D_{11} & D_{12} & D_{13} & D_{14} & D_{15} & D_{16} \\ 0 & D_{22} & D_{23} & D_{24} & D_{25} & D_{26} \\ 0 & 0 & D_{33} & D_{34} & D_{35} & D_{36} \\ 0 & 0 & 0 & D_{44} & D_{45} & D_{46} \\ 0 & 0 & 0 & 0 & D_{55} & D_{56} \\ 0 & 0 & 0 & 0 & 0 & D_{66} \end{bmatrix} \begin{bmatrix} \varepsilon_{11} \\ \varepsilon_{22} \\ \varepsilon_{33} \\ 2\varepsilon_{23} \\ 2\varepsilon_{13} \\ 2\varepsilon_{12} \end{bmatrix}
$$
(5)

where $D_{ij} = C_{ij}\omega_0^{-2\gamma_{ij}}\partial_t^{2\gamma_{ij}}$, and $\gamma_{ij} = \arctan(1/Q_{ij})/\pi$. Equation 5 plus the momentum conservation equations constitute the full viscoelastic anisotropic wave equation with both anisotropic velocity and attenuation. The first-order time derivatives are solved by staggered-grid finite-difference and space derivatives are solved by pseudo-spectral Fourier method.

NUMERICAL EXAMPLES

To validate numerical solutions of the viscoelastic anisotropic wave equation, I generate the wavefield in a homogeneous viscoelastic VTI medium and then estimate P- and SV-wave quality factors using the spectral-ratio method and compare to the exact solution.

The model size is 256×256. The spacings in x and z directions are 10 m. The model anisotropic parameters are $v_p = 6.0$ km/s, $v_s = 3.0$ km/s, $\rho = 2.0$ g/cm^3, $\varepsilon = 0.2$, and $\delta = 0.1$. The anisotropic Q_{ij} are $Q_{11} = 35$, $Q_{13} = 50$, $Q_{33} = 50$, and $Q_{55} = 30$. The source using a 30 Hz Ricker wavelet is located in the center of the model. Figures 1a and 1b show snapshots of anisotropy wave propagation at 300 ms. The case (Figure 1a) with attenuation show the reduced amplitude.

Receivers are circle-positioned and 1 km away from the center of model. Figure 2 compares estimated quality factors to theoretical solutions. Estimations of P-wave attenuation (circle) almost perfectly match the exact curve (solid line). In the diagonal direction, estimations of SV-wave attenuation deviate slightly from the exact solution. This is likely caused by complex SV-wave in these angles in which attenuation estimation may not be accurate. Figure 3 shows two snapshot of 3D anisotropic wave propagation with orthorhombic attenuation (a) ($Q_{11} = 35$, $Q_{12} = 35$, $Q_{13} = 35$, $Q_{22} = 35$, $Q_{23} = 35$, $Q_{33} = 50$, $Q_{44} = 50$, $Q_{55} = 35$, and $Q_{66} = 30$) and without attenuation (b).

CONCLUSION

I present a viscoelastic anisotropic wave equation that is able to characterize phase and attenuation anisotropy. The wave equation holds for arbitrary anisotropy. I show that numerical solutions approximate to the exact ones. Simulations in 2D and 3D synthetic models (including TI and orthorhombic) are presented.

ACKNOWLEDGMENTS
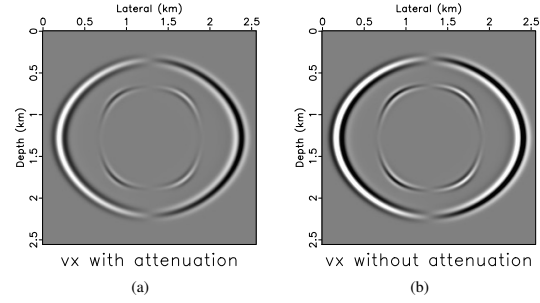
Figure 1: Snapshots (Vx component) of anisotropy wave propagation with TI attenuation (a) and without attenuation (b).
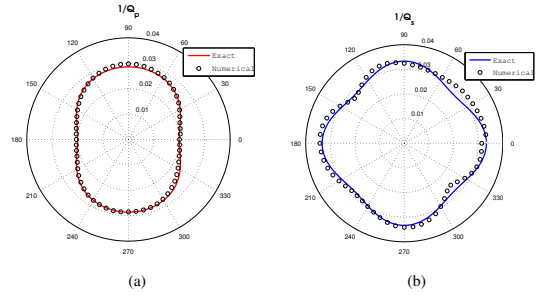
Figure 2: Attenuation $1/Q$ of P-wave (a) and S-wave (b) as functions of the phase angle. Circles are estimations from numerical simulations using spectral ratio. Solid lines denote exact solution from Q_{ij} definition.
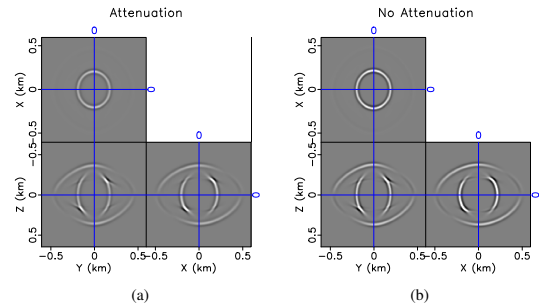

Figure 3: Snapshots (Vx) of anisotropy wave propagation with orthorhombic attenuation (a) and without attenuation (b).

REFERENCES

Alkhalifah, T., 2000, An acoustic wave equation for anisotropic media: Geophysics, **65**, 1239–1250.

Bai, T., and I. Tsvankin, 2016, Time-domain finite-difference modeling for attenuative anisotropic media: Geophysics, **81**, C69–C77.

Caputo, M., and F. Mainardi, 1971, A new dissipation model based on memory mechanism: Pure and Applied Geophysics, **91**, 134–147.

Carcione, J., 1992, Anisotropic q and velocity dispersion of finely layered media1: Geophysical Prospecting, **40**, 761–783.

Carcione, J., D. Kosloff, A. Behle, and G. Seriani, 1992, A spectral scheme for wave propagation simulation in 3-d elastic-anisotropic media: Geophysics, **57**, 1593–1607.

Carcione, J. M., 2009, Theory and modeling of constant-Q P- and S-waves using fractional time derivatives: Geophysics, **74**, T1–11.

——, 2014, Wave fields in real media: Theory and numerical simulation of wave propagation in anisotropic, anelastic, porous and electromagnetic media, 3rd ed.: Elsevier.

Carcione, J. M., F. Cavallini, F. Mainardi, and A. Hanyga, 2002, Time-domain seismic modeling of constant-Q wave propagation using fractional derivatives: Pure and Applied Geophysics, **159**, 1719–1736.

Kjartansson, E., 1979, Constant-Q wave propagation and attenuation: Journal of Geophysical Research, **84**, 4737–4748.

Liu, E., S. Crampin, J. H. Queen, and W. D. Rizer, 1993, Velocity and attenuation anisotropy caused by microc- racks and microfractures in a multiazimuth reverse vsp: Canadian Journal of Exploration Geophysics, **29**, 177–188.

Lynn, H. B., D. Campagna, K. M. Simon, and W. E. Beckham, 1999, Relationship of p-wave seismic attributes, az- imuthal anisotropy, and commercial gas pay in 3-d p- wave multiazimuth data, rulison field, piceance basin, colorado: Geophysics, **64**, 1293–1311.

Podlubny, I., 1999, Fractional Differential Equations: Academic Press.

Tao, G., and M. S. King, 1990, Shear-wave velocity and q anisotropy in rocks: A laboratory study: International Journal of Rock Mechanics and Mining Sciences and Ge- omechanics Abstracts, **27**, 353361.

Zhu, T., and J. M. Harris, 2014, Modeling acoustic wave propagation in heterogeneous attenuating media using decoupled fractional Laplacians: Geophysics, **79**, T105–T116.

Zhu, Y., and I. Tsvankin, 2006, Plane-wave propagation in attenuative transversely isotropic media: Geophysics, **71**, T17–T30.

P-, SV and PSV-wave reflections from a thin VTI layer

Qi Hao*, NTNU; Alexey Stovas, NTNU

Summary

We present the approximate formulae for reflection coefficients from a thin, transversely isotropic layer with a vertical symmetry axis (VTI) embedded in a VTI background. We discuss the assumptions to derive the formulae. A numerical example illustrates the comparison between approximate formulae and exact solution.

Introduction

Characterizing the plane wave reflection from an anisotropic layer is useful for reservoir monitoring and parameters inversion. For horizontally layered media, the reflection and transmission of plane waves can be derived by using the transfer matrix method. Brekhovskikh (1980) systematically studied the wave propagation for horizontally layered, isotropic media. The reflection coefficients from a thin VTI layer can also be derived by transfer matrix method. However, the exact formulae for the reflection coefficients suffer from the algebraic complexity, which is not easily to be utilized in seismic.

In this expanded abstract, we study the reflection of incident plane P- and SV-waves from a thin, homogeneous VTI layer embedded in a homogeneous VTI background (see Figure 1). We adopt Thomsen's (1986) notations to describe a VTI medium. We use the following parameters: υ_{P0} and υ_{S0} denote the velocities of vertically propagating P and S-waves; ε and δ denote Thomsen (1986) anisotropy parameters. The density of medium is denoted by ρ. For simplicity, the P-mode reflection of an incident P-wave is denoted by PP-wave; the SV-mode reflection of an incident P-wave is denoted by PS-wave; the SV-mode reflection of an incident SV-wave is denoted by SS-wave.

Three assumptions

By an analogy with the weak-contrast approximations for VTI reflection coefficients (e.g. Thomsen, 1993) at an interface, we consider the following assumptions to derive the approximate formulae for reflections coefficients from a thin layer.

First, we assume the weak contrast in elastic properties (including density ρ, P-wave vertical velocity υ_{P0} and SV-wave vertical velocity υ_{S0}) at the interface between the thin layer and the background,

$$\left|\frac{\Delta\upsilon_{p0}}{\bar{\upsilon}_{p0}}\right| \ll 1, \left|\frac{\Delta\upsilon_{s0}}{\bar{\upsilon}_{s0}}\right| \ll 1, \left|\frac{\Delta\rho}{\bar{\rho}}\right| \ll 1, \quad (1)$$

where $\Delta\alpha = \alpha^{(M)} - \alpha^{(A)}$, and $\bar{\alpha} = (\alpha^{(M)} + \alpha^{(A)})/2$ denote the difference and the average of medium parameter α at the interface between the layer (corresponding to the superscript M) and the background (corresponding to the superscript A).

Second, we assume that the weak anisotropy assumption is valid for both layer and background. This means that

$$\left|\varepsilon^{(\mu)}\right| \ll 1, \left|\delta^{(\mu)}\right| \ll 1, \quad (2)$$

where the superscript μ is taken as M and A for the layer and the background.

Third, we assume that the VTI layer is very thin such that it satisfies the following inequality,

$$hq_P^{(M)}\omega < hq_S^{(M)}\omega \ll 1, \quad (3)$$

where h denotes the layer thickness; ω is the angular frequency; $q_P^{(M)}$ and $q_S^{(M)}$ correspondingly denote the vertical slowness components of P- and SV-waves in the layer, which are functions of the horizontal slowness component.

From several numerical tests, we find the following condition to replace inequality 3 for simplicity,

$$\omega h \le 0.2\upsilon_{P0}^{(M)} . \quad (4)$$

AVO-type formulae for reflection coefficients

We start with the exact formulae for reflection coefficients and consider the assumptions from the previous section. We expand the exact reflection coefficients with respect to the contrasts in elastic parameters according to equation 1, the anisotropy parameters in equation 2, and the layer thickness. This results in the AVO-type formulae for reflection coefficients from a thin VTI layer.

The first-order approximation for the PP-wave reflection coefficient,

$$R_{PP}(\theta_P) = \frac{i\omega h}{\bar{\upsilon}_{p0}} R_{PP}^{(1)}(\theta_P) , \quad (5)$$

where θ_P denotes the angle of incidence of P-waves; i denotes the imaginary unit, and

$$\frac{R_{PP}^{(1)}(\theta_P)}{\cos\theta_P} = -\frac{\Delta Z_{P0}}{\bar{Z}_{P0}} - \tan^2\theta_P \frac{\Delta\upsilon_{P0}}{\bar{\upsilon}_{P0}} + 4\sin^2\theta_P \frac{\bar{\upsilon}_{S0}^2}{\bar{\upsilon}_{P0}^2} \frac{\Delta G_0}{\bar{G}_0}$$
$$- \sin^2\theta_P(\tan^2\theta_P\Delta\varepsilon + \Delta\delta) \quad (6)$$

Here, $Z_{P0} = \rho\upsilon_{P0}$ denotes the P-wave impedance; and $G_0 = \rho\upsilon_{S0}^2$ denotes the shear modulus.

The second-order approximation for the PP wave reflection coefficient is given by

$$R_{PP}(\theta_P) = \frac{i\omega h}{\bar{\upsilon}_{p0}} R_{PP}^{(1)}(\theta_P) - \frac{\omega^2 h^2}{\bar{\upsilon}_{P0}^2} R_{PP}^{(2)}(\theta_P) , \quad (7)$$

where

$$R_{PP}^{(2)}(\theta_P) = \cos\theta_P R_{PP}^{(1)}(\theta_P) . \quad (8)$$

An acoustic eikonal equations for attenuating, orthorhombic media

The first-order approximation for the SS-wave reflection coefficient is given by

$$R_{SS}(\theta_S) = \frac{i\omega h}{\overline{\upsilon}_{s0}} R_{SS}^{(1)}(\theta_S) \quad , \qquad (9)$$

where θ_s denotes the angle of incidence of SV-waves, and

$$\frac{R_{SS}^{(1)}(\theta_S)}{\cos\theta_S} = -(1 - 2\cos(2\theta_S))\frac{\Delta G_0}{\overline{G}_0} - \frac{\cos(2\theta_S)}{\cos^2\theta_S}\frac{\Delta\upsilon_{S0}}{\overline{\upsilon}_{S0}}$$
$$-\sin^2\theta_S \frac{\overline{\upsilon}_{S0}^2}{\overline{\upsilon}_{P0}^2}(\Delta\varepsilon - \Delta\delta) \qquad . \quad (10)$$

The second-order formula for the SS-wave reflection coefficient is given by

$$R_{SS}(\theta_S) = \frac{i\omega h}{\overline{\upsilon}_{p0}} R_{SS}^{(1)}(\theta_S) - \frac{\omega^2 h^2}{\overline{\upsilon}_{S0}^2} R_{SS}^{(2)}(\theta_S) \quad , \quad (11)$$

with

$$R_{SS}^{(2)} = \cos\theta_S R_{SS}^{(1)} \quad . \qquad (12)$$

The first-order approximation for the PS-wave reflection coefficient is given by

$$R_{PS}(\theta_P) = \frac{i\omega h}{\overline{\upsilon}_{P0}} R_{PS}^{(11)}(\theta_P) + \frac{i\omega h}{\overline{\upsilon}_{S0}} R_{PS}^{(12)}(\theta_P) \quad , \quad (13)$$

with

$$R_{PS}^{(11)}(\theta_P) = \sin\theta_S \frac{\Delta\rho}{\overline{\rho}} + 2\cos(2\theta_S)\sin\theta_S \frac{\Delta\upsilon_{S0}}{\overline{\upsilon}_{S0}} \quad , \quad (14)$$

$$R_{PS}^{(12)}(\theta_P) = \frac{\sin(\theta_P + 3\theta_S)}{\cos\theta_S} \frac{\Delta\rho}{\overline{\rho}} + 2\cos\theta_P \cos(2\theta_S)\sin\theta_S \frac{\Delta\upsilon_{S0}}{\overline{\upsilon}_{S0}}$$
$$-\frac{\overline{\upsilon}_{P0}}{2\overline{\upsilon}_{S0}}\sin\theta_S(2\sin^2\theta_P\Delta\varepsilon - \cos(2\theta_P)\Delta\delta) \qquad ,(15)$$

where $\theta_S = \arcsin(\overline{\upsilon}_{S0}\sin\theta_P / \overline{\upsilon}_{P0})$ denotes the angle of reflection of SV-waves in the average isotropic medium. The second-order formula for the PS-wave reflection coefficient is given by

$$R_{PS}(\theta_P) = \frac{i\omega h}{\overline{\upsilon}_{P0}} R_{PS}^{(11)}(\theta_P) + \frac{i\omega h}{\overline{\upsilon}_{S0}} R_{PS}^{(12)}(\theta_P)$$
$$-\frac{\omega^2 h^2}{\overline{\upsilon}_{P0}^2} R_{PS}^{(21)}(\theta_P) - \frac{\omega^2 h^2}{\overline{\upsilon}_{P0}\overline{\upsilon}_{S0}} R_{PS}^{(22)}(\theta_P) - \frac{\omega^2 h^2}{\overline{\upsilon}_{S0}^2} R_{SS}^{(23)}(\theta_P) \quad .(16)$$

Examples

We design a thin layer model embedded in an unbounded VTI background. The parameters of the thin layer include: $\upsilon_{P0}^{(M)} = 3.5 km/s$, $\upsilon_{S0}^{(M)} = 1.6 km/s$, $\rho^{(M)} = 3.0 g/cm^3$, $\varepsilon^{(M)} = 0.1$, $\delta^{(M)} = 0.05$, $h = 16.7 m$. The parameters of the background include: $\upsilon_{P0}^{(A)} = 3.0 km/s$, $\upsilon_{S0}^{(A)} = 1.6 km/s$, $\rho^{(A)} = 2.6 g/cm^3$, $\varepsilon^{(M)} = 0.1$ and $\delta^{(M)} = 0.05$. The angular frequency of the waves is $\omega = 30 Hz$. Figures 2 to 4 indicate that (1) first-order formulae cannot be used to describe the phase change due to the existence of the layer; (2) the second-order formulae are relatively accurate.

Conclusions
The propose simple approximate formulae provide an analytic perspective for the influence of the change in VTI parameters on the PP-, SS- and PS-wave reflection coefficients computed from the thin VTI layer.

Acknowledgments

References
Brekhovskikh, L.M., 1980, Waves in layered media: Academic, London.
Thomsen, L., 1986, Weak elastic anisotropy: Geophysics, 51, 1954-1966.
Thomsen, L., 1993, Weak anisotropic reflections. In: Offset dependent reflectivity (Castagna and Backus, Eds.): SEG.
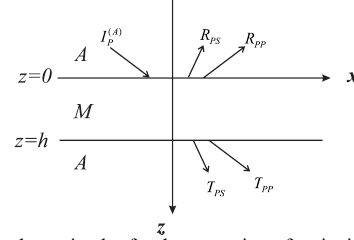
Figure 1. A schematic plot for the scattering of an incident plane P-wave by a horizontal VTI layer (M) embeded in a VTI background (A).
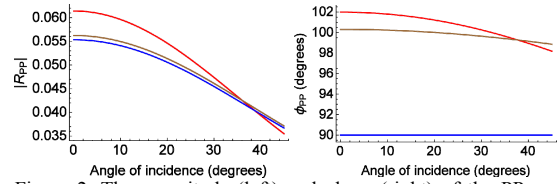
Figure 2. The magnitude (left) and phase (right) of the PP-wave reflection coefficient as a function of the angle of incidence. The red, blue and brown lines correspond to the exact solution, the first-order formula and the second-order formula, respectively.
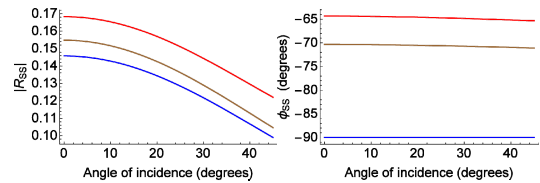
Figure 3. Similar to Figure 2 but for the SS-wave reflection coefficient.
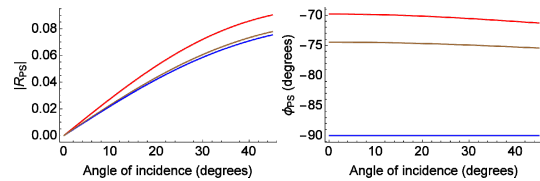
Figure 4. Similar to Figure 2 but for the PS-wave reflection coefficient.

Imaging crust in northeast part of Tibetan Plateau and seismic anisotropy from ambient noise data

Qiong Wang*, Yuan Gao
Institute of Earthquake Science, China Earthquake Administration, Beijing, China.

Summary

We collected continuous seismic data recorded between 2011 and 2012 by 118 broadband stations from China Digital Seismic Network (CDSN) to image the crustal structure and azimuthal anisotropy beneath the northeast part of Tibetan Plateau. Rayleigh wave empirical Green's functions are extracted from the interstation cross-correlation of vertical component records. Phase velocities and azimuthal anisotropy are then obtained from the empirical Green's functions in 8 to 35s period. Furthermore, by adopting the pure-path Rayleigh-wave dispersion curves for each grid node, we finally construct the 3D shear wave velocity in the northeastern Tibetan Plateau. The results show that at period 8s and 12s, sediments feature much slower seismic velocities than crystalline rocks, so Qaidam basin shows low velocity. The anisotropy in this period is consistent with the regional fault, which means the polarization direction of the fast wave goes along the strike of the fault. At period 18 to 25s, the Qiangtang and Songpan-Ganzi terranes become low velocities gradually. The anisotropy in this period is similar to the last one. And at period 30 to 35s, the phase velocities are mainly influenced by the Moho depth. Meanwhile, the fast polarization in the Songpan-Ganzi terrane displays a clockwise rotation in this range. Through vertical profiles of shear wave velocity, we find that the Songpan-Ganzi terrane is associated with a low velocity at middle-lower crust, but it terminates in Qaidam basin. For the azimuthal anisotropy, we find that with the period increasing, the polarization direction is consistent, which suggest that a vertically coherent deformation within the lithosphere beneath the margin of Tibetan plateau.

Introduction

The large-scale surface deformation, uplifting and faulting occurring at the NE margin of the Tibetan plateau are generally believed to be caused by the continuous collision between the India and Eurasia since ~50 millions years ago. However, the style and amount of the subsurface deformation induced by the collision, especially those inside the lower crust and upper mantle are still debated, which also is the hot topics in study of the seismology and geodynamics. Many models have been proposed to explain the deformation of the Tibetan Plateau, such as uniform lithospheric shortening (England and Houseman, 1986) and crustal channel flow (Clark and Royden, 2002). The first model suggests a vertically coherent deformation across the entire lithosphere, while the second model means lower crustal flow is assumed to split into two branches: one channel thought to flow to the south of Longmenshan fault and finally to the Yungui plateau, and the other is believed to flow along the Qinling orogen between the Ordos block and Sichuan basin.

Ambient noise tomography is an emerging field of seismological research in recent years, comparing to seismic surface wave, the main advantage of ambient noise tomography is that it can retrieve velocity dispersion at relatively short period without seismic source location, which is more sensitive to shallow crustal structure. Therefore, shallow surface wave tomography using ambient noise is now widely applied (Fang et al, 2009; Shapiro et al., 2005; Nikolai et al., 2005).

In this study, we focus on a complex junction that connects the margin of the Tibetan plateau with the Alxa block, Ordos plateau and the Qinling orogen, where broadband seismic data of 118 stations are available (Figure 1). We measure Rayleigh wave velocity, azimuthal anisotropy and shear wave velocity at this region to investigate the crustal structure and deformation beneath the NE margin of the plateau and its surrounding areas.
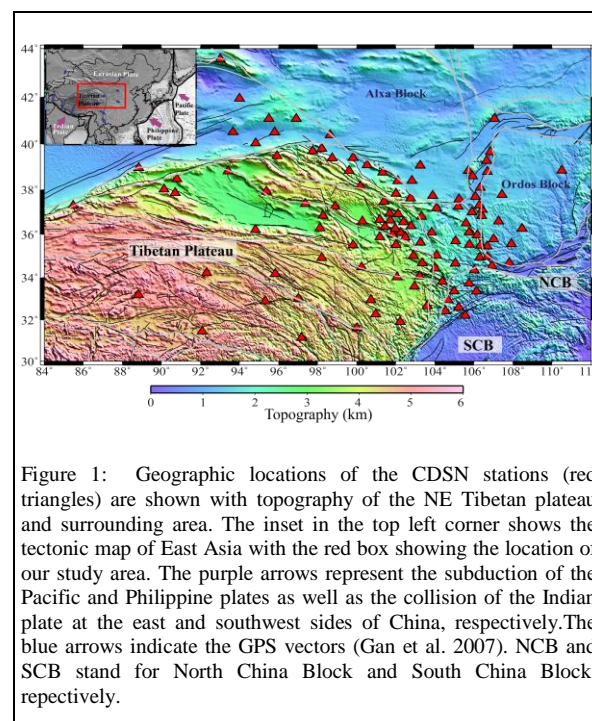
Figure 1: Geographic locations of the CDSN stations (red triangles) are shown with topography of the NE Tibetan plateau and surrounding area. The inset in the top left corner shows the tectonic map of East Asia with the red box showing the location of our study area. The purple arrows represent the subduction of the Pacific and Philippine plates as well as the collision of the Indian plate at the east and southwest sides of China, respectively. The blue arrows indicate the GPS vectors (Gan et al. 2007). NCB and SCB stand for North China Block and South China Block, repectively.

Crustal structure and anisotropy beneath NE Tibet

Theory and/or Method

The data processing of retrieving Rayleigh wave phase velocity from ambient noise used in our study is followed by Yao et al. (2006) and we just estimate Rayleigh wave Green's Function from vertical component which has relatively stronger energy. The resolution of ambient noise tomography is limited primarily by the number of well-distributed stations.

The main procedures include single station data preparation, cross-correlation and stacking, phase velocity dispersion measurement and phase velocity and azimuthal anisotropy. Continuous data are decimated to one sample per sec and are then filtered in the period band from 5 to 50s. Time domain normalization applying running absolute mean normalization method, with the purpose of suppressing the influence of earthquake signals to the cross-correlation.

Generally, there is a pronounced asymmetry between positive and negative time lags of each cross-correlation. This asymmetry originates from an inferred non-uniform distribution of source locations of noise. To reduce the influence of the noise source, we compress the two-sided signal into a one-sided signal by averaging the positive and negative time lags to obtain the "symmetric" signal.

We thus obtain 5773 Rayleigh wave dispersion curves in the period 5 to 35s on the basis of image analysis technique, and this method can trace the whole curve quickly and greatly enhance the accuracy of phase velocity measurements compared to traditional tracing point method. And then, based on the relationship between the phase velocity and azimuthal anisotropy, we finally invert the velocity and anisotropy at the same time following Smith and Dahlen's (1973) theory.

Conclusions

We analyzed a large amount of continuous data to investigate crustal structure and seismic anisotropy beneath the NE Tibetan Plateau and its surrounding areas. We found that there exist two low-velocity zones in the northeast Tibetan Plateau, one is Songpan-Ganze block and the other is northwest Qilian Qorgen. Meanwhile, the low velocity zones weakened in the Kunlun fault and terminated in Qaidam basin, which infer that Kunlun fault may be the north boundary of Sonpan-Ganze low-velocity zone. We also found that with the period increasing, the polarization direction is consistent. These observations combining other research suggest that the crust and mantle lithosphere are mechanically coupled and deformed coherently in responding to the India-Asia collision, and therefore the whole lithospheric shortening is likely the dominant mechanism for the observed large uplifting and crustal thickening within the margin.

REFERENCE CHANGE:

Clark, M.K. & Royden, L.H., 2000. Topographic ooze: Building the eastern margin of Tibet by lower crustal flow, Geology, 28, 703–706.

England, P. & Houseman, G., 1986. Finite strain calculations of continental deformation 2. Comparison with the India-Asia collision zone, J geophys Res, 91(B3), 3664–3676.

Fang L H, Wu J P, Lv Z Y. 2009. Rayleigh wave group velocity tomography from ambient seismic noise in North China. Chinese J Geophys (in Chinese), 52(3): 663-671.

Gan, W., Zhang, P., Shen, Z.K., et al, 2007. Present-day crustal motion within the Tibetan Plateau inferred from GPS measurements, J Geophys Res, 112: B8416.

Nikolai M. Shapiro，Michel Campillo，Laurent Stehly，et al. 2005. High resolution suface wave tomography from ambient seismic noise. Science，307：1615-1618.

Shapiro N M, Campillo M, Stehly L, et al. 2005. High-resolution surface-wave tomography from ambient seismic noise. Science, 307(5715): 1615-1618.

Yao H, Van Der Hilst R D, De Hoop M V. 2006. Surface‐wave array tomography in SE Tibet from ambient seismic noise and two‐station analysis‐I. Phase velocity maps. Geophys J Int, 166(2): 732-744.

Shear-wave anisotropy in northeast part of Tibetan Plateau

Yuan Gao, Qiong Wang, Yutao Shi
Institute of Earthquake Science, China Earthquake Administration, Beijing, China.

Summary

This study adopts shear-wave splitting from local events in the upper-middle crust, splitting of XKS (SKS, PKS and SKKS) phases to detect seismic anisotropy in the lithosphere and asthenosphere as well as receiver functions from teleseismic events to detect seismic anisotropy in the whole crust. Seismic anisotropy in the northeast margin of Tibetan Plateau shows anisotropy in the crust is almost equal to that in the upper mantle.

Introduction

Tibetan Plateau intensely lifts within the Himalayan tectonic evolution. With the tectonic process, strong seismic anisotropy were observed by different reserachers. There are many large active faults and strong earthquakes in the northeast margin of Tibetan Plateau, where is located in convergence zone among the Tibetan block, Alxa block, Ordos block and South-China block. Shear-wave splitting is one of very effective ways to detect Shear-wave anisotropy in the crust and in the mantle. In addition, receiver functions also always are adopted to detect seismic anisotropy. In our studies, shear-wave splitting, as well as receiver functions, are applied to analyze seismic anisotropy in northeast part of Tibetan Plateau.

Theory and/or Method

In northeastern edge of Tibetan Plateau, the crust movement from GPS data is clearly towards NE and NEE, as well as rotation clockwise. However it is unclear of the deep deformation. We have known that lithospheric deformation and asthenospheric flow, also including typical structure, can lead to observed seismic anisotropy in the upper mantle.

Many studies suggest seismic anisotropy is effective to detect the stress, deformation and movement process in the crust and also in the mantle. We adopt shear-wave splitting from local events to detect seismic anisotropy in the upper-middle crust, adopt receiver functions from teleseismic events to extract seismic anisotropy in the whole crust. And we also use splitting of XKS (SKS, PKS and SKKS) phases to detect seismic anisotropy in the lithosphere and asthenosphere, i.e. upper mantle plus crust. GPS data are also adopted to analyze surface movement and compare to deep deformation by seismic anisotropy.

Conclusions

Results from shear-wave splitting in the crust and XKS splitting indicate the anisotropic pattern in the west part in the northeast margin of Tibetan Plateau is different to that in the east part. Polarizations of fast shear-wave in the west part are quite different to that in the east part, which are some related to GPS pattern. The fast direction of XKS shows coherent characteristics between the west part and the east part.
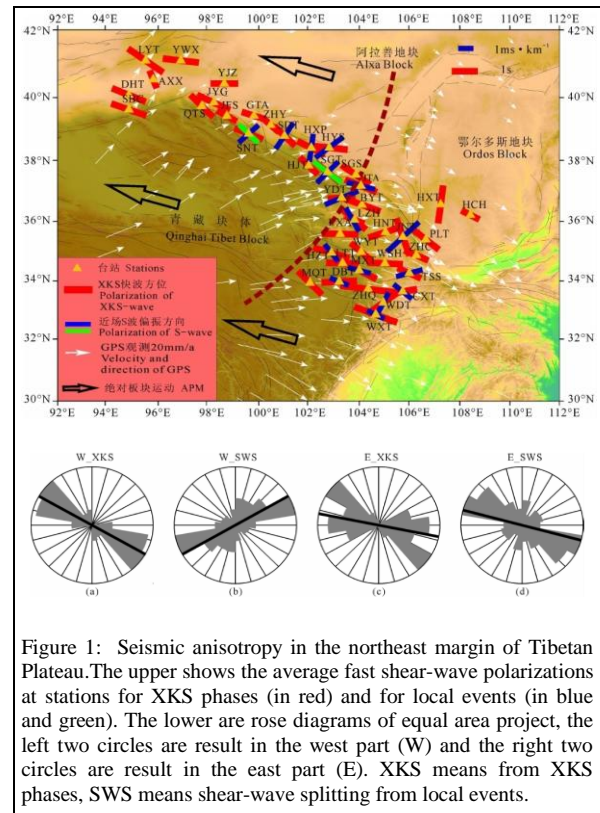
Figure 1: Seismic anisotropy in the northeast margin of Tibetan Plateau.The upper shows the average fast shear-wave polarizations at stations for XKS phases (in red) and for local events (in blue and green). The lower are rose diagrams of equal area project, the left two circles are result in the west part (W) and the right two circles are result in the east part (E). XKS means from XKS phases, SWS means shear-wave splitting from local events.

Anisotropy in NE Tibetan Plateau

We also obtained seismic anisotropy from receiver functions data and found significant azimuthal anisotropy within the crust beneath stations, with a splitting time between about 0.36s and 1.06s, for average 0.6s. The fast polarization directions aligned well with surface structures and consistent to the directions the fast XKS phase. However, the splitting time from XKS phases, i.e. time delay between fast and slow phase, was an average splitting time of 1.2s. It suggests the crustal anisotropy occupied heavy weight in seismic anisotropy in the crust-mantle system. At least, it is an observed phenomenon in the northeast margin of Tibetan Plateau. In addition, the time delays of shear-wave splitting of local events were at about average of 0.2s, which showed seismic anisotropy in the upper crust or upper-middle crust. Anisotropy in the crust is almost equal to that in the upper mantle.

REFERENCE CHANGE:

Gao, Y., Wu, J., Fukao, Y., et al., 2011. Shear-wave splitting in the crust in North China: stress, faults and tectonic implications. Geophys. J. Int., 187: 642-654.

Wang, Q., Niu, F. & Gao, Y., et al., 2016. Crustal structure and deformation beneath the NE margin of the Tibetan plateau constrained by teleseismic receiver function data. Geophys. J. Int., 204, 167-179.

Zhang, H., Gao, Y., Shi, Y., et al., 2012. Tectonic stress analysis based on the crustal anisotropy in the northeastern margin of Tibetan plateau. Chinese J. Geophys. (in Chinese), 55(1), 95-104.

Velocity model smoothing in orthorhombic media

Alexey Stovas and Shibo Xu, NTNU, Norway

Summary

Certain degree of smoothness of velocity model is required for most ray based migration and tomography. Applying the conventional smoothing in model parameters results in the offset-dependent traveltime errors for reflected events, which can be large even for small contrasts in model parameters between the layers. This causes the shift in both the depth and residual moveout (RMO) of the migrated images. To overcome this problem in transversely isotropic medium with a vertical symmetry axis (VTI), the preserved traveltime smoothing (PTS) method was proposed earlier. We extend this method for orthorhombic media with and without azimuthal variation between the layers. We illustrate this method for a single interface between two orthorhombic layers.

Introduction

The velocity models for prestack depth migration (PSDM) are commonly built by layer-stripping with velocity discontinuities across the horizons. The ray tracing used in Kirchhoff or bean migration requires certain smoothness of the depth velocity model. Current industrial practice for smoothing is to perform a bell-shaped filter (Gonzalez and Woods 2008) to the step of model parameters. The drawback of the conventional smoothing is that the migrated events will shift to higher velocity layer at the discontinuities compared with results from the unsmoothed model. The errors in depth and the residual moveout (RMO) for the migrated images are induced by the smoothing process, which will cause errors in velocity analysis. Several approaches are proposed for this problem like adding the horizons in the ray-tracing process (Vinje et al. 1996) and combing the unsmoothed and smoothed models (Baina et al. 2006). The preserved traveltime smoothing (PTS) (Vinje et al. 2012) is proposed to solve this problem for TI media. It is designed to smooth the depth models preserving the traveltime parameters at the velocity discontinuities. The orthorhombic (ORT) medium is introduced by Schoenberg and Helbig (1997) to describe the fractured earth and has become a new standard to define model parameters to cover the azimuthal dependence of the traveltime surface. Tsvankin (1997) defines the elastic ORT model with nine parameters that can be reduced to six parameters in an acoustic approximation (Alkhalifah 2003). These parameters are vertical velocity, two NMO velocities defined in vertical symmetry planes and three anelliptic parameters. The anelliptic parameters can be defined in all symmetry planes (Grechka and Tsvankin 1999) or can be defined in terms of azimuthally dependent anellipticity (Stovas 2015). In addition to that, we might have one extra parameter responsible for azimuthal orientation of the symmetry planes. In this paper, we extend the PTS method to ORT model based on the azimuthal dependence of kinematic properties defined for an acoustic ORT medium (Stovas 2015) to preserve the traveltime parameters for smoothed ORT model. In case of azimuthal variations in the symmetry axis between the layers, the least-squares approximation is adopted to estimate the effective anellipticity parameters from this layered medium. The traveltime parameters are preserved for the azimuthally dependent ORT model, and the resulting error in traveltime is sufficiently small from the numerical examples. In our paper, we focus on defining the composite parameters only and use very simple Gaussian smoothing filter.

Preserved traveltime smoothing in VTI media

The idea behind the PTS smoothing in VTI media (Vinje et al., 2012) is to apply the smoothing for velocity moments,

$$n_1 = 1/V_0, \quad n_2 = V_{nmo}^2/V_0, \quad n_3 = V_{nmo}^4(1+8\eta)/V_0, \tag{1}$$

where V_0, V_{nmo} are the vertical and NMO velocities, and η is anelliptic parameter. The smoothed velocity moments $\tilde{n}_1$, $\tilde{n}_2$ and $\tilde{n}_3$ can be converted back into original parameter space by

$$\tilde{V}_0 = 1/\tilde{n}_1, \quad \tilde{V}_{nmo} = \sqrt{\tilde{n}_2/\tilde{n}_1}, \quad \tilde{\eta} = \left(\tilde{n}_3\tilde{n}_1 - \tilde{n}_2^2\right)/8\tilde{n}_2^2. \tag{2}$$

If the initial velocity model is isotropic, the PTS method results in smoothing-induced anisotropy.

Preserved traveltime smoothing in ORT media

For ORT model without azimuthal variations between the layers, the velocity moments are very similar to VTI case,

$$n_1 = 1/V_0, \quad n_2 = V_{nmo1}^2/V_0, \quad n_3 = V_{nmo1}^4(1+8\eta_1)/V_0, \tag{3}$$

$$n_4 = V_{nmo2}^2/V_0, \quad n_5 = V_{nmo2}^4(1+8\eta_2)/V_0, \quad n_6 = V_{nmo1}^2 V_{nmo2}^2(1+4\eta_{xy})/V_0$$

where (Stovas, 2015)

$$\eta_{xy} = \sqrt{(1+2\eta_1)(1+2\eta_2)/(1+2\eta_3)} - 1, \tag{4}$$

with η_3 being the anelliptic parameter in horizontal symmetry plane. The conversion from the smoothed parameters into the model space is very similar to the VTI case. For ORT model with azimuth variations between the layers, there are nine velocity moments to be smoothed. The first four velocity moments are used to compute the vertical velocity, two NMO velocities and azimuth orientation. Remaining five velocity moments are used to compute three anelliptic parameters by least-squares method (Stovas, 2015).

Numerical examples

To illustrate the PTS method for ORT models, we select one interface between two ORT layers with parameters:
$V_0 = 1.5\,km/s$, $V_{nmo1} = 2\,km/s$, $V_{nmo2} = 1.8\,km/s$, $\eta_1 = 0.1$,

$\eta_2 = 0.12$ and $\eta_{xy} = 0.22$ (upper layer) and $V_0 = 2\,km/s$, $V_{nmo1} = 2.5\,km/s$, $V_{nmo2} = 2.2\,km/s$, $\eta_1 = 0.12$, $\eta_2 = 0.15$ and $\eta_{xy} = 0.2$ (lower layer). The result of application of PTS with Gaussian smoothing operator on ORT model with no azimuthal variations is shown in Figure 1. One can see that the shape of the smoothed velocities is very similar, while the behavior of the smoothed anelliptic parameters is slightly different (for example, different magnitude of overshooting at the interface). The result of application of PTS for ORT model (with parameters listed above and 30 degrees azimuth variation) is shown in Figure 2. One can see (comparing with Figure 1) that the presence of azimuth has minor effect on NMO velocities, but significantly affects the anelliptic parameters.
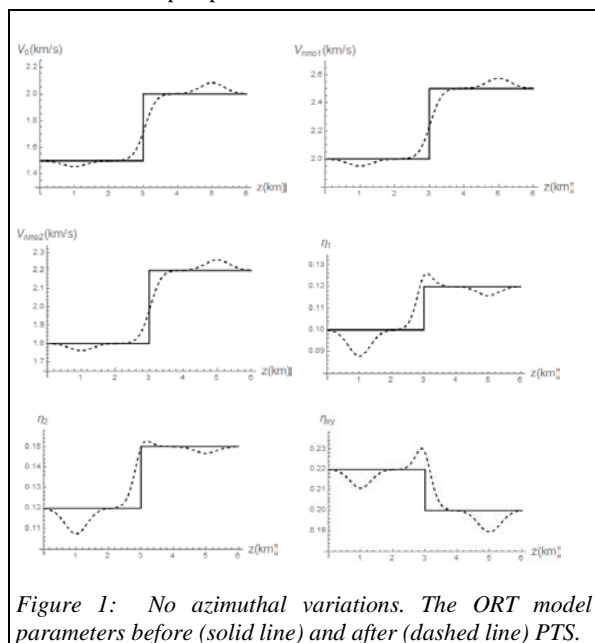
Figure 1: No azimuthal variations. The ORT model parameters before (solid line) and after (dashed line) PTS.

Conclusions

We develop the preserved traveltime smoothing method for orthorhombic velocity model with and without azimuth variations between the layers. The method is based on the smoothing of velocity moments.

References

Alkhalifah T. 2003. An acoustic wave equation for orthorhombic anisotropy. *Geophysics* **68**, 1169-1172.

Baina R., Zamboni E. and Lambaré G. 2006. How to cope with smoothing effect in ray based PSDM. 68th EAGE Conference & Exhibition, Extended Abstracts.

Gonzalez R., and Woods R. 2008. Digital Image Processing, 3rd edition, Prentice Hall.
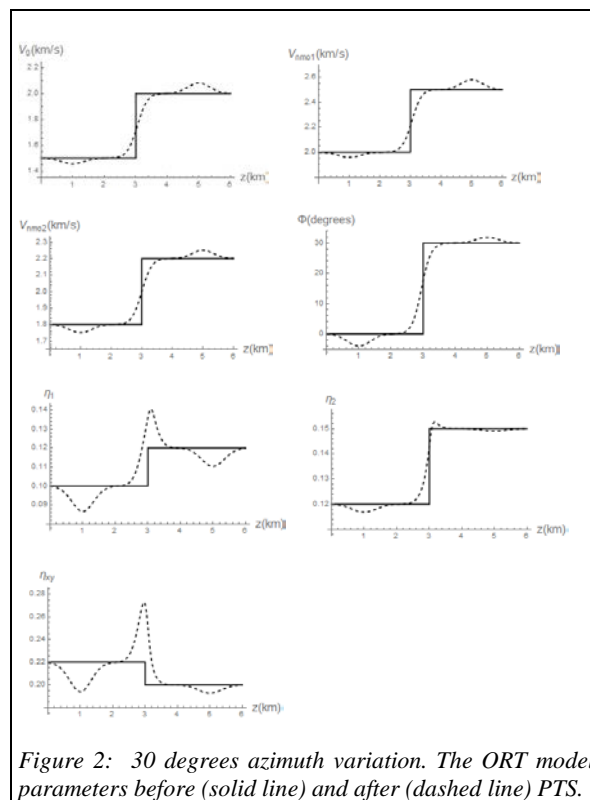
Figure 2: 30 degrees azimuth variation. The ORT model parameters before (solid line) and after (dashed line) PTS.

Grechka V., and Tsvankin I. 1999. 3-D moveout velocity analysis and parameter estimation for orthorhombic media. *Geophysics* **64**, 820–837.

Lailly P., and Sinoquet D. 1996. Smooth velocity models in reflection tomography for imaging complex geological structures: *Geophys. J. Int* **124**, 349-362.

Schoenberg M., and Helbig K. 1997. Orthorhombic media: Modeling elastic wave behavior in a vertically fractured earth: *Geophysics* **62**, 1954–1974.

Song X. and. Alkhalifah T. 2013. Modeling of pseudoacoustic P-waves in orthorhombic media with a low-rank approximation: *Geophysics* **78**, no4, C33–C40.

Stovas A. 2015. Azimuthally dependent kinematic properties of orthorhombic media. *Geophysics* **80**, C107-C122.

Tsvankin, I. 1997. Anisotropic parameters and P-wave velocity for orthorhombic media: *Geophysics* **62**, 1292–1309.

Vinje V. Iversen E. Åstebøl K. and Gjøystdal H. 1996. Estimation of multivalued arrivals in 3D models using wavefront construction, Part I. *Geophysical Prospecting* **44**, 819-842.

Vinje V., Stovas A. and Reynaud D. 2012. Preserved-traveltime smoothing. *Geophysical Prospecting* **61**, 380-390.

Wave propagation, reflection and transmission in tilt orthorhombic media

Yuandi Gan[1], and Evgeni M. Chesnokov[1]
[1] *University of Houston*

SUMMARY

Different tilt angles result in different velocity anisotropy on horizontal and vertical planes. We used Christoffel equation and Schoenberg's solution to calculate phase and group velocity, deviation angle, reflectivity, and transmissivity in tilt orthorhombic media. We got results of phase and group velocities and deviation angle in media with varied tilt angles, and we obtained results of reflectivity and transmissivity of plane-wave for cases in which waves propagate from an isotropic medium to a tilt orthorhombic medium.

INTRODUCTION

We can describe most of them by using tilt transversely isotropic media and tilt orthorhombic media for a simplification and approximation. For a model of orthorhombic medium is more general than one of transversely isotropic medium, our objective is to examine the anisotropy of phase and group velocities and deviation angle in a tilt orthorhombic medium, and reflectivity and transmissivity of plane-wave from an isotropic medium to a tilt orthorhombic medium; as well as to examine how those physical parameters change with variation of tilt angle of a tilt orthorhombic medium.

VELOCITIES AND DEVIATION ANGLE IN TILT ORTHORHOMBIC MEDIA

In this section, we studied phase velocity, group velocity, and deviation angle of wave propagation in the homogeneous tilt orthorhombic medium.

Christoffel equation

Phase velocity in a homogeneous medium may be calculated from the Christoffel equation given by

$$(C_{ijkl}n_j n_l - \rho V^2 \delta_{ik})U_k = 0, \tag{1}$$

where C is the stiffness tensor, **n** is a unit vector which represents the direction of wave propagation, ρ is the density, V is the magnitude of phase velocity, δ is the Kronecker delta function; and **U** represents the direction of particle displacement. Group velocity can be calculated by

$$V_j^{(group)} = \frac{1}{\rho V} C_{ijkl} U_i U_k n_l. \tag{2}$$

Deviation angle is defined as the deviated angle of the polarization in an anisotropic medium from its original direction in an isotropic medium (Mavko et al., 2009).

Table 1: Physical parameters of the orthorhombic medium

C_{11} (GPa)	324.0	C_{22} (GPa)	198.0	C_{33} (GPa)	249.0
C_{12} (GPa)	59.0	C_{23} (GPa)	78.0	C_{13} (GPa)	79.0
C_{44} (GPa)	81.0	C_{55} (GPa)	66.7	C_{66} (GPa)	79.0
ρ (kg/m^3)	3300				
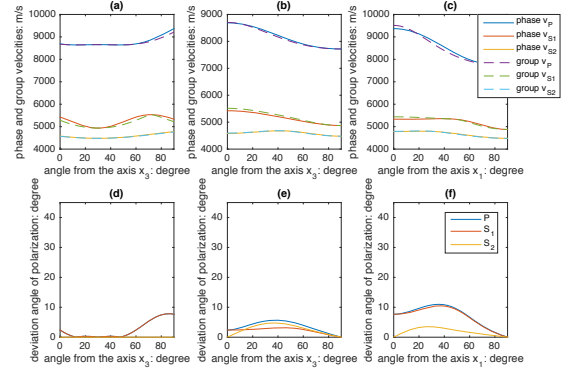
Figure 1: Phase and group velocities (a,b,c) and deviation angle (d,e,f) in tilt orthorhombic medium with tilt angle equal to $30°$ on (a,d) coordinate plane containing x_1 and x_3, (b,e) coordinate plane containing x_2 and x_3, and (c,f) coordinate plane containing x_1 and x_2

Numerical models

We used numerical models to show the phase velocity, group velocity, and deviation angle in tilt orthorhombic media. We obtained a tilt orthorhombic medium by rotating a horizontal orthorhombic medium. The physical parameters of the horizontal orthorhombic medium is shown in Table 1 (Keith and Crampin, 1977).

The stiffness of the tilt orthorhombic medium is calculated from that of the horizontal orthorhombic medium by using Bond transformation method (Auld, 1990). Figure 1 and Figure 2 show those in tilt orthorhombic media with tilt angle equal to $30°$ and $60°$, respectively.

REFLECTION AND TRANSMISSION IN TILT ORTHORHOMBIC MEDIUM

We studied reflection and transmission of plane waves from an isotropic medium to a tilt orthorhombic medium in this section.

### Calculation of reflectivity and transmissivity in anisotropic media
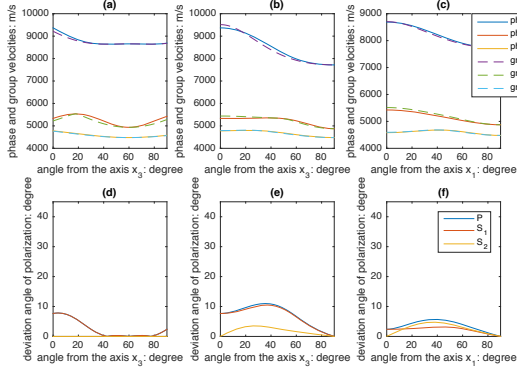
Figure 2: Phase and group velocities (a,b,c) and deviation angle (d,e,f) in tilt orthorhombic medium with tilt angle equal to 60° on (a,d) coordinate plane containing x_1 and x_3, (b,e) coordinate plane containing x_2 and x_3, and (c,f) coordinate plane containing x_1 and x_2

Schoenberg and Protazio (1990) give solutions of reflectivity and transmissivity for the plane-wave reflection and transmission problem. Reflectivity and transmissivity are expressed in terms of stiffness, slowness, and polarization vector. We assumed two horizontal components of slowness are known, we solved for the vertical component slowness by using Equation (1). We then substituted the slowness into Schoenberg's solution to get reflectivity and transmissivity.

Reflectivity and transmissivity of plane waves propagating from an isotropic medium to a tilt orthorhombic medium

We used a numerical model to examine the reflectivity and transmissivity for varied incident angles and varied tilt angles of tilt orthorhombic media. The model consisted of two half spaces and one interface between them. The upper half space was an isotropic medium; its physical parameters were shown in Table 2. The lower half space was a tilt orthorhombic medium; its stiffness tensor was obtained by rotating a horizontal orthorhombic stiffness tensor using Bond transformation. We used P-wave as incident waves, and the reflected and transmitted waves include P-, S_1-, and S_2 waves. Figure 3 and Figure 4 respectively show reflectivity and transmissivity as a function of incident angle for the cases in which tilt angle of the lower half space equal to 0°, 30°, 60°, 90°.

DISCUSSION

Base on the algorithm of reflectivity and transmissivity of an interface between two anisotropic media, our future work will involve multilayers. We are working on the synthetic seismic diagram of a randomly layered medium consisting of tilt anisotropic layers and porous anisotropic layers.

Table 2: Physical parameters of the isotropic medium

P-wave velocity (km/s)	10.00
S-wave velocity (km/s)	5.77
density (kg/m^3)	3600
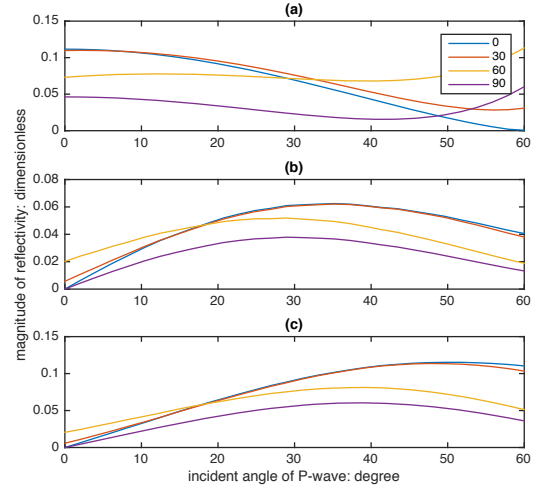
Figure 3: Reflectivity as a function of incident angle of P-wave incidence for varied tilt angles of the lower half space: (a) reflected P-wave, (b) reflected S_1-wave, (c) reflected S_2-wave
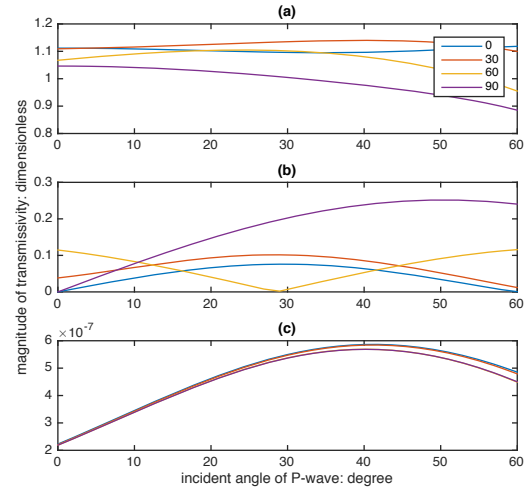
Figure 4: Transmissivity as a function of incident angle of P-wave incidence for varied tilt angles of the lower half space: (a) transmitted P-wave, (b) transmitted S_1-wave, (c) transmitted S_2-wave

REFERENCES

Auld, B. A., 1990, Acoustic fields and waves in solids: RE Krieger, **2**.

Keith, C. M., and S. Crampin, 1977, Seismic body waves in anisotropic media: reflection and refraction at a plane interface: Geophysical Journal International, **49**, 181–208.

Mavko, G., T. Mukerji, and J. Dvorkin, 2009, The rock physics handbook: Tools for seismic analysis of porous media: Cambridge University Press.

Schoenberg, M., and J. Protazio, 1990, zoeppritz rationalized, and generalized to anisotropic media: The Journal of the Acoustical Society of America, **88**, S46–S46.

On the algebraic degree of general group-velocity surface

Vladimir Grechka (Marathon Oil Company)

Summary

This paper establishes the values of three apparently unknown at present quantities: the algebraic degree, $\mathfrak{D}$, of general group-velocity surface (or elementary wavefront), the maximum number, $\mathfrak{B}$, of plane body waves that can propagate along a ray in a homogeneous anisotropic solid, and the maximum number, $\mathfrak{C}_{\tilde{s}}$, of isolated, singularity-unrelated saddle-shaped regions of an elementary wavefront.

Introduction

Three algebraic surfaces play fundamental role in the theory of seismic wave propagation in anisotropic media: the slowness surface, the phase-velocity surface, and the group-velocity surface. The slowness and phase-velocity surfaces are fairly simple, and their algebraic orders or degrees, defined as the orders of the polynomials representing the surfaces, are known to be equal to 6 and 12, respectively (e.g., Fedorov, 1968; Musgrave, 1970). The group-velocity surfaces, $\Phi(\boldsymbol{g})$, describing elementary wavefronts in anisotropic media, are much more complex; they are complex to the extent that only the upper bound of their degree, $\mathfrak{D} \equiv \deg[\Phi(\boldsymbol{g})] \leq 150$ (Musgrave, 1954, 1970; Fedorov, 1968), is currently available.

Here, $\mathfrak{D}$ is derived as a by-product of solving a system of polynomial equations that express surface $\Phi(\boldsymbol{g})$ as a function of its radius vector, subsequently making it possible to establish the value of $\mathfrak{B}$.

Improved upper bound for $\mathfrak{D}$

To obtain the group-velocity vector $\boldsymbol{g}$ of a plane body wave, one would typically specify the unit wavefront normal $\boldsymbol{n}$, solve the Christoffel equation

$$\boldsymbol{\Gamma}(\boldsymbol{n}) \cdot \boldsymbol{U} = V^2 \boldsymbol{U} \qquad (1)$$

for the phase velocity V and the unit polarization vector $\boldsymbol{U}$, and calculate $\boldsymbol{g}$ by applying its definition

$$\boldsymbol{g} = \boldsymbol{\Gamma}(\boldsymbol{U}) \cdot \frac{\boldsymbol{n}}{V}, \qquad (2)$$

where

$$\boldsymbol{\Gamma}(\boldsymbol{n}) \equiv \boldsymbol{n} \cdot \boldsymbol{a} \cdot \boldsymbol{n} \ \ \text{and} \ \ \boldsymbol{\Gamma}(\boldsymbol{U}) \equiv \boldsymbol{U} \cdot \boldsymbol{a} \cdot \boldsymbol{U} \qquad (3)$$

are the 3×3 Christoffel tensors, $\boldsymbol{a}$ is the $3 \times 3 \times 3 \times 3$ density-normalized stiffness tensor, and dots denote the dot products.

Equations 1 and 2 can be used to express $\boldsymbol{g}$ as a function of its unit radius vector or ray $\boldsymbol{r} \equiv \boldsymbol{g}/|\boldsymbol{g}|$. To compute $\boldsymbol{g}(\boldsymbol{r})$ or, more precisely, $\boldsymbol{n}(\boldsymbol{r})$ and $\boldsymbol{U}(\boldsymbol{r})$ and then $\boldsymbol{g}(\boldsymbol{r})$ from equation 2, it is convenient to rotate the quantities appearing in equations $1 - 3$ to a coordinate frame in which $\boldsymbol{r} = [0, 0, 1]$, take a cross product of $\boldsymbol{r}$ and equation 2,

$$\left\{\boldsymbol{r} \times \left[\boldsymbol{\Gamma}(\boldsymbol{U}) \cdot \boldsymbol{n}\right]\right\}_i = 0, \quad (i = 1, 2) \qquad (4)$$

and eliminate V^2 from equations 1,

$$\left\{\boldsymbol{U} \times \left[\boldsymbol{\Gamma}(\boldsymbol{n}) \cdot \boldsymbol{U}\right]\right\}_i = 0, \quad (i = 1, 2). \qquad (5)$$

Polynomials 4, 5 comprise a system of four algebraic equations for four unknown components of vectors $\tilde{\boldsymbol{n}} \equiv \boldsymbol{n}/n_3$ and $\tilde{\boldsymbol{U}} \equiv \boldsymbol{U}/U_3$.

Equations 4, linear in the components of $\tilde{\boldsymbol{n}}$, are easily solvable, yielding

$$\tilde{n}_i = \frac{\displaystyle\sum_{j,\,k=0}^{j+k\,\leq\,4} \alpha_{jk}^{(i)} \, \tilde{U}_1^j \, \tilde{U}_2^k}{\displaystyle\sum_{j,\,k=0}^{j+k\,\leq\,4} \beta_{jk} \, \tilde{U}_1^j \, \tilde{U}_2^k}, \quad (i = 1, 2), \qquad (6)$$

where the coefficients $\alpha_{jk}^{(i)}$ and β_{jk} are functions of the components of stiffness tensor $\boldsymbol{a}$ in the rotated coordinate frame. Importantly, both numerators and denominator in 6 are at most quartic polynomials in $\tilde{U}_i$, $(i = 1, 2)$, making the degree of each equation 5 at most 10 and the degree of system 4, 5 as a whole at most 100 – an improvement over the bound 150 established by Musgrave (1954, 1970) and Fedorov (1968).

The theoretically derived degree of $\Phi(\boldsymbol{g})$ is an upper bound, $\mathfrak{D} \leq 100$, tighter than the classic bound, $\mathfrak{D} \leq 150$, but still a bound. This becomes obvious when one takes into account the central symmetry of group-velocity surfaces and recognizes that $\deg[\Phi(\boldsymbol{g})] = 100$, being divisible by 4, entails the topologically implausible *even* number of body waves propagating along a ray. Hence, some high-degree monomials in equations 4 and 5 necessarily vanish.

Degree of $\Phi(\boldsymbol{g})$

To find out the number of identically zero monomials, system 4, 5 has been solved for numerous randomly generated triclinic models, always resulting in 43 real- and complex-valued quadruplets $\tilde{n}_i$ and $\tilde{U}_i$, $(i = 1, 2)$ and implying the degree of general group-velocity surface to be equal to $\mathfrak{D} = 43 \times 2 = 86$.

$\mathfrak{D}$, $\mathfrak{B}$, and cusps

The knowledge of $\mathfrak{D}$ makes it possible to establish the maximum number, $\mathfrak{B}$, of plane body waves that can propagate along a ray in a homogeneous anisotropic medium or, stating the same problem mathematically, to determine the maximum number of real-valued roots of system 4, 5 that satisfy the inequality $\boldsymbol{r} \cdot \boldsymbol{n} > 0$ imposed by the elastic stability conditions. Clearly,

$$\mathfrak{B} = \frac{\mathfrak{D} - \mathfrak{C}}{2}, \qquad (7)$$

where $\mathfrak{C}$ is maximum number of degeneracies of $\Phi(\boldsymbol{g})$ that give rise to $\mathfrak{C}/2$ irremovable complex-valued roots of equations 4 and 5.

Degeneracies of $\Phi(\boldsymbol{g})$ – the cusps formed at borders of saddle-shaped regions of $\Phi(\boldsymbol{g})$ separating its areas of positive and negative Gaussian curvature (Musgrave, 1954) – can be split into the singularity-related, $\mathfrak{C}_s$, and singularity-unrelated, $\mathfrak{C}_{\tilde{s}}$, degeneracies,

$$\mathfrak{C} = \mathfrak{C}_s + \mathfrak{C}_{\tilde{s}}, \qquad (8)$$

equal to the maximum numbers of the corresponding iso-
lated saddle-shaped (or hyperbolic) regions of $\Phi(\boldsymbol{g})$.

The quantity $\mathfrak{C}_s$ is exactly the maximum number of singu-
larities (defined as the wavefront normals $\boldsymbol{n}_s$ along which
the phase velocities of two plane body waves coincide)
because a general (conical) singularity is always accom-
panied by a cusp. The maximum number of singularities
is 16 (e.g., Holm, 1992; Darinskii, 1994) if the centrally
symmetric vectors $+\boldsymbol{n}_s$ and $-\boldsymbol{n}_s$ are counted as a single
direction; therefore, $\mathfrak{C}_s = 16 \times 2 = 32$.

The quantity $\mathfrak{C}_{\tilde{s}}$ in equation 8 is to be determined.

Quantity $\mathfrak{C}_{\tilde{s}}$

Anisotropic media without singularities are extremely un-
usual and possibly do not exist in nature. Yet, Alshits and
Lothe (1979) discovered that such artificial solids could be
constructed if values of diagonal stiffness elements com-
posing the triplets $\{a_{11}, a_{22}, a_{33}\}$ and $\{a_{44}, a_{55}, a_{66}\}$ are
allowed to intermix. For instance, orthorhombic medium
that has the diagonal stiffness matrix (in arbitrary veloc-
ity squared units)

$$\boldsymbol{a} = \begin{pmatrix} 18 & 0 & 0 & 0 & 0 & 0 \\ & 8 & 0 & 0 & 0 & 0 \\ & & 50 & 0 & 0 & 0 \\ & & & 11 & 0 & 0 \\ & \text{SYM} & & & 14 & 0 \\ & & & & & 13 \end{pmatrix} \quad (9)$$

is an example of a solid possessing no singularities. The
importance of model 9 lies in exhibiting the maximum
possible number, $\mathfrak{C}_{\tilde{s}} = 16$, of isolated hyperbolic regions
(Figure 1) bordered by the cuspidal edges of $\Phi(\boldsymbol{g})$.

Quantity $\mathfrak{B}$

Substituting the values of $\mathfrak{D}$, $\mathfrak{C}_s$, and $\mathfrak{C}_{\tilde{s}}$ in equations 7
and 8 predicts the maximum number of plane body waves
having the same ray direction to be

$$\mathfrak{B} = \frac{86 - (32 + 16)}{2} = 19 \, . \quad (10)$$

The maximum $\mathfrak{B} = 19$ is reached in strongly anisotropic
media, in which group-velocity surfaces contain pervasive
multiple branches. For example, 19 body waves propagate
along ray $\boldsymbol{r} = [0.548, 0.551, 0.629]$ in a triclinic solid spec-
ified by the stiffness matrix (in arbitrary velocity squared
units)

$$\boldsymbol{a} = \begin{pmatrix} 45.60 & 0.93 & 0.89 & 0.10 & 0.07 & 0.07 \\ & 14.44 & 0.88 & -0.08 & 0.02 & -0.06 \\ & & 44.30 & -0.05 & -0.04 & -0.03 \\ & & & 0.46 & 0.09 & 0.05 \\ & \text{SYM} & & & 0.37 & 0.10 \\ & & & & & 0.45 \end{pmatrix} .$$

Conclusions

The findings of the paper can be summarized as follows:

- Algebraic degree of general group-velocity surface is
  $\mathfrak{D} = 86$.

- The maximum number of plane body waves that
  can propagate along a ray in any homogeneous
  anisotropic medium is $\mathfrak{B} = 19$.

- The maximum number of isolated, singularity-un-
  related hyperbolic regions of $\Phi(\boldsymbol{g})$ is $\mathfrak{C}_{\tilde{s}} = 16$.
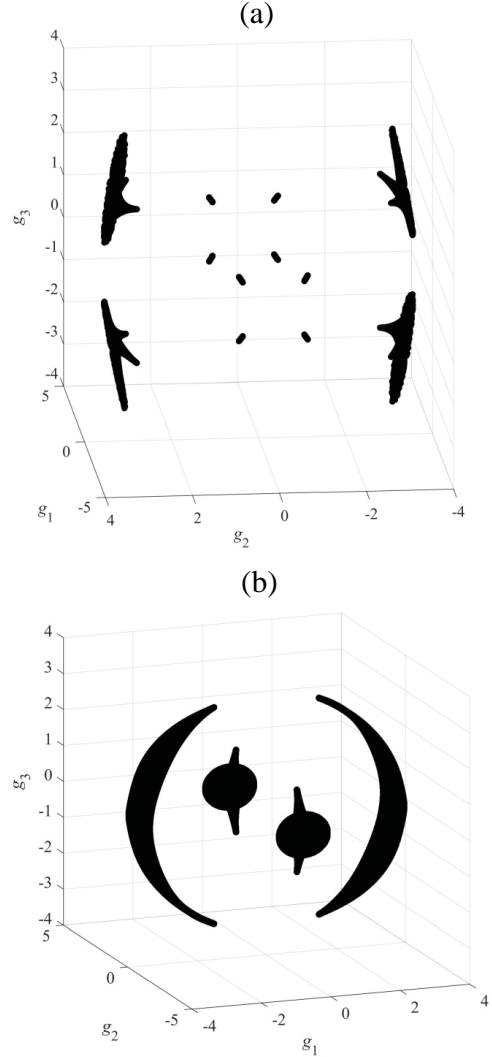
Fig. 1: Hyperbolic regions of group-velocity surfaces of (a) fast
and (b) slow shear-waves in orthorhombic model 9.

Both maxima, $\mathfrak{B} = 19$ and $\mathfrak{C}_{\tilde{s}} = 16$, are demonstratively
realizable.

References

Alshits, V. I., and J. Lothe, 1979, Elastic waves in tri-
clinic crystals. II. Topology of polarization fields and
some general theorems: Soviet Physics, Crystallog-
raphy, **24**, no. 4, 393–398.

Darinskii B. M., 1994, Acoustic axes in crystals: Crys-
tallography Reports, **39**, no. 5, 697–703.

Fedorov, F. I., 1968, Theory of elastic waves in crystals:
Plenum Press (originally in Russian, 1965, Nauka).

Holm, P., 1992, Generic elastic media, Physica Scripta,
T44, 122–127.

Musgrave, M. J. P., 1954, On the propagation of elastic
waves in aeolotropic media. I. General principles:
Proceedings of the Royal Society of London, **A226**,
339–355.

Musgrave, M. J. P., 1970, Crystal acoustics: Holden-Day
(2nd edition, 2003, Acoustical Society of America).

Second- and Fourth-order NMO Velocities in General Anisotropic Horizontally Layered Media

Zvi Koren* and Igor Ravve, Paradigm Geophysical

Summary

We present a method for computing second- and fourth-order azimuthally-dependent normal moveout (NMO) velocity functions $V_2(\psi)$ and $V_4(\psi)$, for quasi pure mode waves, in general anisotropic horizontally layered media, without making any assumption of weak anisotropy. We consider the dependency on both azimuth domains: slowness (phase-azimuth, ψ_{phs}) and acquisition (offset-azimuth, ψ_{off}). The accuracy of the method is tested by setting our derived V_2 and V_4 functions within the azimuthally dependent fractional asymptotic fourth-order traveltime approximation (Alkhalifah and Tsvankin, 1995), and comparing with an exact ray tracing.

Introduction

In previous studies (Ravve and Koren, 2016, and Koren and Ravve, 2016) we suggested a method to construct azimuthally-dependent second- and fourth-order NMO velocity functions in the phase-azimuth and offset-azimuth domains from eight global moveout coefficients, obtained by a Dix-like summation over the corresponding local coefficients of the individual layers. Note that the computation of the eight local parameters requires calculating ray velocity components which depend on the type of anisotropy of the given layers, while the method for computing the eight global parameters (Dix-like summation) is generic. In this work we consider pure-mode waves (compressional or shear), so that the traveltime expansion includes even functions of offset only.

Derivation Workflow

We introduce the following three moveout components: radial-offset h_R, along a given phase-azimuth, transverse-offset h_T in the normal direction, and the corresponding two-way time t. For a given layer their calculation requires computing the three ray velocity components for the incidence and reflected rays,

$$\frac{\Delta h_R}{\Delta z} = \frac{v_{ray,R}^{re}}{v_{ray,3}^{re}} - \frac{v_{ray,R}^{in}}{v_{ray,3}^{in}} \ , \qquad \frac{\Delta t}{\Delta z} = \frac{1}{v_{ray,3}^{re}} + \frac{1}{v_{ray,3}^{in}} \quad (1)$$

$$\frac{\Delta h_T}{\Delta z} = \frac{v_{ray,T}^{re}}{v_{ray,3}^{re}} - \frac{v_{ray,T}^{in}}{v_{ray,3}^{in}} \ ,$$

where, Δz is the layer thickness, and the radial and transverse ray velocity components are

$$v_{ray,R} = +v_{ray,1}\cos\psi_{phs} + v_{ray,2}\sin\psi_{phs} \ , $$
$$v_{ray,T} = -v_{ray,1}\sin\psi_{phs} + v_{ray,2}\cos\psi_{phs} \ . \qquad (2)$$

For a given phase-azimuth ψ_{phs} and horizontal slowness p_h, the three moveout components can be written in the following series expansion,

$$\Delta h_R = u_2\,p_h - \left(w_{2x}\cos2\psi_{phs} + w_{2y}\sin2\psi_{phs}\right)p_h$$
$$+ u_4 p_h^3 + \left(w_{42x}\cos2\psi_{phs} + w_{42y}\sin2\psi_{phs}\right)p_h^3$$
$$+ \left(w_{44x}\cos4\psi_{phs} + w_{44y}\sin4\psi_{phs}\right)p_h^3 + O\!\left(p_h^5\right).$$

$$\Delta h_T = \left(w_{2x}\sin2\psi_{phs} - w_{2y}\cos2\psi_{phs}\right)p_h$$
$$- \frac{1}{2}\left(w_{42x}\sin2\psi_{phs} - w_{42y}\cos2\psi_{phs}\right)p_h^3 \qquad (3)$$
$$- \left(w_{44x}\sin4\psi_{phs} - w_{44y}\cos4\psi_{phs}\right)p_h^3 + O\!\left(p_h^5\right).$$

$$\Delta t - \Delta t_o = \frac{1}{2}u_2 p_h^2 - \frac{1}{2}\left(w_{2x}\cos2\psi_{phs} + w_{2y}\sin2\psi_{phs}\right)\times$$
$$\times p_h^2 + \frac{3}{4}u_4 p_h^4 + \frac{3}{4}\left(w_{42x}\cos2\psi_{phs} + w_{42y}\sin2\psi_{phs}\right)p_h^4$$
$$+ \frac{3}{4}\left(w_{44x}\cos4\psi_{phs} + w_{44y}\sin4\psi_{phs}\right)p_h^4 + O\!\left(p_h^6\right).$$

Coefficients $u_2, w_{2x}, w_{2y}, u_4, w_{42x}, w_{42y}, w_{44x}, w_{44y}$ are too long to be listed in this abstract.

For an individual layer it is easier to work with the opening angle γ_{phs} between the incidence and reflection phase velocities, rather than with the horizontal slowness p_h. Then we apply the two-way azimuthally-dependent relationships between p_h and γ_{phs}. We introduce the following notations: v_{ver}, the vertical phase velocity, and $v'_{ver}, v''_{ver}\ldots$, the first, the second, etc. derivatives of the phase velocity magnitude with respect to zenith angle, computed for the normal incidence ray (with vanishing zenith angle of the phase velocity). Thus $v'_{ver}, v''_{ver}\ldots$ are functions of the phase-azimuth alone. The two rays are assumed emerging from the reflection point. Thus, their azimuths differ by π. The azimuth of the reflection ray is ψ_{phs}, and the azimuth of the incidence ray is $\psi_{phs}+\pi$. We apply the following workflow to compute the ray velocities:

- Given the opening angle γ_{phs}, apply Snell's law to find the incidence and reflection angles θ_{phs}^{in} and θ_{phs}^{in} apart,

Second- and Fourth-order NMO Velocities in General Anisotropic Horizontally Layered Media

$$\theta_{\text{phs}}^{\text{in}} = \frac{\gamma_{\text{phs}}}{2} - \frac{v_{\text{phs}}'}{4v_{\text{ver}}}\gamma_{\text{phs}}^2$$

$$- \frac{\left(2v_{\text{phs}}' + v_{\text{phs}}'''\right)v_{\text{phs}}^{\text{ver}2} + 3v_{\text{phs}}'v_{\text{phs}}''v_{\text{ver}} - 6v_{\text{phs}}'^3}{96v_{\text{ver}}^3}\gamma_{\text{phs}}^4 + O\!\left(\gamma_{\text{phs}}^5\right)$$

$$\theta_{\text{phs}}^{\text{re}} = \frac{\gamma_{\text{phs}}}{2} + \frac{v_{\text{phs}}'}{4v_{\text{ver}}}\gamma_{\text{phs}}^2 \tag{4}$$

$$+ \frac{\left(2v_{\text{phs}}' + v_{\text{phs}}'''\right)v_{\text{phs}}^{\text{ver}2} + 3v_{\text{phs}}'v_{\text{phs}}''v_{\text{ver}} - 6v_{\text{phs}}'^3}{96v_{\text{ver}}^3}\gamma_{\text{phs}}^4 + O\!\left(\gamma_{\text{phs}}^5\right)$$

- For each of the two rays, whose phase direction is now specified by two spherical angles (zenith and azimuth), find the phase velocity magnitude and the derivatives of this magnitude with respect to zenith and azimuth

$$v_{\text{phs}}^{\text{in}} = v_{\text{phs}}^{\text{ver}} - v_{\text{phs}}'\frac{\gamma_{\text{phs}}}{2} + \frac{v_{\text{phs}}^{\text{ver}}v_{\text{phs}}'' + 2v_{\text{phs}}'^2}{v_{\text{phs}}^{\text{ver}}}\frac{\gamma_{\text{phs}}^2}{8}$$

$$- \frac{v_{\text{phs}}^{\text{ver}}v_{\text{phs}}''' + 6v_{\text{phs}}'v_{\text{phs}}''}{v_{\text{phs}}^{\text{ver}}}\frac{\gamma_{\text{phs}}^3}{48}$$

$$+ \frac{v_{\text{phs}}''''v_{\text{phs}}^{\text{ver}3} + 8\left(v_{\text{phs}}' + 2v_{\text{phs}}'''\right)v_{\text{phs}}'v_{\text{phs}}^{\text{ver}2}}{v_{\text{phs}}^{\text{ver}3}}\frac{\gamma_{\text{phs}}^3}{384}$$

$$+ \frac{24v_{\text{phs}}'^2\left(v_{\text{phs}}''v_{\text{phs}}^{\text{ver}} - v_{\text{phs}}'^2\right)}{v_{\text{phs}}^{\text{ver}3}}\frac{\gamma_{\text{phs}}^3}{384} + O\!\left(\gamma_{\text{phs}}^5\right),$$

$$v_{\text{phs}}^{\text{re}} = v_{\text{phs}}^{\text{ver}} + v_{\text{phs}}'\frac{\gamma_{\text{phs}}}{2} + \frac{v_{\text{phs}}^{\text{ver}}v_{\text{phs}}'' + 2v_{\text{phs}}'^2}{v_{\text{phs}}^{\text{ver}}}\frac{\gamma_{\text{phs}}^2}{8}$$

$$+ \frac{v_{\text{phs}}^{\text{ver}}v_{\text{phs}}''' + 6v_{\text{phs}}'v_{\text{phs}}''}{v_{\text{phs}}^{\text{ver}}}\frac{\gamma_{\text{phs}}^3}{48}$$

$$+ \frac{v_{\text{phs}}''''v_{\text{phs}}^{\text{ver}3} + 8\left(v_{\text{phs}}' + 2v_{\text{phs}}'''\right)v_{\text{phs}}'v_{\text{phs}}^{\text{ver}2}}{v_{\text{phs}}^{\text{ver}3}}\frac{\gamma_{\text{phs}}^3}{384}$$

$$+ \frac{24v_{\text{phs}}'^2\left(v_{\text{phs}}''v_{\text{phs}}^{\text{ver}} - v_{\text{phs}}'^2\right)}{v_{\text{phs}}^{\text{ver}3}}\frac{\gamma_{\text{phs}}^3}{384} + O\!\left(\gamma_{\text{phs}}^5\right). \tag{5}$$

- Apply the phase velocity and its derivatives to compute the Cartesian components of the ray velocity

We omit here the relationships for the derivatives of the phase velocity magnitude computed for the directions of the incidence and reflection rays, and the ray velocity components. Their structure is similar to that of the incidence and reflection angles in equation 5. They are series of the opening angle whose coefficients depend on the derivatives of the phase velocity with respect to zenith angle, up to order four, computed for the normal incidence ray, $v_{\text{phs}}', v_{\text{phs}}'', v_{\text{phs}}''', v_{\text{phs}}''''$. These derivatives, in turn, are functions of the phase-azimuth. In the series expansion, the opening angle is assumed a small parameter, i.e., nearly-vertical rays are being studied. Finally, we replace the opening angle with the horizontal slowness, applying

$$p_h = \frac{\gamma_{\text{phs}}}{2v_{\text{ver}}} - \frac{v_{\text{ver}}^2 + 3v_{\text{ver}}''v_{\text{ver}} + 6v_{\text{ver}}'^2}{v_{\text{ver}}^3}\frac{\gamma_{\text{phs}}^3}{48} + O\!\left(\gamma_{\text{phs}}^5\right) \tag{6}$$

$$\gamma_{\text{phs}} = 2v_{\text{ver}}p_h + v_{\text{ver}}\!\left(v_{\text{ver}}^2 + 3v_{\text{ver}}''v_{\text{phs}}^{\text{ver}} + 6v_{\text{ver}}'^2\right)\frac{p_h^3}{3} + O\!\left(p_h^5\right).$$

Since derivatives of the phase velocity up to the fourth-order are needed, then, in the proximity of the normal-incidence ray, the phase velocity is approximated by a smooth fourth-order surface defined by 15 coefficients. Each of them, in turn, may be computed from the coefficients of the Christoffel matrix. Eventually, these 15 coefficients are combined into 8 local moveout coefficients.

Tilted Orthorhombic Anisotropy

Tilted Orthorhombic (TOR) anisotropy becomes an important representation of tilted compacted sediment layers with orthogonal sets of fractures. We suggest two ways to compute the moveout coefficients of a TOR layer: a) rotate the layer to global axes and treat it as triclinic b) compute the coefficients in its local tilted frame. The results are, of course, identical.

Conclusions

We derived new relations for the second- and fourth-order azimuthally dependent NMO velocities for multi-layer triclinic media in the phase-azimuth and offset-azimuth domains. We obtain three low-order and five high-order local and global effective parameters, which are related by simple forward and inverse Dix-like transforms. The local coefficients depend on the stiffness matrix and layer thickness.

References

Alkhalifah, T., and I. Tsvankin, 1995, Velocity analysis for transversely isotropic media: *Geophysics*, 60, 1550-1566.

Ravve, I., and Z. Koren, 2016, Fourth-order NMO velocity for P-waves in layered orthorhombic media vs. phase azimuth: 86-th SEG Meeting, Extended Abstracts.

Koren, Z., and I. Ravve, 2016, Fourth-order NMO velocity for P-waves in layered orthorhombic media vs. offset azimuth: 86-th SEG Meeting, Extended Abstracts.

Prevailing-frequency approximation of the coupling ray theory for S waves

Luděk Klimeš & Petr Bulant*
Department of Geophysics, Faculty of Mathematics and Physics, Charles University in Prague, Ke Karlovu 3,
121 16 Praha 2, Czech Republic, http://sw3d.cz

Summary

The coupling ray theory S-wave tensor Green function is frequency dependent. Its prevailing–frequency approximation removes this frequency dependence and allows us to introduce the coupling–ray–theory travel times and the coupling–ray–theory amplitudes, and to process the coupling–ray–theory wave field in the same way as the anisotropic–ray–theory wave field. This simplification may be decisive when storing the tensor Green function at the nodes of dense grids.

Introduction

There are two different high–frequency asymptotic ray theories for S waves with frequency–independent amplitudes: the isotropic ray theory based on the assumption of equal velocities of both S waves, and the anisotropic ray theory assuming both S waves strictly decoupled. Here the term "different" means that the isotropic ray theory is not a special case of the anisotropic ray theory for decreasing anisotropy, and that both theories yield different S waves in equal velocity models.

In the isotropic ray theory, the S–wave polarization vectors do not rotate about the ray, whereas in the anisotropic ray theory they coincide with the eigenvectors of the Christoffel matrix which may rotate rapidly about the ray.

In "weakly anisotropic" media, at moderate frequencies, the actual S–wave polarization tends to remain unrotated round the ray, but is partly attracted by the rotation of the eigenvectors of the Christoffel matrix. The intensity of the attraction increases with frequency. This behaviour of the actual S–wave polarization is described by the coupling ray theory proposed by Coates & Chapman (1990). The frequency–dependent coupling ray theory is the generalization of both the zero–order isotropic and anisotropic ray theories and provides continuous transition between them. The coupling ray theory is applicable to S waves at all degrees of anisotropy, from isotropic to considerably anisotropic velocity models. The numerical algorithm for calculating the frequency–dependent coupling–ray–theory S–wave Green tensor has been designed by Bulant & Klimeš (2002).

The coupling–ray–theory S–wave Green tensor is frequency dependent, and is usually calculated for many frequencies. This frequency dependence represents no problem in calculating the Green tensor, but may represent a great problem in storing the Green tensor at the nodes of dense grids (Klimeš & Bulant, 2013), typical for applications such as seismic migrations, Born approximation, or hypocenter determination. This contribution is devoted to the approximation of the coupling–ray–theory Green tensor, which eliminates this frequency dependence within a limited frequency band.

Theory and Method

In the vicinity of a given prevailing frequency, we approximate the frequency–dependent frequency–domain coupling–ray–theory tensor Green function (G^{CRT}) by two dyadic Green functions corresponding to two waves described by their travel times and amplitudes calculated for the prevailing frequency. We refer to these travel times and amplitudes as the coupling–ray–theory travel times and the coupling–ray–theory amplitudes. This prevailing–frequency approximation of the coupling ray theory tensor Green function (G^{PFA}) is uniquely defined by two conditions:

a) at the given prevailing frequency, we require $G^{PFA}=G^{CRT}$ and

b) at the given prevailing frequency, we require the derivative of G^{PFA} with respect to the frequency to equal the derivative of G^{CRT}.

These two conditions uniquely determine coupling-ray-theory travel times and coupling-ray-theory polarization vectors. We numerically calculate G^{CRT} at the given prevailing frequency using the algorithm by Bulant & Klimeš (2002), and we calculate the derivatives of G^{CRT} with respect to the frequency using the derivative of this algorithm (Klimeš & Bulant 2016). The prevailing–frequency approximation of the coupling ray theory allows us to process the coupling–ray–theory wave field in the same way as the anisotropic–ray–theory wave field. This simplification may be decisive when storing the tensor Green function at the nodes of dense grids.

The coupling ray theory is usually applied to anisotropic common reference rays, but it is more accurate if it is applied to reference rays which are closer to the actual wave paths. In a generally anisotropic medium, the actual wave paths may be approximated by the anisotropic–ray–theory rays if these rays behave reasonably. In an approximately transversely isotropic medium, we can define and trace the SH and SV reference rays, and use them as reference rays for the prevailing–frequency approximation of the coupling ray theory (Klimeš & Bulant 2015).
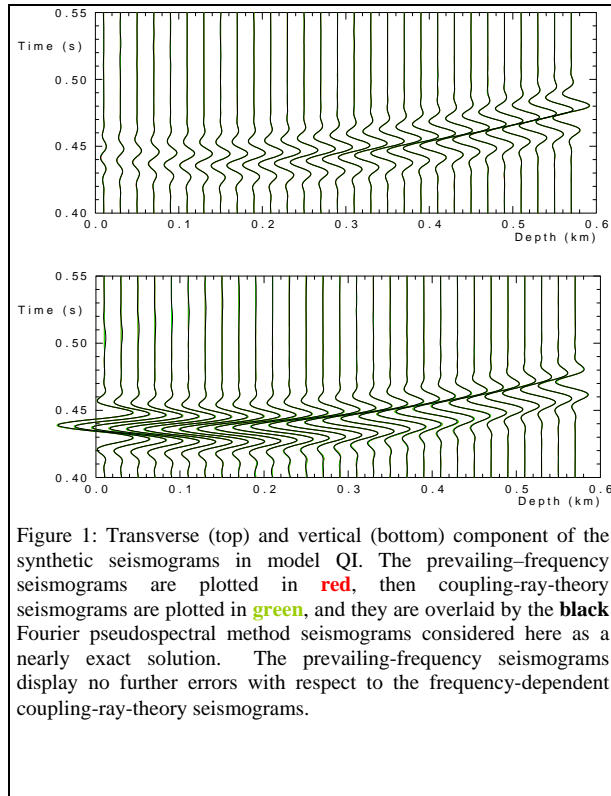
Figure 1: Transverse (top) and vertical (bottom) component of the synthetic seismograms in model QI. The prevailing–frequency seismograms are plotted in **red**, then coupling-ray-theory seismograms are plotted in **green**, and they are overlaid by the **black** Fourier pseudospectral method seismograms considered here as a nearly exact solution. The prevailing-frequency seismograms display no further errors with respect to the frequency-dependent coupling-ray-theory seismograms.


Figure 2: Vertical components of the synthetic seismograms in model SC2. Top figure shows the coupling-ray-theory seismograms calculated along the common anisotropic reference rays plotted in **red**, and they are overlaid by the **black** Fourier pseudospectral method seismograms considered here as a nearly exact solution. The bottom figure shows the coupling-ray-theory seismograms calculated along the approximate SH and SV anisotropic reference rays plotted in **red**, and they are again overlaid by the **black** Fourier pseudospectral method seismograms. The seismograms calculated along the approximate SH and SV rays display better fit with the Fourier pseudospectral method seismograms.

Examples & Conclusions

We tested the accuracy of the proposed prevailing–frequency approximation of the coupling ray theory numerically using elastic S waves in several anisotropic velocity models. The additional inaccuracy introduced by the prevailing–frequency approximation is smaller than the inaccuracy of the standard frequency–domain coupling ray theory, see the example of synthetic seismograms in model QI on Figure 1.

We used SH and SV reference rays in several models which are approximately transversely isotropic, and obtained more accurate synthetic seismograms compared to the case of using the common anisotropic reference rays, see the example of synthetic seismograms in model SC2 on Figure 2.

Acknowledgments

References

Bulant, P. & Klimeš, L. (2002): Numerical algorithm of the coupling ray theory in weakly anisotropic media. *Pure appl. Geophys.*, **159**, 1419–1435.

Coates, R.T. & Chapman, C.H. (1990): Quasi–shear wave coupling in weakly anisotropic 3–D media. *Geophys. J. int.*, **103**, 301–320.

Klimeš, L. & Bulant, P. (2012): Single–frequency approximation of the coupling ray theory. *Seismic Waves in Complex 3–D Structures*, **22**, 143–167, online at "http://sw3d.cz".

Klimeš, L. & Bulant, P. (2013): Interpolation of the coupling–ray–theory S–wave Green tensor within ray cells. *Seismic Waves in Complex 3–D Structures*, **23**, 203–218, online at "http://sw3d.cz".

Klimeš, L. & Bulant, P. (2015): Ray tracing and geodesic deviation of the SH and SV reference rays in a heterogeneous generally anisotropic medium which is approximately transversely isotropic. *Seismic Waves in Complex 3–D Structures*, **25,** 187–208, online at "http://sw3d.cz".

Klimeš, L. & Bulant, P. (2016): Prevailing-frequency approximation of the coupling ray theory for electromagnetic waves or elastic S waves. *Stud. Geophys. Geod.*, **60**, 419–450, DOI: 10.1007/s11200-014-1070-4

Theory of interval traveltime parameter estimation in layered anisotropic media

Yanadet Sripanich and Sergey Fomel, The University of Texas at Austin

SUMMARY

Moveout approximations for reflection traveltimes are typically based on a truncated Taylor expansion of traveltime squared around zero offset. The fourth-order Taylor expansion involves NMO velocities and quartic coefficients. We derive general expressions for layer-stripping of both second- and fourth-order parameters in horizontally stacked anisotropic strata. The error of approximating effective parameters by using approximate VTI formulas can be significant in comparison with the exact formulas derived in this paper. The proposed Dix-type inversion formulas for interval parameter estimation from traveltime expansion coefficients and the averaging formulas for calculation of effective parameters are readily applicable to 3D seismic reflection processing in layered media with arbitrary anisotropy.

TRAVELTIME EXPANSION

Bolshykh (1956) and Taner and Koehler (1969) laid the groundwork for studies on moveout approximations by proposing to employ the Taylor expansion of reflection traveltimes around zero offset. In the case of horizontally stacked isotropic layers, the effective NMO velocity can be related to the interval velocity through Dix inversion (Dix, 1955). Its 3D counterpart was described as *generalized Dix equation* (Grechka and Tsvankin, 1998). In the case of long-offset seismic data and more complex media, the moveout nonhyperbolicity must be considered (Fomel and Grechka, 2001). An averaging formula for the effective quartic coefficient in VTI media and its corresponding Dix-type formula for interval quartic coefficient estimation were studied by Hake et al. (1984) and Tsvankin and Thomsen (1994). Several other nonhyperbolic moveout approximations have been investigated and can be related to the generalized moveout approximation (Fomel and Stovas, 2010; Sripanich and Fomel, 2015; Sripanich et al., 2016).

In the case of 3D orthorhombic media, several well-known moveout approximations make use of the rational approximation (Al-Dajani et al., 1998), together with, the weak anisotropy assumption (Pech and Tsvankin, 2004; Xu et al., 2005; Vasconcelos and Tsvankin, 2006). For a horizontally layered model, this approximation suggests averaging azimuthally dependent interval quartic coefficients using the formula for VTI media, which is justifiable only when the azimuthal anisotropy is mild (Al-Dajani et al., 1998; Vasconcelos and Tsvankin, 2006). In this paper, we propose a framework for deriving exact expressions for averaging interval traveltime coefficients and also exact Dix-like layer-stripping formulas for interval parameter estimation in 3D layered media with arbitrary anisotropy.

Assuming the Einstein repeated-indices summation convention, we can expand the squared two-way traveltime into a Taylor series of full offset $x_i = 2h_i$ ($i = 1$ or 2 in 3D) around zero offset as follows:

$$4t^2(x_i) \approx 4t_0^2 + a_{ij}x_ix_j + a_{ijkl}x_ix_jx_kx_l + \dots , \qquad (1)$$

where

$$a_{ij} = t_0t_{ij} , \qquad (2)$$

$$a_{ijkl} = \frac{1}{16}\left(t_{ij}t_{kl} + \frac{t_0}{3}t_{ijkl}\right) . \qquad (3)$$

Here, t denotes one-way traveltime, t_0 is t along the vertical axis, h_i denotes half offset, $t_{ij} = \frac{\partial^2 t}{\partial h_i \partial h_j}$ and $t_{ijkl} = \frac{\partial^4 t}{\partial h_i \partial h_j \partial h_k \partial h_l}$ are second- and fourth-order derivative tensors, respectively. Both tensors are symmetric thanks to the symmetry of mixed derivatives. Equation 1 is valid when pure-mode reflections with source-receiver reciprocity are considered.

In the case of horizontally stacked layers, the half-offset and two-way traveltime can be expressed in terms of horizontal slownesses p_1 and p_2 in h_1 and h_2 directions as follows:

$$h_i(p_1, p_2) = -\sum_{n=1}^{N}D_{(n)}\frac{\partial Q_{(n)}(p_1, p_2)}{\partial p_i} , \qquad (4)$$

$$2t(p_1, p_2) = 2\left(p_1h_1 + p_2h_2 + \sum_{n=1}^{N}D_{(n)}Q_{(n)}(p_1, p_2)\right) ,$$

where $D_{(n)}$ and $Q_{(n)}(p_1, p_2)$ denote the thickness and the vertical slowness of the n-th layer. The general dependence $Q_{(n)}(p_1, p_2)$ follows directly from the Christoffel equation. Throughout the text, we use the subscript index (n) to indicate the corresponding layer. The upper-case and lower-case letters denote interval and effective parameters respectively.

INTERVAL PARAMETER ESTIMATION

Using equation 4 and applying the chain rule, we can differentiate the one-way traveltime t with respect to half offset h_i to derive the following expressions at zero offset ($p_i=0$):

$$t_i|_{h=0} = 0 , \qquad (5)$$

$$t_{ij}|_{h=0} = g_{ij} , \qquad (6)$$

$$t_{ijk}|_{h=0} = 0 , \qquad (7)$$

$$t_{ijkl}|_{h=0} = -g_{\hat{l}l}g_{\hat{k}k}g_{im}h_{m\hat{m},\hat{k}\hat{l}}g_{\hat{m}j} , \qquad (8)$$

where the derivatives with respect to p_1 and p_2 are represented by comma ($\frac{\partial}{\partial p_i}$ corresponds to $,i$), g_{ij} denotes $\frac{\partial p_i}{\partial h_j}$, and $\hat{k}$, $\hat{l}$, $\hat{m}$ represent dummy indices. Equations 5-8 can be substituted into equations 2 and 3 leading to

$$a_{ij} = t_0g_{ij} , \qquad (9)$$

$$a_{ijkl} = \frac{1}{16}\left(g_{ij}g_{kl} - \frac{t_0}{3}g_{\hat{l}l}g_{\hat{k}k}g_{im}h_{m\hat{m},\hat{k}\hat{l}}g_{\hat{m}j}\right) . \quad (10)$$

Equations 9 and 10 represent the most general forms of the traveltime derivatives for pure-mode reflections in horizontally layered media with arbitrary anisotropy.

Interval parameter estimation

Letting elements of the matrix inverse of a_{ij} be denoted as b_{ji} and considering the second-order term (equation 9) with direct accumulations of traveltime and offset, we can deduce

$$B_{ji(n)} = \frac{t_{0(n)}b_{ji(n)} - t_{0(n-1)}b_{ji(n-1)}}{t_{0(n)} - t_{0(n-1)}} . \qquad (11)$$

where $T_{0(n)} = t_{0(n)} - t_{0(n-1)}$ and $B_{ji(n)}$ denote the vertical one-way traveltime and the inverse of interval matrix $A_{ij(n)}$ in the n-th layer, and $t_{0(n)}$ and $b_{ji(n)}$ denote the effective values of the same two parameters at the bottom of the n-th layer. Equation 11 is referred to as the *generalized Dix equation* (Tsvankin and Grechka, 2011). We can turn to equation 10 for the quartic coefficients and follow an analogous procedure, where only the direct accumulation of $h_{m\hat{m},\hat{k}\hat{l}}$ term needs to be considered because other terms can be simply related to b_{ji}. Therefore, the interval quartic coefficient $A_{ijkl(n)}$ in the n-th layer can be given as follows:

$$A_{ijkl(n)} = \frac{1}{16}\left(\frac{1}{T_{0(n)}^2}A_{ij(n)}A_{kl(n)} - \right. \qquad (12)$$

$$\left. \frac{1}{3T_{0(n)}^3}A_{\hat{l}l(n)}A_{\hat{k}k(n)}A_{im(n)}H_{m\hat{m},\hat{k}\hat{l}(n)}A_{\hat{m}j(n)} \right) .$$

Thus, the second- and fourth-order interval coeffcients for the traveltime expansion can be found from equations 11 and 12 respectively.

To test the accuracy of the previously suggested approximations (Al-Dajani et al., 1998; Xu et al., 2005) for computing effective coefficients based on VTI averaging against the exact expressions, we consider two three-layered models (Sripanich and Fomel, 2016). Figure 1 shows the resultant azimuthal error plots of the quatic term $a_{ijkl}x_ix_jx_kx_l/r^4$ where $r = \sqrt{x_1^2 + x_2^2}$ denotes the offset along the CMP line. The VTI based approximation produces small errors when applied in weak anisotropic media but grow noticeably with the strength of anisotropy. The separate effects from pseudoacoustic approximation alone are shown in the same figures with large-dashed blue lines. It can be seen from the results that the error from pseudoacoustic approximation dominates the error from the VTI averaging formula in media with a higher degree of anisotropy. The total error on the quartic term $a_{ijkl}x_ix_jx_kx_l$ can be computed from the azimuthal error amplified by r^4 and grows with larger distance r along the CMP line. The proposed interval parameter estimation formulas (equations 11 and 12) are exact and produce results within computational accuracy.

Figure 1: Azimuthal relative error of the quatic term $a_{ijkl}x_ix_jx_kx_l/r^4$ where $r = \sqrt{x_1^2 + x_2^2}$ denoting the source-receiver distance along the CMP line in a) layered weak and b) layered strong model based on methods by Al-Dajani et al. (1998) (small-dashed green) and Xu et al. (2005) (Solid red). The large-dashed blue line denotes the errors solely from pseudoacoustic approximation with the correct averaging formulas. The azimuthal error shown remains constant for all offsets and can be multiplied with r^4 for the total error.

REFERENCES

Al-Dajani, A., I. Tsvankin, and M. N. Toksöz, 1998, Non-hyperbolic reflection moveout for azimuthally anisotropic media: 68th Meeting Expanded Abstracts, SEG, 1479–1482.

Bolshykh, C. F., 1956, Approximate model for the reflected wave traveltime curve in multilayered media: Applied Geophysics, **15**, 3–15. (in Russian).

Dix, C. H., 1955, Seismic velocities from surface measurements: Geophysics, **20**, 68–86.

Fomel, S., and V. Grechka, 2001, Nonhyperbolic reflection moveout of P-waves: An overview and comparison of reasons: Technical report, Colorado School of Mines.

Fomel, S., and A. Stovas, 2010, Generalized nonhyperbolic moveout approximation: Geophysics, **75**, no. 2, U9–U18.

Grechka, V., and I. Tsvankin, 1998, 3-D description of normal moveout in anisotropic inhomogeneous media: Geophysics, **63**, no. 3, 1079–1092.

Hake, H., K. Helbig, and C. S. Mesdag, 1984, Three-term Taylor series for $t^2 - x^2$ curves over layered transversely isotropic ground: Geophysical Prospecting, **32**, 828–850.

Pech, A., and I. Tsvankin, 2004, Quartic moveout coefficient for a dipping azimuthally anisotropic layer: Geophysics, **69**, no. 3, 699–707.

Sripanich, Y., and S. Fomel, 2015, 3D generalized nonhyperboloidal moveout approximation: 85th Meeting Expanded Abstracts, SEG, 5147–5152.

———, 2016, Theory of interval traveltime parameter estimation in layered anisotropic media: Geophysics. (Accepted).

Sripanich, Y., S. Fomel, A. Stovas, and Q. Hao, 2016, 3D generalized nonhyperboloidal moveout approximation: Geophysics. (Under review).

Taner, M. T., and F. Koehler, 1969, Velocity spectra – Digital computer derivation and applications of velocity functions: Geophysics, **34**, 859–881.

Tsvankin, I., and V. Grechka, 2011, Seismology of Azimuthally Anisotropic Media and Seismic Fracture Characterization: SEG.

Tsvankin, I., and L. Thomsen, 1994, Non-hyperbolic reflection moveout in anisotropic media: Geophysics, **59**, 1290–1304.

Vasconcelos, I., and I. Tsvankin, 2006, Non-hyperbolic moveout inversion of wide-azimuth P-wave data for orthorhombic media: Geophysical Prospecting, **54**, 535–552.

Xu, X., I. Tsvankin, and A. Pech, 2005, Geometrical spreading of P-waves in horizontally layered, azimuthally anisotropic media: Geophysics, **70**, D43–D53.

Travel Time Inversion within Orthorhombic Media

Ed Wright*, Shell, Peter Bakker, Shell and Xiaoxiang Wang, Shell

SUMMARY

With wide-azimuth and full-azimuth surveys becoming more common within the industry, so too is it becoming more common to observe residual moveout (RMO) that is dependent on the azimuthal angle. This abstract demonstrates how orthorhombic parameters can be tomographically inverted for from RMO that exhibits azimuthal dependency. The method uses a two-step approach, where the azimuthal direction of anisotropy is first realized, and then subsequent orthorhombic parameters can be inverted for. The method has been tested on simple synthetic examples, and real data examples (not shown in this abstract).

INTRODUCTION

An orthorhombic medium is described by having three mutually orthogonal planes of mirror symmetry. Figure 1 shows an example of an orthorhombic medium, where the planes of symmetry are caused by parallel vertical cracks embedded in a medium composed of thin horizontal layers. The phase velocity of a propagating wave within an orthorhombic medium depends on 12 independent parameters, where 9 of these parameters define the stiffness of the medium, and the remaining 3 define the orientation of the symmetry planes. An orthorhombic medium has a lower form of symmetry than a transversely isotropic medium.

There are a few examples in the literature where orthorhombic velocity model building has been performed. Early development into orthorhombic model building has been done by (Birdus et al., 2012). (He et al., 2013) performed orthorhombic model building in the Gulf of Mexico and (Li et al., 2012) performed velocity model building using full azimuth data for tilted orthorhombic depth imaging, also, in the Gulf of Mexico.

More recently (Kainkaryam et al., 2016) performed orthorhombic model building which included an inversion for the orientation of the prinicpal axes of azimuthal anisotropy. This was done by determining the major axis of the elliptical variation in δ.

In this abstract we present a two step method to performing orthorhombic model building. The first step uses an elliptical approximation of the phase velocity, given by equation 1, to determine the orientation of the principal axes of azimuthally dependent anisotropy. The second step freezes this orientation, and then performs another inversion for the remaining orthorhombic parameters. A simple synthetic example demonstrates this approach.

THEORY

An approximate form of the eikonal equation for an orthorhombic medium has been derived using a non-tilted weak approximation, similar to (Tsvankin, 1997), (Pšenčìk and Farra, 2005), (Farra, 2001), (Farra and Pšenčìk, 2003), given by the equation,

$$1 = V_{P0}^2 \left[\|\vec{p}\|^2 + (\epsilon_1 + \epsilon_2)A + (\epsilon_1 - \epsilon_2)B \right]$$
$$- \frac{V_{P0}^2}{\|\vec{p}\|^2} \left[(\eta_1 + \eta_2)Ap_z^2 + (\eta_1 - \eta_2)Bp_z^2 + \frac{1}{2}\eta_3 C \right], \quad (1)$$

where, $A = p_x^2 + p_y^2$, $B = (p_y^2 - p_x^2)\cos 2\chi + 2p_x p_y \sin 2\chi$, and $C = (\sin 2\chi(p_x^2 - p_y^2) + 2p_x p_y \cos 2\chi)^2$. Here, V_{P0}, is the velocity along the vertical x_3 axis in figure 1, angle χ describes the orientation of the principal axes of symmetry in the horizontal plane, $\hat{p} = (p_x, p_y, p_z)$ defines the slowness vector, ϵ_1 and ϵ_2 are Thomsen's transverse isotropy (TI) parameters (Thomsen, 1986) in the $[x_2, x_3]$, $[x_1, x_3]$, planes respectively (Tsvankin, 1997), and η_1, η_2 and η_3 are Alkhalifah's anellipticity parameters (Alkhalifah and Tsvankin, 1995) in the $[x_2, x_3]$, $[x_1, x_3]$, and $[x_1, x_2]$ planes respectively.

To determine the direction of azimuthal anisotropy, we perform a travel time inversion using an elliptic approximation of equation 1, ($\eta_1 = 0, \eta_2 = 0, \eta_3 = 0$), which determines the angle χ at which the stiffness tensor is rotated in the horizontal plane towards the principal axes of azimuthal anisotropy, and the strength of the azimuthal anisotropy. By fixing χ, another inversion is run using equation 1 to determine the remaining orthorhombic parameters. Note that tilt angles can be applied to model tilted orthorhombic media, but the tomography is restricted to the angle χ.

SYNTHETIC EXAMPLE

Synthetic data is generated by anisotropic raytracing to six horizontal reflectors from a 65 by 65 square grid of shots and receivers. The raytracing is through a constant velocity of $V_{P0} = 3500\text{ms}^{-1}$ that contains an orthorhombic ellipsoidal anomaly, where $\epsilon_1 = 0.228$, $\epsilon_2 = 0.076$, $\delta_1 = 0.02$, $\delta_2 = -0.02$, $\delta_3 = 0.02662$, $\gamma_1 = 0$, $\gamma_2 = 0$ and $\chi = 30^o$. Figure 2 (a) displays the velocity model with respect to $\delta_D = 0.5(\delta_2 - \delta_1)$. The anomaly has been removed in the start model.

The travel time inversion (TTI) input consists of double parabolic picks from offset vector tiles generated by pre-stack Kirchoff depth migration. The parameters inverted for are χ, V_{P0}, δ_1, δ_2, δ_3, ϵ_1 and ϵ_2. $\delta = 0.5(\delta_1 + \delta_2) = 0$ is a constraint in the inversion. The inversion is restricted to a box around where the anomaly

# Travel Time Inversion within Orthorhombic Media

(a)
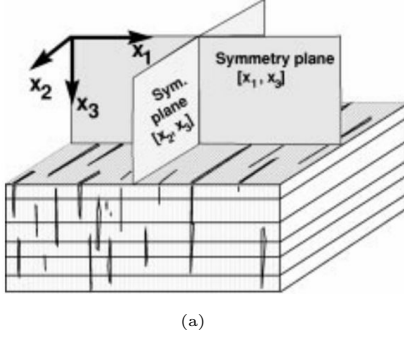
Figure 1: An orthorhombic model caused by parallel vertical cracks embedded in a medium composed of thin horizontal layers. Orthorhombic media have three mutually orthogonal planes of mirror symmetry Tsvankin (1997).

is located in the true model. The final update is obtained after 4 iterations of migration, picking and inversion.

The results in figure 2 show vertical cross-sections comparing the true (a) and final (b) profiles for δ_D, where the shape of the anomaly has been recovered. Figure 2 (c) and (d) compare depth slices showing how the inversion has recovered the principal direction and strength of the azimuthal anisotropy. This has been parameterised by $\alpha = 0.5(\epsilon_1 - \epsilon_2 + \delta_1 - \delta_2)$, where the orientation of the line segments from the x_1 axis illustrate the χ parameter. The value of α is recovered to around 80% accuracy.

In figure 2 (e) and (f) (cross-section) selections of offset vector tiles for the three deeper horizons are compared between the start model and the final model after migration. A significant reduction in the RMO is observed.

DISCUSSION

Performing an orthorhombic velocity inversion is a challenging task due to the size of the inversion parameter space. The two-step method presented here has split the problem into first determining the principal axes of azimuthal anisotropy, and then inverting for the remaining orthorhombic parameters. In the synthetic example shown, the principal strength and direction of the azimuthal anisotropy has been recovered to around 80% accuracy. A significant reduction of RMO is seen when comparing gathers generated from the start and final model, showing the validity of our approach.

ACKNOWLEDGMENTS

(a)
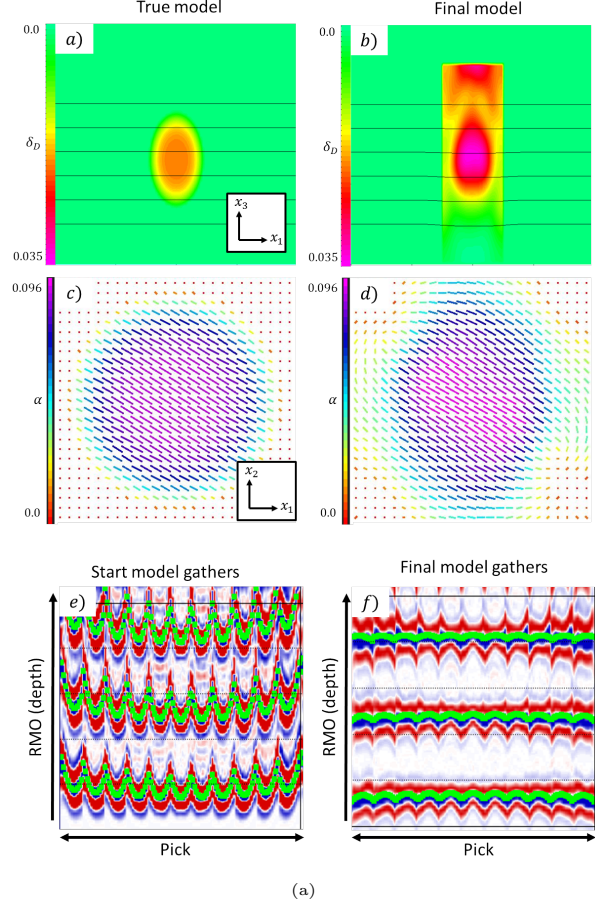
Figure 2: (a) Vertical cross-section of $\delta_D = 0.5(\delta_2 - \delta_1)$ in the true model, showing the orthorhombic anomaly. Also shown are the six horizonal reflectors. (b) Same vertical cross-section of δ_D from the final velocity model. (c) Depth cross-section of the principal direction (orientation of the line segments with the x_1 axis) and strength (length of line segment) of azimuthal anisotropy, where $\alpha = (\epsilon_1 - \epsilon_2 + \delta_1 - \delta_2)/2$. (d) Same depth cross-section for the final model. (e) Cross-section selection of offset vector tiles for three reflectors after a migration of the start model. The green squares are (cross-sections) of the double parabolic picks. (f) Same cross-section selection of offset vector tiles for the final model.

Travel Time Inversion within Orthorhombic Media

REFERENCES

Alkhalifah, T., and I. Tsvankin, 1995, Velocity analysis for transversely isotropic media: Geophysics, **60**, 1550–1566.

Birdus, S., J. Sun, W. Sun, Y. Xie, M. Gazzoli, M. Andreolli, and A. Ursulic, 2012, Multi-azimuth PSDM processing in the presence of orthorhombic anisotropy-a case history offshore North West Australia: ASEG Extended Abstracts, **2013**, 1–4.

Farra, V., 2001, High-order perturbations of the phase velocity and polarization of qP and qS waves in anisotropic media: Geophysics, **147**, 93–104.

Farra, V., and I. Pšenčìk, 2003, Properties of the zeroth-, first-, and higher-order approximations of attributes of elastic waves in weakly anisotropic media: J. Acoust. Soc. Am., **114**, 1366–1378.

He, Y., A. Gersztenkorn, G. Hilburn, S. Yang, B. Wang, et al., 2013, Orthorhombic PSDM processing a case history in Mississippi Canyon, Gulf of Mexico: 2013 SEG Annual Meeting.

Kainkaryam, S., M. Decker, D. Nichols, and J. Mathewson, 2016, Quadratic form tomography for tilted orthorhombic media: SEG Technical Program Expanded Abstracts 2015.

Li, Y., W. Han, C.-s. Chen, T. Huang, et al., 2012, Velocity model building for tilted orthorhombic depth imaging: 2012 SEG Annual Meeting.

Pšenčìk, I., and V. Farra, 2005, First-order ray tracing for qP waves in inhomogeneous weakly anisotropic media: Geophysics, **70**, D65–D75.

Thomsen, L., 1986, Weak elastic anisotropy: Geophysics, **51**, 1954–1966.

Tsvankin, I., 1997, Anisotropic parameters and P-wave velocity for orthorhombic media: Geophysics, **62**, 1292–1309.

Weak-anisotropy moveout approximations for anisotropy of arbitrary symmetry: TTI case

Ivan Pšenčík[2] and Véronique Farra[2]

[1] *Institute of Geophysics, Acad.Sci. of CR, Bočni II, 141 31 Praha 4, Czech Republic*
[2] *Institut de Physique du Globe de Paris, F-75005 Paris, France*

1   Introduction

We present an approximate P-wave moveout formula for weakly or moderately anisotropic media of arbitrary symmetry. Instead of common expansion of the square of reflection traveltime in terms of the square of the source-receiver offset, we expand the square of reflection traveltime in terms of weak-anisotropy (WA) parameters. We specify the formula for the TTI media, transversely isotropic media with arbitrarily tilted axis of symmetry, and test and discuss its accuracy.

2   Moveout formula

We consider the source-receiver profile oriented along the x_1 axis of the Cartesian coordinate system x_i. The approximate nonhyperbolic moveout formula for anisotropic media of arbitrary symmetry has then the following form:

$$T^2(\bar{x}) = T_0^2 \frac{(1+\bar{x}^2)^3}{P(\bar{x})} . \tag{1}$$

Here, T denotes the traveltime of the unconverted reflected P wave, $\bar{x}$ is the normalized offset $\bar{x} = x/2H$, where x is the source-receiver offset and H is the depth of the reflector. The symbol T_0 denotes the two-way zero-offset traveltime in a reference isotropic medium whose P-wave velocity is α, $T_0 = 2H/\alpha$. It generally represents an approximation of the actual zero-offset traveltime. Finally, the polynomial $P(\bar{x})$ in equation (1) is given by the expression

$$P(\bar{x}) = (1+\bar{x}^2)^2 + 2\epsilon_x\bar{x}^4 + 2\delta_y\bar{x}^2 + 2\epsilon_z , \tag{2}$$

in which ϵ_x, ϵ_z and δ_y are the WA parameters defined as

$$\epsilon_x = \frac{A_{11} - \alpha^2}{2\alpha^2} , \quad \epsilon_z = \frac{A_{33} - \alpha^2}{2\alpha^2} , \quad \delta_y = \frac{A_{13} + 2A_{55} - \alpha^2}{\alpha^2} . \tag{3}$$

The parameters $A_{\alpha\beta}$ are the density-normalized elastic moduli in the Voigt notation.

   Equation (1) is formally identical to the moveout formula for anisotropic media of higher symmetry up-to monoclinic, underlaid by horizontal reflectors coinciding with one of the symmetry planes (Farra, Pšenčík and Jílek, 2016). In contrast to it, equation (1) is related to a reference ray, which generally differs from the actual ray. The reference ray is symmetric with respect to the normal to the reflector and situated in the plane (x_1, x_3); its reflection point generally differs from the reflection point of the actual ray. Equation (1) is independent of the reference velocity α.

   In the following, we use the above moveout formula for TTI media. We specify the axis of symmetry of a TTI medium by the unit vector **t**:

$$\mathbf{t} \equiv (t_1, t_2, t_3) \equiv (\cos\varphi\sin\theta, \sin\varphi\sin\theta, \cos\theta) , \tag{4}$$

where φ and θ are the azimuth and polar angles, respectively. In the local Cartesian coordinate system x_i^{TI} with x_3^{TI} axis parallel to the vector **t**, P-wave propagation is controlled by three local P-wave TI WA parameters ϵ_x^{TI}, ϵ_z^{TI} and δ_y^{TI} defined as in (3), but with $A_{\alpha\beta}^{TI}$ instead of $A_{\alpha\beta}$. WA parameters ϵ_x, ϵ_z and δ_y given in equation (3) are related to WA parameters ϵ_x^{TI}, ϵ_z^{TI} and δ_y^{TI} through the following equations:

$$\epsilon_x = \epsilon_x^{TI}(t_2^2 + t_3^2)^2 + \epsilon_z^{TI}t_1^4 + \delta_y^{TI}t_1^2(t_2^2 + t_3^2) , \quad \epsilon_z = \epsilon_x^{TI}(t_1^2 + t_2^2)^2 + \epsilon_z^{TI}t_3^4 + \delta_y^{TI}t_3^2(t_1^2 + t_2^2) ,$$

$$\delta_y = 2\epsilon_x^{TI}(3t_1^2t_3^2 + t_2^2) + 6\epsilon_z^{TI}t_1^2t_3^2 + \delta_y^{TI}[(t_2^2 + t_3^2)t_3^2 + t_1^2(t_1^2 + t_2^2) - 4t_1^2t_3^2] . \tag{5}$$

3 Tests of accuracy

Figure 1 shows the relative traveltime errors of the moveout formula (1) for several orientations of the axis of symmetry of the Greenhorn shale (Fomel, 2004) model (anisotropy $\sim 26\%$). As an exact reference, traveltimes obtained from the program package ANRAY are used. The maximum errors are about 2.5%.
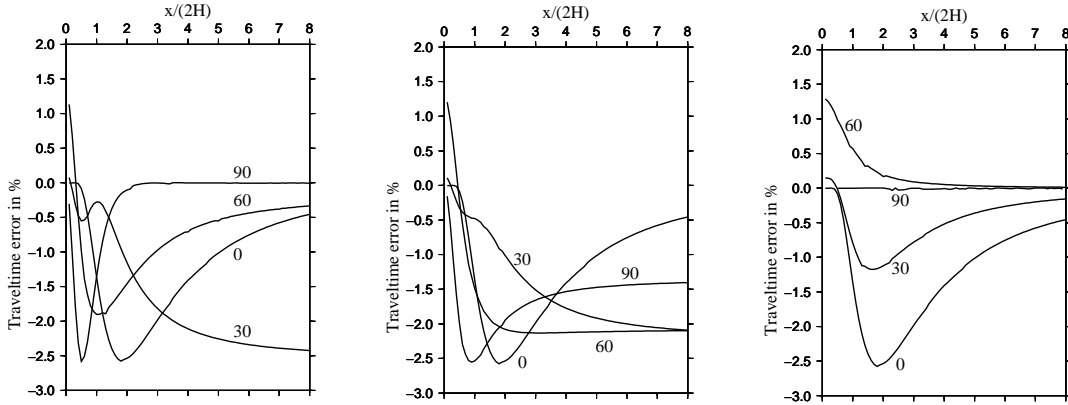

Figure 1: TTI Greenhorn shale model. Variation of relative traveltime errors with $\bar{x} = x/(2H)$ for the axis of symmetry with azimuths $\varphi = 0^o$ (left), $\varphi = 45^o$ (middle) and $\varphi = 90^o$ (right). Polar angles θ made by the axis of symmetry with the vertical x_3-axis are $\theta = 0^o$, 30°, 60° and 90° in each frame.

4 Conclusions

The approximate P-wave moveout formula (1) for anisotropic media of arbitrary symmetry represents an alternative to commonly used formulae based on the Taylor expansion of traveltime. Specified for the TTI case, it depends on two angles determining the orientation of the axis of symmetry and 3 P-wave WA parameters ϵ_x^{TI}, ϵ_z^{TI} and δ_y^{TI}.

As in previous studies, the accuracy of the formulae depends strongly on deviations of ray- and phase-velocity directions. Maximum relative traveltime errors are about 2.5% for anisotropy whose strength is about 26%.

The specification of the moveout formula (1) by only WA parameters ϵ_x, ϵ_z and δ_y (describing the VTI symmetry) agrees with the observation of Rasolofosaon (2003) that the use of the TI parameterization can be extended to moderate anisotropy of any symmetry.

For higher-symmetry anisotropic media overlaying a reflector, which coincides with one of their symmetry planes, equation (1) reduces to the formula derived recently by Farra et al. (2016) for HTI, VTI, orthorhombic or monoclinic media.

The procedure, used above for TTI media, can be used for tilted orthorhombic or monoclinic media.

Acknowledgements

References

Farra, V., Pšenčík, I. and Jílek, P., 2015. Weak-anisotropy moveout approximations for P waves in homogeneous layers of monoclinic or higher anisotropy symmetries. *Geophysics*, **81**, C39-C59.

Fomel, S., 2004. On anelliptic approximations for qP velocities in VTI media: *Geophys. Prosp.*, **52**, 247–259.

Rasolofosaon, P., 2003. Any P-wave kinematic algorithm for vertical transversely isotropic media can be ADAPTed to moderately anisotropic media of arbitrary symmetry type: *J. Appl. Geophysics*, **54**, 335–346.

Oriented inversion of non-hyperbolic moveout attributes in VTI media

M. Javad Khoshnavaz and Andrej Bóna; Curtin University, Perth, Western Australia*

Summary

Accurate seismic imaging requires an accurate velocity model. Construction of velocity model from seismic data is generally time-consuming and labor-intensive. Taking anisotropy into account, where more than a single parameter is required for searching velocities through non-hyperbolic moveout approximation, the velocity model building process would be even more time-consuming. Oriented approach is an alternative to the routine time-domain imaging/inversion algorithms (e.g., semblance analysis). The term oriented refers to velocity-less or velocity-independent techniques based on the local slopes, which carry sufficient information about the reflection geometry and the traveltime moveout of the subsurface layering/structures. We use a curvature-independent oriented approach for the inversion of non-hyperbolic moveout attributes using several non-hyperbolic approximations of traveltimes in horizontally layered vertical-transverse-isotropy (VTI) media. In the approach, the second derivative of two-way-traveltime with respect to offset (curvature) is removed from the previously proposed oriented approaches. The need for the curvature estimation is replaced by estimation of the zero-offset two-way-traveltime using predictive painting technique. The accuracy of the estimated moveout attributes using the curvature-independent approach for shifted hyperbola, rational, three-parameter and acceleration approximations is studied and compared on a synthetic VTI CMP gather.

Introduction

Most of the routine seismic imaging algorithms require a seismic velocity model. Velocity analysis from seismic data in time domain (e.g., semblance analysis and constant velocity stacks) is a popular way for velocity model building; however, it is generally labour-intensive and time-consuming (Yilmaz, 2001). It needs experienced processors to pick the proper velocities from the velocity spectrum. The velocity model building using the routine techniques (e.g., semblance analysis) becomes more complicated and time-consuming by taking non-hyperbolic traveltime moveouts into account, where more than a single parameter is required for the moveout approximations (Alkhalifah and Tsvankin, 1995).

Oriented time-domain imaging/inversion using local slopes is an alternative to the conventional imaging algorithms. Local slopes express the apparent ray parameters in a seismic record. They carry sufficient information about the reflection geometry and the traveltime moveout of the subsurface layering/structures (Fomel, 2007). A lot of research has been done in the area of the oriented time-

domain imaging over the last 80 years. Rieber (1936) and Riabinkin (1957) were the first who used local slopes in prestack seismic domain. Ottolini (1983) formulated the migration velocity for each point of the registered seismic data to perform it on his oriented migration algorithm for horizontal interfaces. This idea was generalized by Fomel (2007) by proposing several time-domain imaging operators in prestack domain. Cooke et al. (2009) further developed an oriented prestack time migration workflow. They used the oriented migration velocities to separate/ remove multiples form the primaries. These algorithms were developed for isotropic media.

Fowler et al. (2008) used local slopes for the estimation of interval velocities for anisotropic media with polar anisotropy (VTI). Oriented time-domain imaging was extended to 3D elliptically anisotropic media by Burnett and Fomel (2009a, 2009b). Casasanta and Fomel (2011) proposed another oriented time-domain imaging/inversion technique for VTI media in the slant-stack (τ-p) domain. Stovas and Fomel (2015) used local slopes and curvatures to estimate the non-hyperbolic moveout attributes in VTI media for several non-hyperbolic approximations, including shifted hyperbola approximation (Malovichko, 1978; de Bazelaire, 1988; Castle, 1994), rational approximation (Alkhalifah and Tsvankin, 1995) and generalized moveout approximation (Fomel and Stovas, 2010). Khoshnavaz et al. (2016), proposed a curvature-independent approach for the estimation of non-hyperbolic attributes in VTI media. In their approach, the attributes are in terms of local slopes and zero-offset two-way-traveltimes (TWTT) for different non-hyperbolic approximations, including shifted-hyperbola (Malovichko, 1978; de Bazelaire, 1988; Castle, 1994), rational (Alkhalifah and Tsvankin, 1995), three-parameter (Blias, 2009), and acceleration approximations (Taner et al., 2005). They took advantage of predictive painting algorithm (Fomel, 2010) for the estimation of the zero-offset TWTT. Use of predictive painting kept all moveout attributes curvature independent.

Herein, we applied the oriented technique by Khoshnavaz et al. (2016) on a synthetic multilayered VTI CMP gather. We compared the accuracy of the estimated attributes using their proposed approach for several non-hyperbolic moveout approximations, including shifted-hyperbola, rational, three-parameter, and acceleration approximation. It is shown that NMO velocity is more accurate than non-hyperbolic attribute (η), regardless of the approximation type. We found that the rational approximation has the highest accuracy while acceleration approximation has the lowest, among the other approximations presented here. We used Madagascar Open-Source package (Fomel et al., 2013) for the estimation

Oriented inversion of moveout attributes

of local event slopes using plane-wave destructors (Fomel, 2002) and for the estimation of zero-offset TWTT using predictive painting (Fomel, 2010).

Theory

The proposed approach by Khoshnavaz et al. (2016), is based on differentiation of TWTT (t) with respect to offset form the non-hyperbolic moveout approximations. It gives an oriented moveout equation in terms of local slopes (p). The original and oriented equations construct a system of equations with two unknown variables, NMO velocity and anellipticity parameter (η). Solution of the system gives the NMO velocity and the anisotropic parameter in terms of zero-offset TWTT (t_0) and the local slopes. Shifted-hyperbola, rational, three-parameter, and acceleration approximations are given by equations 1, 2, 3 and 4, respectively (Golikov and Stovas, 2012). The non-hyperbolic moveout attributes for the above approximations using the oriented approach are listed in Table 1.

$$t \cong t_0\left(1 - \frac{1}{8\eta+1}\right) + \frac{1}{8\eta+1}\sqrt{t_0{}^2 + \frac{x^2(8\eta+1)}{v^2}}, \tag{1}$$

$$t^2 \cong t_0{}^2 + \frac{x^2}{v^2} - \frac{2\eta x^4}{v^4 t_0{}^2\left[1+(1+2\eta)\frac{x^2}{v^2 t_0{}^2}\right]}, \tag{2}$$

$$t^2 \cong \frac{t_0{}^2}{2} + \frac{x^2}{v^2} + \frac{1}{2}\sqrt{t_0{}^2 - \frac{8\eta x^4}{v^4}}, \tag{3}$$

$$t^2 \cong t_0{}^2 + \frac{x^2}{v^2\left(1+\frac{2\eta x^2}{v^2 t_0{}^2}\right)}. \tag{4}$$

Shifted hyperbola	$\eta = -\frac{t_0(xp-2t+2t_0)}{8(t-t_0)(xp-t+t_0)} - \frac{1}{8}$	(5)
	$v^2 = \frac{x(xp-t+t_0)}{t_0 p(t-t_0)}$	(6)
Rational	$\eta = \frac{t_0{}^2(1+R^2)(t^2-t_0{}^2-pxt)}{2R^2(t^2-t_0{}^2)^2}$	(7)
	$v^2 = \frac{Rx^2}{t_0{}^2}$	(8)
	$R = \frac{pxtt_0{}^2}{2(t^2-t_0{}^2)^2} +$ $\frac{t_0\sqrt{(pxtt_0)^2-4(t^2-t_0{}^2)^2(t^2-t_0{}^2-pxt)}}{2(t^2-t_0{}^2)^2}$	(9)
Three-parameter	$\eta = \frac{-(2tpxc-1)(2bc-x^2)}{2x^2}$	(10)
	$v^2 = 2x^2 c$	(11)
	$b = t^2 - \frac{t_0{}^2}{2}$	(12)
	$c = \frac{2(ptx-t^2)+t_0{}^2}{4(ptbx-t^4+t^2 t_0{}^2)}$	(13)
Acceleration	$\eta = -\frac{1}{2}\frac{t_0{}^2(ptx+t_0{}^2-t^2)}{(t_0{}^2-t^2)^2}$	(14)
	$v^2 = \frac{ptx^3}{(t_0{}^2-t^2)^2}$	(15)

Table 1. Oriented moveout attributes.

Synthetic data example

The oriented inversion technique is applied to a synthetic CMP gather from a horizontally layered model including 12 VTI layers (Figure 1).
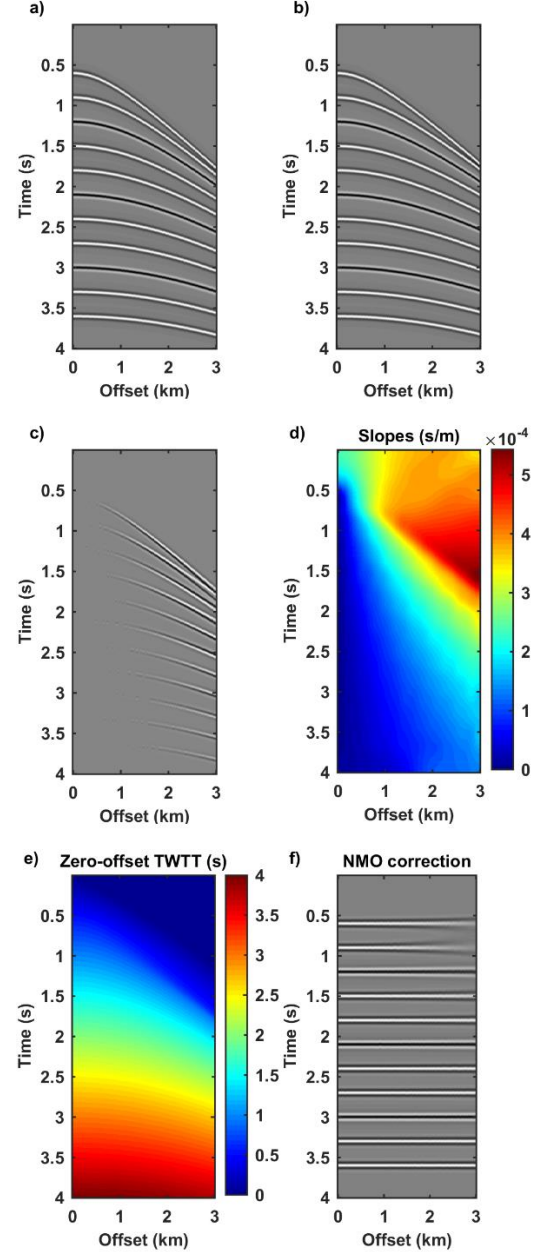

Figure 1. Generated a) isotropic and b) anisotropic CMP gather c) the amplitude difference between the isotropic and anisotropic CMP gathers, d) local slopes, e) zero-offset TWTTs, and f) flattened data.

Oriented inversion of moveout attributes

NMO-velocities increase linearly with time with the range of 1800-2300 m/s and the effective anellipticity parameter (η) varies between 0.04-0.16. Figures 1a-1c illustrate the isotropic CMP gather, anisotropic CMP gather and the difference between them, respectively. The traveltimes used for modeling, were computed from the effective VTI ray velocities corresponding to the given ηs following a similar approach explained in Bóna et al. (2008). Figures 1d-1e show the local slopes and zero-offset TWTTs estimated by plane-wave destructor (Fomel, 2002) and by predictive painting (Fomel, 2010) in Madagascar Open-Source multi-dimensional data analysis package (Fomel et al., 2013), respectively. Figure 1f illustrates the of flattened anisotropic CMP gather by the implementation of the predictive painting technique. It is observed that the anisotropic data is well flattened. To quantify the precision of the estimated TWTTs, including the zero-offset TWTTs, the exact TWTT curve at interface 5 obtained by forward modeling is compared with its corresponding predicted TWTT in Figure 3. Predicted TWTT curve is estimated using the fact that TWTTs with the same zero-offset TWTT belong to the same waveform. The procedure of predicting TWTT curves from the predicted zero-offset TWTTs is known as time-warping (Burnett and Fomel, 2009b). The standard error around the exact curve is less than 0.1% in this example.
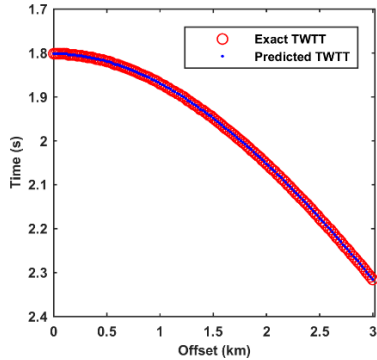

Figure 2. Comparison between the true traveltime curve and the predicted traveltime curve for interface 5 expressed Figure 1b.

The estimated local slopes and zero-offset TWTTs are employed to compute the anisotropy anellipticity coefficient (η) and NMO velocity from the presented approximations. Figures 3a-3d illustrate the corresponding estimated spectra for η from shifted hyperbola approximation (equation 5), rational approximation (equation 7), three-parameter approximation (equation 10) and acceleration approximation (equations 14), respectively. The yellow dots indicate the exact effective ηs used for forward modeling. Figures 4a-4d show the corresponding estimated spectra for NMO velocity from shifted hyperbola approximation (equation 6), rational

approximation (equation 8), three-parameter approximation (equation 11) and acceleration approximation (15), respectively. The red dots indicate the exact NMO velocities used for forward modeling. It is worth mentioning that due to the numerical errors resulting from small local slopes at small offsets (close to zero), we filter out the small-offset estimates.
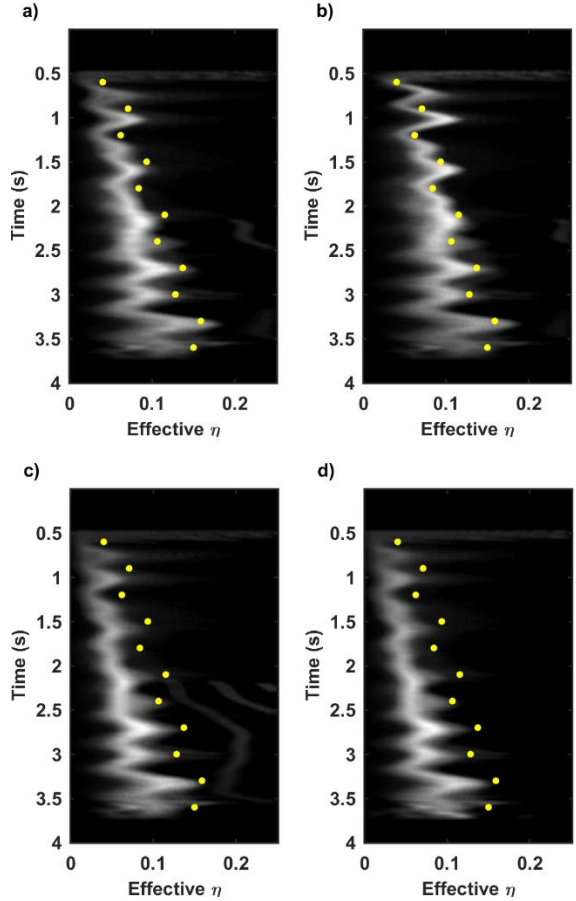
Figure 3. Estimated η from a) shifted hyperbola, b) rational, c) three-parameter and d) acceleration approximations using the oriented approach.

To have a better comparison between the accuracy of estimated moveout attributes from the approximations, we picked the maximus for the main time horizons in each spectrum and compared them with the exact values. Figures 5a and 5b show the comparison of effective ηs and effective NMO velocities obtained by the application of different approximations. It is observed that implementation of all approximations result in underestimated η and over-estimated NMO velocity. Rational approximation has the highest precision while the acceleration approximation has

Oriented inversion of moveout attributes

the lowest. The error in estimated effective η increases with time, whereas the error in NMO velocity decreases with time for all approximations. The obtained results confirm the comparable accuracy of acceleration and three-parameter approximation, as pointed out by Golikov and Stovas (2012).
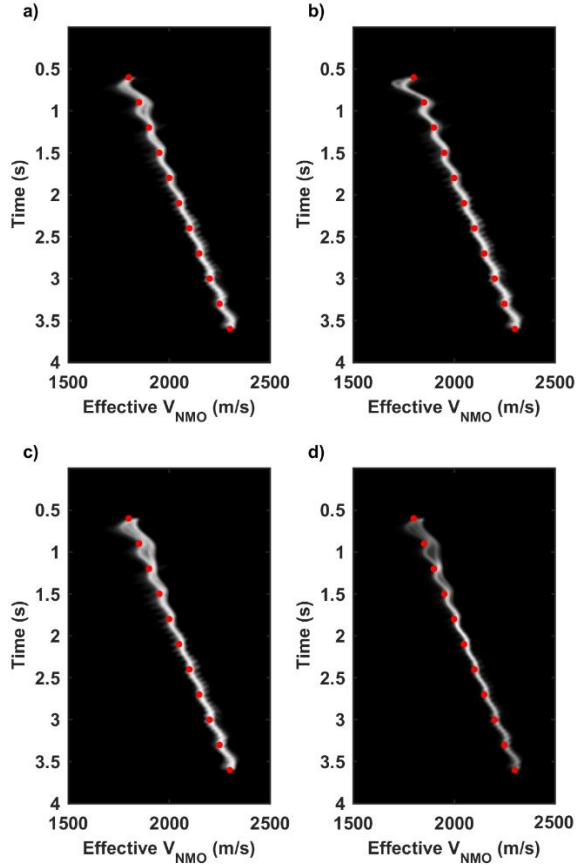

Figure 4. Estimated η from a) shifted hyperbola, b) rational, c) three-parameter and d) acceleration approximations using the oriented approach.

Conclusions

We studied an oriented approach for the inversion of non-hyperbolic attributes in VTI media. The approach is the further improved version of the previous oriented inversion algorithms. The only initial requirements of the studied approach are local slopes in each point within a CMP gather and the corresponding zero-offset TWTT. The main advantages of the oriented approach are its time-efficiency and curvature independence. The need for the estimation of curvature was replaced by the use of predictive painting technique to estimate the zero-offset TWTT. Comparison between the inverted moveout attributes obtained by the

application of the oriented approach on a numerical transversely isotropic CMP gather from shifted-hyperbola approximation, rational approximation, three-parameter approximation, and acceleration approximation showed that the rational approximation has the highest accuracy while the acceleration approximation has the lowest accuracy for both ηs and NMO velocities. It was also demonstrated that the precision in the inversion of NMO velocities is higher than the precision in the inversion of ηs, regardless of approximation type. The road ahead is to extend the oriented approach to other approximations and to estimate the interval parameters from the effective estimated parameters.

Acknowledgements
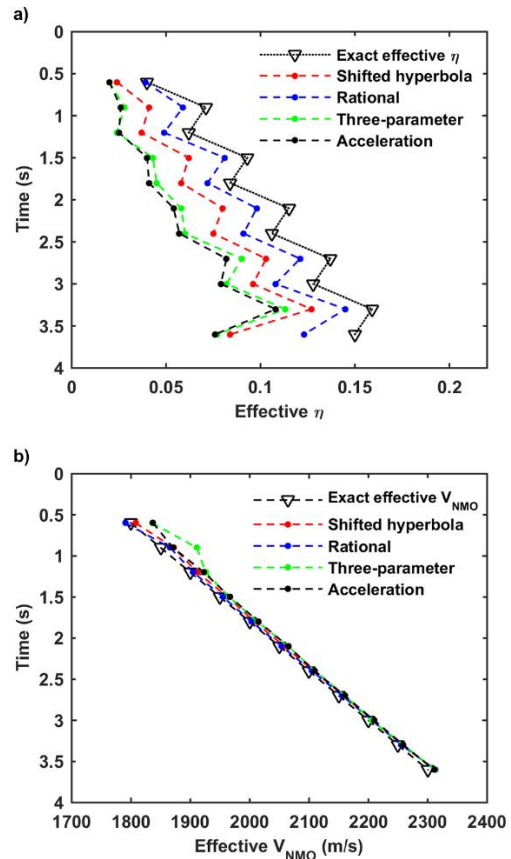
Figure 5. Comparison of a) η and b) NMO velocity for the main interfaces estimated from different approximations by the implementation of the oriented technique to the anisotropic CMP gather shown in Figure 1b.

Oriented inversion of moveout attributes

References

Alkhalifah, T., and I. Tsvankin, 1995, Velocity analysis for transversely isotropic media: Geophysics, **60**, no. 5, 1550–1566, doi: 10.1190/1.1443888.

Blias, E., 2009, Long-offset NMO approximations for a layered VTI model. Model study: 79th Annual International Meeting, SEG, Expanded Abstracts, 3745–3749, doi: 10.1190/1.3255647.

Bóna, A., I. Bucataru, and A. Slawinski, 2008, Inversion of ray velocity and polarization for elasticity tensor: Journal of applied Geophysics, **65**, 1-5, doi: 10.1016/j.jappgeo.2008.01.004.

Burnett, W., and S. Fomel, 2009a, 3D velocity-independent elliptically anisotropic moveout correction: Geophysics, **74**, no. 5, WB129–WB136, doi: 10.1190/1.3184804.

Burnett, W., and S. Fomel, 2009b, Moveout analysis by time-warping: 79th Annual International Meeting, SEG, Expanded Abstracts, **28**, 3710–3714, doi: 10.1190/1.3255639.

Casasanta, L., and S. Fomel, 2011, Velocity-independent τ-p moveout in a horizontally layered VTI medium: Geophysics, **76**, no. 4, U45-U57, doi: 10.1190/1.3595776.

Castle, R. J., 1994, Theory of normal moveout: Geophysics, **59**, no. 6, 983–999, doi: 10.1190/1.1443658.

Cooke, D., A. Bóna, and B. Hansen, 2009, Simultaneous time imaging, velocity estimation and multiple suppression using local event slopes: Geophysics, **74**, no. 6, WCA65–WCA73, doi: 10.1190/1.3242751.

de Bazelaire, E., 1988, Normal moveout revisited: Inhomogeneous media and curved interfaces: Geophysics, **53**, no. 2, 143–157, doi: 10.1190/1.1442449.

Fomel, S., 2002, Applications of plane-wave destruction filters: Geophysics, **67**, no. 6, 1946–1960, doi:10.1190/1.1527095.

———, 2007, Velocity-independent time-domain seismic imaging using local event slopes: Geophysics, **72**, no. 3, S139–S147, doi: 10.1190/1.2714047.

———, 2010, Predictive painting of 3D seismic volumes: Geophysics, **75**, no. 4, A25–A30, doi: 10.1190/1.3453847.

Fomel, S., and A. Stovas, 2010, Generalized nonhyperbolic moveout approximation: Geophysics, **75**, no. 2, U9–U18, doi: 10.1190/1.3334323.

Fomel, S., P. Sava, I. Vlad, Y. Liu, and V. Bashkardin, 2013, Madagascar: open-source software project for multidimensional data analysis and reproducible computational experiments: Journal of Open Research Software, **1**, e8, http://dx.doi.org/10.5334/jors.ag.

Fowler, P. J., A. Jackson, J. Gaffney and D. Boreham, 2008, Direct nonlinear traveltime inversion in layered VTI media: 78th Annual International Meeting, SEG, Expanded Abstracts, **27**, 3028–3032.

Golikov, P., and A. Stovas, 2012, Accuracy comparison of nonhyperbolic moveout approximations for qP-waves in VTI media: Journal of Geophysics and Engineering, **9**, 428-432, doi: 10.1088/1742-2132/9/4/428.

Khoshnavaz, M. J., A. Bóna, and M. Urosevic, 2016, Velocity-independent estimation of kinematic attributes in VTI media using local slopes and predictive painting: Accepted to publish in Geophysics.

Malovichko, A. A., 1978, A new representation of the traveltime curve of reflected waves in horizontally layered media: Applied Geophysics (in Russian), **91**, 47–53. English translation in C. H. Sword, 1987, A Soviet look at datum shift, SEP-51: Stanford Exploration Project, 313–316, accessed 26 January 2010;

http://sepwww.stanford.edu/data/media/public/oldreports/sep51/51_22.pdf.

Ottolini, R., 1983, Velocity independent seismic imaging: Technical report, Stanford Exploration Project, SEP-37: Stanford University.

Riabinkin, L. A., 1957, Fundamentals of resolving power of controlled directional reception (CDR) of seismic waves, in L. Lu, ed., Slant-stack processing, 1991, SEG, 36–60. (Translated and paraphrased from Prikladnaya Geofiizika, **16**, 3–36).

Rieber, F., 1936, A new reflection system with controlled directional sensitivity: Geophysics, **1**, 97–106, doi: 10.1190/1.1437082.

Stovas, A., and S. Fomel, 2015, Mapping of moveout attributes using local slopes: Geophysical prospecting, doi: 10.1111/1365-2478.12284.

Taner, M. T., S. Treitel, and M. Al-Chalabi, 2005, A new travel time estimation method for horizontal strata: 75th Annual International Meeting, SEG, Expanded Abstracts, 2273–2276, doi: 10.1190/1.2148170.

Yilmaz, O., 2001, Seismic data analysis, processing, inversion, and interpretation of seismic data: Investigations in Geophysics Series no. 10, SEG.

Feasibility of waveform inversion in acoustic orthorhombic media

Hui Wang [1] and Ilya Tsvankin, Colorado School of Mines

SUMMARY

3D waveform inversion (WI) for anisotropic media is highly challenging due to its computational cost, large model space, and trade-offs between the model parameters. Here, we explore the feasibility of 3D waveform inversion for orthorhombic media in the acoustic approximation. A separable form of the wave equation is implemented using the pseudospectral method. The pseudospectral extrapolator is stable and produces kinematically accurate pure-mode P-wavefields with an acceptable computational cost. To build the initial long-wavelength model for waveform inversion, we use the envelope-based misfit functional, which alleviates the reliance of WI on low-frequency data. The WI gradients are derived for both the conventional data-difference and the envelope-based objective functions. Testing on a modified SEG/EAGE overthrust model illustrates the performance of the developed wavefield-extrapolation and gradient-computation algorithms for realistic orthorhombic media.

WAVEFIELD SIMULATOR

Pure-mode mixed-domain wavefield extrapolators satisfy a general equation of the form

$$\partial_{tt} u(\mathbf{k}, t) + \mathbf{\Phi}(\mathbf{x}, \mathbf{k}) \, u(\mathbf{k}, t) = 0, \tag{1}$$

where $u(\mathbf{k}, t)$ denotes the scalar wavefield variable in the time-wavenumber domain, $\mathbf{k}$ is the wave vector, ∂_{tt} is the second time-derivative operator, and $\mathbf{\Phi}(\mathbf{x}, \mathbf{k})$ is a linear operator defined in the mixed (spatial and wavenumber) domain. For acoustic orthorhombic medium with the symmetry planes that coincide with the Cartesian coordinate planes, the separable mixed-domain operator can be derived through a Taylor series expansion (Fowler and Lapilli, 2012):

$$\mathbf{\Phi}(\mathbf{x}, \mathbf{k}) = \sum_{i=1}^{3} \left(V_{Pi}^2 \, k_i^2 - \frac{V_{P1}^2 V_{P2}^2 V_{P3}^2 / V_{Pi}^2 - V_{pai}^4}{V_r^2} \frac{k_1^2 \, k_2^2 \, k_3^2}{k_i^2 \, k^2} \right), \tag{2}$$

where V_r is a reference velocity, V_{Pi} $(i = 1, 2, 3)$ are the P-wave velocities in the coordinate directions, and

$$\begin{aligned}
V_{pa1}^2 &= V_{\text{nmo1}} \, V_{P3}, \\
V_{pa2}^2 &= V_{\text{nmo2}} \, V_{P3}, \\
V_{pa3}^2 &= V_{\text{nmo3}} \, V_{P1};
\end{aligned} \tag{3}$$

$V_{\text{nmo}i}$ $(i = 1, 2, 3)$ are the P-wave NMO velocities. The velocities V_{nmo1} and V_{nmo2} are measured in the x_1- and x_2- directions, respectively, above a horizontal orthorhombic layer. They can be expressed in Tsvankin's (1997) notation as follows:

$$V_{\text{nmo1}} \equiv V_{\text{nmo}}^{(2)} = V_{P0} \sqrt{1 + 2\delta^{(2)}}, \tag{4}$$

$$V_{\text{nmo2}} \equiv V_{\text{nmo}}^{(1)} = V_{P0} \sqrt{1 + 2\delta^{(1)}}, \tag{5}$$

where $\delta^{(1)}$ and $\delta^{(2)}$ are the anisotropy coefficients in the $[x_2, x_3]$- and $[x_1, x_3]$-planes, respectively. The velocity V_{nmo3} is defined by Fowler and Lapilli (2012) in a similar fashion:

$$V_{\text{nmo3}} \equiv V_{\text{nmo}}^{(3)} = V_{P1} \sqrt{1 + 2\delta^{(3)}}, \tag{6}$$

where $\delta^{(3)}$ corresponds to the $[x_1, x_2]$-plane (Tsvankin, 1997).

We implement the mixed-domain extrapolator using the generalized pseudospectral method. Substituting equation 2 into equation 1 and adding an exponentially decaying absorbing boundary condition yields the time-stepping formula for the generalized pseudospectral simulator:

$$
\begin{aligned}
&u(\mathbf{x}, t + \Delta t) + e^{-2\alpha(\mathbf{x})} u(\mathbf{x}, t - \Delta t) \\
&= e^{-\alpha(\mathbf{x})} \left\{ 2u(\mathbf{x}, t) - (\Delta t)^2 \sum_{i=1}^{3} \left(V_{Pi}^2 \mathcal{F}^{-1} \left[k_i^2 \mathcal{F} \left[u(\mathbf{x}, t) \right] \right] \right.\right. \\
&\left.\left. - \frac{V_{P1}^2 V_{P2}^2 V_{P3}^2 / V_{Pi}^2 - V_{pai}^4}{V_r^2} \mathcal{F}^{-1} \left[\frac{k_1^2 k_2^2 k_3^2}{k_i^2 k^2} \mathcal{F} \left[u(\mathbf{x}, t) \right] \right] \right) \right\},
\end{aligned} \tag{7}
$$

where $\alpha(\mathbf{x})$ is the damping profile.

INVERSION GRADIENTS

To compute the gradients of the objective function using the adjoint-state method (Plessix, 2006), we consider the ℓ_2-norm data difference and envelope-based misfit functionals:

$$
\begin{aligned}
\mathcal{J}_{\text{dat}} &= \frac{1}{2} \sum_{i \in \Gamma_x} \| \boldsymbol{d}_i - \boldsymbol{do}_i \|^2, \\
\mathcal{J}_{\text{env}} &= \frac{1}{2} \sum_{i \in \Gamma_x} \left\| \boldsymbol{e}_i^2 - \boldsymbol{eo}_i^2 \right\|^2,
\end{aligned} \tag{8}
$$

where the subscript i denotes the data coordinate, Γ_x is an index set for the data coordinates, $\boldsymbol{d}_i$ and $\boldsymbol{do}_i$ are the modeled and observed discrete-time data, and $\boldsymbol{e}_i$ and $\boldsymbol{eo}_i$ are the envelopes of the modeled and observed discrete data, respectively.

Misfit functionals produce different adjoint-source functions used for modeling the adjoint variables. For the ℓ_2-norm data difference and envelope-based misfit functionals, the adjoint source functions are (respectively):

$$\boldsymbol{f}_{\text{dat}}^a = \boldsymbol{d} - \boldsymbol{do}, \tag{9}$$

$$\boldsymbol{f}_{\text{env}}^a = 2 \left\{ \Delta \boldsymbol{e}^2 \circ \boldsymbol{d} - \mathbf{H} \left(\Delta \boldsymbol{e}^2 \circ \mathbf{H} \boldsymbol{d} \right) \right\}, \tag{10}$$

where $\Delta \boldsymbol{e}^2 = \boldsymbol{e}^2 - \boldsymbol{eo}^2$ is the squared envelope difference. The symbol "$\circ$" denotes the Hadamard (Schur) product and $\mathbf{H}$ is the Hilbert-transform matrix.

Parameterizing the model by V_{P1}^2, V_{P2}^2, V_{P3}^2, V_{nmo1}^2, V_{nmo2}^2, and V_{nmo3}^2, we compute the gradients for the misfit functionals

WI in acoustic orthorhombic media

through the adjoint-state formulation:

$$\frac{\partial \mathcal{J}}{\partial \left(V_{P1}^2\right)} = \left\langle \lambda, \left(k_1^2 - \frac{V_{P2}^2}{V_r^2}\frac{k_1^2 k_2^2}{k^2} - \frac{V_{P3}^2}{V_r^2}\frac{k_1^2 k_3^2}{k^2}\right) u \right\rangle, \quad (11)$$

$$\frac{\partial \mathcal{J}}{\partial \left(V_{p2}^2\right)} = \left\langle \lambda, \left(k_2^2 - \frac{V_{P1}^2}{V_r^2}\frac{k_1^2 k_2^2}{k^2} - \frac{V_{P3}^2}{V_r^2}\frac{k_2^2 k_3^2}{k^2}\right) u \right\rangle, \quad (12)$$

$$\frac{\partial \mathcal{J}}{\partial \left(V_{p3}^2\right)} = \left\langle \lambda, \left(k_3^2 - \frac{V_{P1}^2}{V_r^2}\frac{k_1^2 k_3^2}{k^2} - \frac{V_{P2}^2}{V_r^2}\frac{k_2^2 k_3^2}{k^2}\right) u \right\rangle, \quad (13)$$

$$\frac{\partial \mathcal{J}}{\partial \left(V_{\text{nmo1}}^2\right)} = \left\langle \lambda, \left(\frac{V_{P3}^2}{V_r^2}\frac{k_2^2 k_3^2}{k^2}\right) u \right\rangle, \quad (14)$$

$$\frac{\partial \mathcal{J}}{\partial \left(V_{\text{nmo2}}^2\right)} = \left\langle \lambda, \left(\frac{V_{P3}^2}{V_r^2}\frac{k_1^2 k_3^2}{k^2}\right) u \right\rangle, \quad (15)$$

$$\frac{\partial \mathcal{J}}{\partial \left(V_{\text{nmo3}}^2\right)} = \left\langle \lambda, \left(\frac{V_{P1}^2}{V_r^2}\frac{k_1^2 k_2^2}{k^2}\right) u \right\rangle, \quad (16)$$

where λ is the adjoint wavefield variable satisfying the discrete adjoint equations and $\langle \cdot, \cdot \rangle$ denotes the inner product in the L_2-space (to which the state and adjoint variables belong).

NUMERICAL EXAMPLE
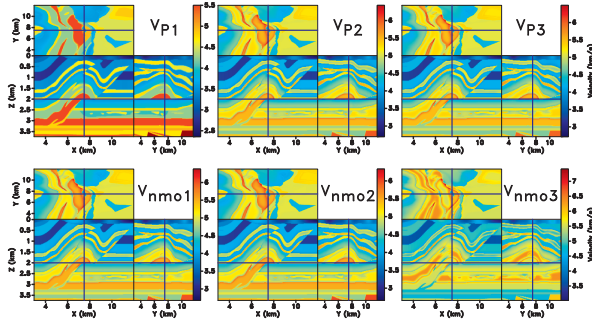
Figure 1: Orthorhombic medium obtained from the SEG/EAGE overthrust model. The velocities are scaled from the original P-wave isotropic velocity field.

The algorithm is tested on a modified 3D SEG/EAGE overthrust model. The medium parameters are obtained by heuristically scaling the P-wave velocity to ensure that each parameter varies within a reasonable range (Figure 1). The initial models for all velocities linearly increase with depth and contain little structural information (Figure 2). For comparison, we apply both misfit functionals to compute the WI gradients. The data are generated for 25 shots (red dots) in Figure 2 at every grid point on the horizontal surface. Figure 3 displays the gradients obtained using the data-difference misfit functional. The gradients have substantial values only in the shallow part of the model because the initial velocity fields are quite smooth and most of the modeled energy represents diving waves. The gradients computed with the data-difference functional contain higher-wavenumber information, which should generally be avoided during the early stages of WI. In contrast, the gradients
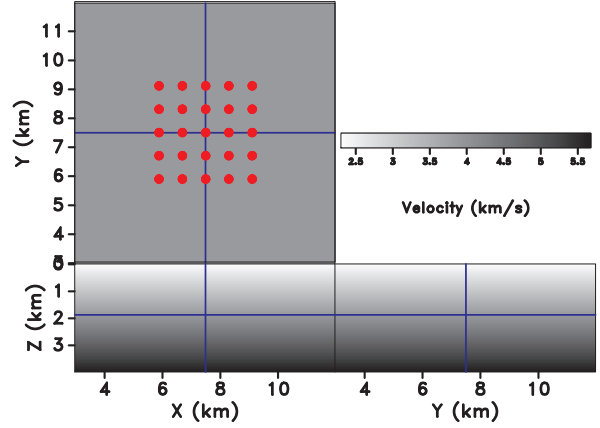
Figure 2: Initial parameter fields (identical for all six parameters) used to compute the WI gradients for the model in Figure 1. The red dots mark the source positions.

produced by the squared envelope misfit functional are more smooth and have a lower-wavenumber content, which should help in updating long-wavelength macro models for later iterations of WI.
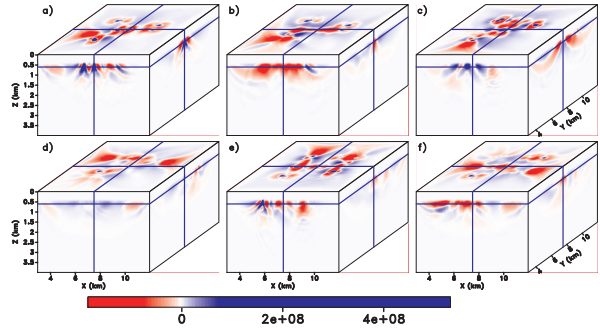
Figure 3: Gradients computed with the data difference functional: a) V_{P1}^2, b) V_{P2}^2, c) V_{P3}^2, d) V_{nmo1}^2, e) V_{nmo2}^2, and f) V_{nmo3}^2.

REFERENCES

Fowler, P. J., and C. Lapilli, 2012, Generalized pseudospectral methods for orthorhombic modeling and reverse-time migration: 82nd Annual International Meeting, SEG, Expanded Abstracts, 1–5.

Plessix, R.-E., 2006, A review of the adjoint-state method for computing the gradient of a functional with geophysical applications: Geophysical Journal International, **167**, 495–503.

Tsvankin, I., 1997, Anisotropic parameters and P-wave velocity for orthorhombic media: Geophysics, **62**, 1292–1309.

Elastic FWI for VTI media: A synthetic parameterization study

Nishant Kamath, Ilya Tsvankin & Esteban Díaz
Center for Wave Phenomena, Colorado School of Mines

SUMMARY

A major challenge for multiparameter full-waveform inversion (FWI) is the inherent trade-offs (or cross-talk) between model parameters. Here, we perform elastic FWI of multicomponent data generated for a synthetic VTI (transversely isotropic with a vertical symmetry axis) model based on a geologic section of the Valhall field in the North Sea. An oblique displacement source, which excites intensive SV waves in the conventional offset range, is needed to take advantage of shear information. We test three model parameterizations, which exhibit different radiation patterns and, therefore, create different parameter trade-offs. The results show that the choice of parameterization for FWI depends on the availability of long-offset data, the quality of the initial model for the anisotropy coefficients, and the parameter that needs to be resolved with the highest accuracy.

INTRODUCTION

Full-waveform inversion (FWI) can provide a higher-resolution model of the subsurface (on the order of wavelength) compared to reflection or traveltime tomography. Most elastic FWI algorithms are developed for isotropic media (Vigh et al., 2014). When anisotropy is taken into account, inversion is often performed in the acoustic approximation (Gholami et al., 2013; Alkhalifah and Plessix, 2014).

Kamath and Tsvankin (2016) devise an elastic FWI algorithm for VTI media and apply it to 2D synthetic transmission data. To gain insight into the inversion results, they present analytic expressions for the radiation (sensitivity) patterns of the VTI parameters. Here, the FWI methodology of Kamath and Tsvankin (2016) is applied to multicomponent data from a synthetic model based on a geologic section of the Valhall field.

METHODOLOGY

FWI is performed in the time domain by minimizing the least-squares objective function $\mathscr{F}$ defined as the L2-norm of the difference between the observed data and those computed for a trial model. The gradient of the objective function with respect to the stiffness coefficients c_{ijkl} is obtained using the adjoint-state method (Kamath and Tsvankin, 2016):

$$\frac{\partial \mathscr{F}}{\partial c_{ijkl}} = -\int_0^T \frac{\partial u_i}{\partial x_j} \frac{\partial \psi_k}{\partial x_l} \, dt \,, \qquad (1)$$

where T is the trace length, and $\mathbf{u}$ and ψ are the forward-modeled and adjoint wavefields, respectively. The gradient with respect to a chosen model parameter m_n is then found

as:

$$\frac{\partial \mathscr{F}}{\partial m_n} = \sum_{ijkl} \frac{\partial \mathscr{F}}{\partial c_{ijkl}} \frac{\partial c_{ijkl}}{\partial m_n}. \qquad (2)$$

A finite-difference algorithm is employed to compute the multicomponent displacement field using the elastic wave equation for VTI media. The model is iteratively updated with the L-BFGS-B technique of Byrd et al. (1995).

Propagation of P- and SV-waves in VTI media is controlled by four Thomsen parameters: the P- and SV-wave vertical velocities, V_{P0} and V_{S0}, and the anisotropy coefficients ε and δ. The parameterizations employed here include combinations of V_{P0}, V_{S0}, the P-wave NMO (V_{nmo}) and horizontal (V_{hor}) velocities, and the anisotropy coefficients ε, δ, and η.

INVERSION RESULTS

The synthetic model (Figure 1) used in this paper is fashioned after the geology of the Valhall field in the North Sea (Munns, 1985). The initial models for all three parameterizations are computed by smoothing the actual fields of V_{P0}, V_{S0}, V_{nmo}, and V_{hor}. We use 109 displacement sources placed with an increment of 80 m, and receivers at every grid point; both sources and receivers are at a depth of 20 m. The source signal is a Ricker wavelet with a peak frequency of 3.5 Hz. A multiscale approach is employed to mitigate cycle-skipping; the resolution of the inverted model, as expected, increases with the addition of higher frequencies.

The first parameterization, which was successfully used by Kamath and Tsvankin (2013) for layer-cake VTI media, includes the velocities V_{P0}, V_{S0}, V_{nmo} and V_{hor}. The P-wave radiation patterns of V_{P0} and V_{hor} (Figure 2(a)) do not significantly overlap, and the objective function is most sensitive to these two velocities. A high-resolution V_{P0}-field (Figure 3(a)) can be obtained even with conventional-offset data if the initial model does not produce cycle-skipping. To build an accurate low-wavenumber model of V_{hor} (Figure 3(a)), it is necessary to use diving waves.

The objective function for the second parameterization, which consists of V_{nmo}^2, V_{S0}^2, $(1+2\eta)$, and $(1+2\delta)$ (after Alkhalifah and Plessix, 2014), is more sensitive to the velocity V_{nmo} than to the other parameters. Because of the trade-off between V_{nmo} and the anisotropy coefficient η at large offsets, the long-wavelength model of V_{nmo} cannot be built without good a priori knowledge of η. The possibility of obtaining a high-resolution V_{nmo}-field from data in the conventional offset range depends on the accuracy of the initial δ-field.

A low-wavenumber model of the horizontal velocity for parameterization III [V_{hor}^2, V_{S0}^2, $(1+2\eta)$, and $(1+2\varepsilon)$] can be accurately estimated by inverting long-offset data because there

Elastic FWI for 2D VTI media
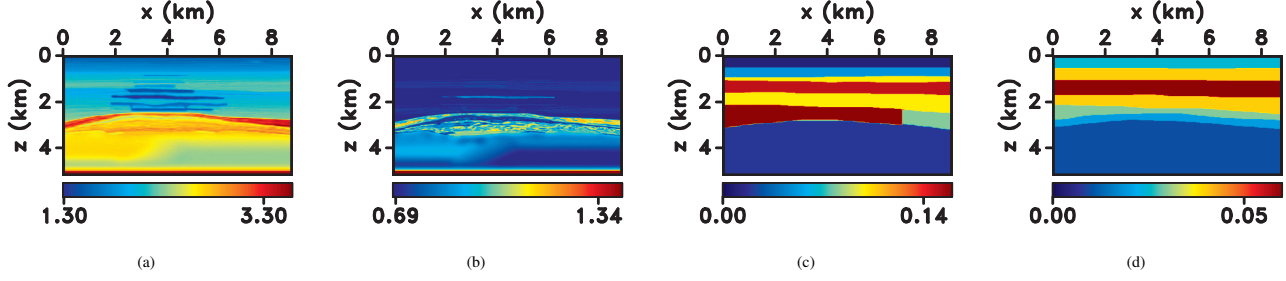
Figure 1: Parameters (a) V_{P0}, (b) V_{S0}, (c) ε, and (d) δ of a synthetic VTI model based on sections from the Valhall field. The velocities have units of km/s.
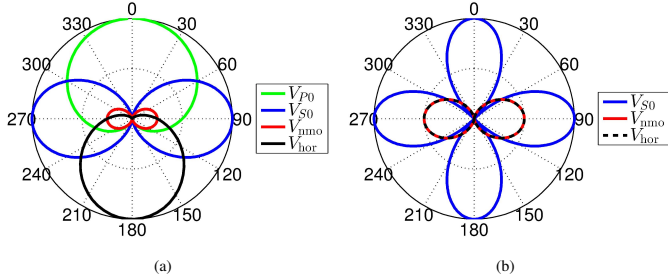

Figure 2: (a) P- and (b) SV-wave radiation patterns obtained with parameterization I for reflections from a horizontal interface. The patterns are computed as functions of the opening angles at the diffractor with the background velocity ratio $V_P/V_S = 2$ (the background is isotropic).
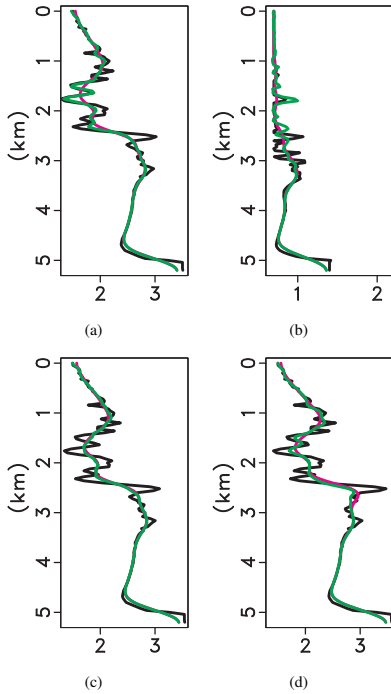

Figure 3: Actual (black), initial (magenta), and inverted (green) velocities for parameterization I: (a) V_{P0}, (b) V_{S0}, (c) V_{nmo}, and (d) V_{hor}. The data were generated by an array of oblique displacement sources. The profiles are displayed at location x = 3.5 km.

are no trade-offs between V_{hor} and other parameters at large opening angles. Conventional-offset displacement can yield a high-resolution model of V_{hor} provided the ε-field is known with sufficient accuracy.

The results for this synthetic model provide important insights into the performance of elastic FWI for VTI media and should help in choosing the most suitable parameterization for different inversion scenarios.

ACKNOWLEDGMENTS

REFERENCES

Alkhalifah, T., and R. Plessix, 2014, A recipe for practical full-waveform inversion in anisotropic media: An analytical parameter resolution study: Geophysics, **79**, R91–R101.

Byrd, R. H., P. Lu, J. Nocedal, and C. Zhu, 1995, A limited memory algorithm for bound constrained optimization: SIAM Journal on Scientific Computing, **16**, 1190–1208.

Gholami, Y., R. Brossier, S. Operto, A. Ribodetti, and J. Virieux, 2013, Which parameterization is suitable for acoustic vertical transverse isotropic full waveform inversion? Part 1: Sensitivity and trade-off analysis: Geophysics, **78**, R81–R105.

Kamath, N., and I. Tsvankin, 2013, Full-waveform inversion of multicomponent data for horizontally layered VTI media: Geophysics, **78**, WC113–WC121.

——, 2016, Elastic full-waveform inversion for VTI media: Methodology and sensitivity analysis: Geophysics, **81**, C53–C68.

Munns, J., 1985, The Valhall field: a geological overview: Marine and Petroleum Geology, **2**, 23–43.

Vigh, D., K. Jiao, D. Watts, and D. Sun, 2014, Elastic full-waveform inversion application using multicomponent measurements of seismic data collection: Geophysics, **79**, R63–R77.

Waveform inversion for attenuation estimation in anisotropic media

Tong Bai & Ilya Tsvankin
Center for Wave Phenomena, Colorado School of Mines

SUMMARY

Robust estimation of attenuation coefficients remains a challenging problem, especially for heterogeneous and anisotropic models. Here, we apply full-waveform inversion (FWI) for attenuation analysis in 2D VTI (transversely isotropic with a vertical symmetry axis) media. A time-domain finite-difference algorithm based on the standard linear solid model simulates nearly constant quality-factor values in a specified frequency band. We employ the adjoint-state method to derive the gradients of the objective function under the Born approximation. Four parameters describing the attenuation coefficients of P- and SV-waves are updated simultaneously with the L-BFGS technique. The inversion algorithm is tested on homogeneous VTI models with a Gaussian anomaly in one of the Thomsen-style attenuation parameters. Accurate knowledge of the velocity field and sufficient aperture of the experiment make it possible to resolve the anomaly, with better estimates of its shape and peak magnitude obtained for a lower-frequency source wavelet.

VISCOELASTIC MODELING IN VTI MEDIA

Wavefields in attenuative media can be simulated in the time domain by superposing several rheological bodies (Carcione, 1993; Bohlen, 2002). As discussed by Bai and Tsvankin (2016), anisotropic attenuation can be described by the following relaxation function (shown here with only one relaxation mechanism):

$$\Psi_{ijkl}(t) = C_{ijkl}^R \left(1 + \tau_{ijkl}\, e^{-t/\tau^\sigma} \right) H(t), \qquad (1)$$

where $C_{ijkl}^R = \Psi_{ijkl}(t \to \infty)$ is called the "relaxed stiffness," which corresponds to the low-frequency limit ($\omega = 0$), τ^σ denotes the stress relaxation time determined by the dominant frequency, the τ_{ijkl}-parameters measure the difference between the stress and strain relaxation time and quantify the magnitude of anisotropic attenuation, and $H(t)$ is the Heaviside function. The relaxation function at zero time yields the "unrelaxed stiffness":

$$C_{ijkl}^U \equiv \Psi_{ijkl}(t=0) = C_{ijkl}^R (1 + \tau_{ijkl}). \qquad (2)$$

The stiffness difference $\Delta C_{ijkl} = C_{ijkl}^U - C_{ijkl}^R$ is proportional to τ_{ijkl} and, therefore, reflects the magnitude of attenuation.

The P- and SV-wave attenuation in VTI media can be described by the Thomsen-style parameters A_{P0}, A_{S0}, ε_Q, and δ_Q (Zhu and Tsvankin, 2006); $A_{P0} \approx 1/(2Q_{33})$ and $A_{S0} \approx 1/(2Q_{55})$ denote the P- and S-wave attenuation coefficients in the vertical (symmetry-axis) direction. The parameter ε_Q quantifies the fractional difference between the horizontal and vertical P-wave attenuation coefficients, and δ_Q controls the curvature of the P-wave attenuation coefficient at the symmetry axis. Combined with the unrelaxed stiffnesses C_{ijkl}^U (used as the reference elastic parameters), these attenuation parameters can be converted into the quality-factor elements Q_{ijkl} and then into ΔC_{ijkl}.

The viscoelastic stress-strain relationship can be expressed as

$$\sigma_{ij} = C_{ijkl}^U \varepsilon_{kl} + \Delta C_{ijkl}\, r_{kl}, \qquad (3)$$

where r_{kl} are the memory variables, which satisfy the following partial differential equations (Bai and Tsvankin, 2016):

$$\frac{\partial r_{kl}}{\partial t} = -\frac{1}{\tau^\sigma}\left(r_{kl} + \varepsilon_{kl}\right). \qquad (4)$$

Equations 3 and 4 and the momentum conservation law constitute the viscoelastic VTI wave equation. Solving that equation with finite-differences allows us to carry out time-domain modeling for media with VTI symmetry for both velocity and attenuation.

VISCOELASTIC FULL-WAVEFORM INVERSION

FWI utilizes the entire waveforms of certain arrivals (e.g., diving waves and/or reflections) to iteratively update the model parameters. The degree of data fitting is usually evaluated with the ℓ_2-norm objective function (e.g., Tarantola, 1988; Tromp et al., 2005):

$$F(\mathbf{m}) = \frac{1}{2} \sum_{r=1}^{N} \parallel \mathbf{u}(x_r,t,\mathbf{m}) - \mathbf{d}(x_r,t) \parallel^2, \qquad (5)$$

where $\mathbf{u}(x_r,t,\mathbf{m})$ denotes the data computed for the trial model $\mathbf{m}$, $\mathbf{d}(x_r,t)$ is the observed data, r is the receiver index, and t is the time. Summation over shots is implied. The gradient of the objective function can be computed with the adjoint-state method (Tarantola, 1988; Tromp et al., 2005). By applying the Born approximation, the gradients for the viscoelastic parameters ΔC_{ijkl} can be expressed as the cross-correlation of the memory variables from the forward simulation with the adjoint strain fields (Tarantola, 1988):

$$\frac{\partial F}{\partial \Delta C_{jklm}} = - \sum_{\text{sources}} \int_0^T \frac{\partial u_i^\dagger}{\partial x_j}\, r_{kl}\, dt, \qquad (6)$$

where $\mathbf{u}^\dagger$ denotes the adjoint displacement field.

FWI algorithms for attenuative media are usually parameterized by coefficients inversely proportional to the quality factor Q. Here, we invert for the vertical attenuation coefficients A_{P0}, A_{S0} and two more parameters of similar magnitude (A_{Ph}, A_{Pn}) dependent on attenuation anisotropy. The P-wave horizontal attenuation coefficient A_{Ph} is given by:

$$A_{Ph} = A_{P0}(1 + \varepsilon_Q) \approx \frac{1}{2Q_{11}}. \qquad (7)$$

To account for the attenuation-anisotropy coefficient δ_Q, we define another attenuation parameter, A_{Pn}:

$$A_{Pn} = A_{P0}(1 + \delta_Q),\tag{8}$$

which governs the variation of P-wave attenuation near the symmetry axis and has a form similar to the normal-moveout (NMO) velocity for a horizontal VTI layer. The gradients for the stiffness differences ΔC_{ijkl} (equation 6) can be converted into those for the attenuation coefficients A_{P0}, A_{S0}, A_{Ph} and A_{Pn} by applying the chain rule.

To reduce the ambiguity of the inverse problem, we assume the reference velocity parameters (C_{ij}^U) and density to be known. This prevents cycle-skipping in the inversion because the influence of attenuation-induced dispersion in the seismic frequency band is typically small (Zhu and Tsvankin, 2006). Hence, the FWI algorithm can operate with relatively high frequencies to increase the sensitivity of the wavefield to attenuation. The L-BFGS method is applied to scale the gradients by an approximate inverse Hessian matrix.

SYNTHETIC EXAMPLE

The algorithm is tested on VTI models with a Gaussian anomaly in one of the Thomsen-style parameters (A_{P0}, A_{S0}, ε_Q, and δ_Q) embedded in a homogeneous background. Figure 1 shows a model with a Gaussian anomaly in the shear-wave attenuation coefficient A_{S0}. The horizontal source and receiver arrays are placed above and below the anomaly. The velocity parameters V_{P0}, V_{S0}, ε, and δ and the density are constant and kept at the actual values during the inversion. The reference frequency is set equal to the central frequency of the wavelet. Starting from the homogeneous background model, we conduct simultaneous inversion for the attenuation parameters A_{P0}, A_{S0}, A_{Ph}, and A_{Pn}. To illustrate the influence of frequency on the inversion results, the test is performed for two wavelets with a different central frequency (100 Hz and 30 Hz).
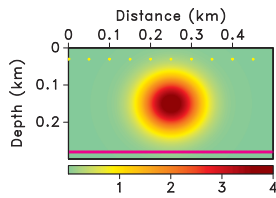

Figure 1: The fractional difference between A_{S0} and its background value, 0.005 ($Q_{S0} = 100$); at the center of the anomaly, $A_{S0} = 0.025$ ($Q_{S0} = 20$). The other parameters are constant: $A_{P0} = 0.005$, $\varepsilon_Q = 0.2$, $\delta_Q = 0.4$, $V_{P0} = 4000$ m/s, $V_{S0} = 2000$ m/s, $\varepsilon = 0.15$, $\delta = 0.1$, $\rho = 2.0\,\text{g/m}^3$. The yellow dots denote horizontal displacement sources, and the magenta line marks the receivers placed at each grid point.

When the 100-Hz wavelet is used (Figure 2(a)), the shape of the anomaly is somewhat distorted and its peak ($A_{S0} = 0.019$) deviates from the actual value ($A_{S0} = 0.025$). A more accurate recovery of the peak magnitude ($A_{S0} = 0.022$) and shape of the anomaly (Figure 2(b)) is achieved with the 30-Hz wavelet.

In both cases, the algorithm produces no updates in the other three attenuation parameters (A_{P0}, A_{Ph}, and A_{Pn}), which indicates the absence of trade-offs in the inversion for A_{S0}. Likewise, it is possible to recover the peak magnitude and shape of an anomaly in ε_Q (A_{Ph}), with better results for the low-frequency (30-Hz) wavelet.
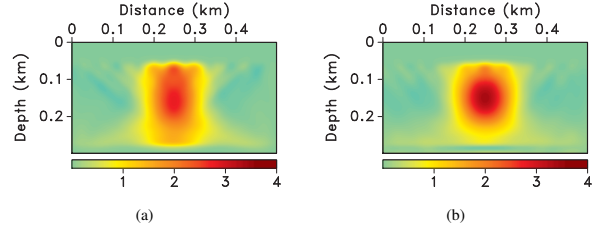

Figure 2: Fractional differences between the inverted and initial A_{S0} for the model with the A_{S0}-anomaly. The inversion is performed with the (a) 100-Hz wavelet and (b) 30-Hz wavelet.

Reconstruction of an anomaly in the P-wave coefficient A_{P0} proves to be more problematic. Because the parameters ε_Q and δ_Q are constant, there are anomalies in A_{Ph} and A_{Pn} as well. The inversion using a 100-Hz wavelet accurately recovers A_{P0}, whereas A_{Ph} and A_{Pn} are barely updated. Analysis of the objective function shows that the difficulty in estimating A_{Ph} and A_{Pn} is due to the trade-off between these two coefficients. Reducing the central frequency of the wavelet to 30 Hz improves the inversion results for A_{Ph} and A_{Pn}, although the peak values of the anomalies are underestimated.

The algorithm is also applied to a more structurally complicated medium based on a section of the modified BP TI model. These results will be discussed in the workshop presentation.

REFERENCES

Bai, T., and I. Tsvankin, 2016, Time-domain finite-difference modeling for attenuative anisotropic media: Geophysics, **81**, C69–C77.

Bohlen, T., 2002, Parallel 3-D viscoelastic finite difference seismic modelling: Computers & Geosciences, **28**, 887–899.

Carcione, J. M., 1993, Seismic modeling in viscoelastic media: Geophysics, **58**, 110–120.

Tarantola, A., 1988, Theoretical background for the inversion of seismic waveforms including elasticity and attenuation: Pure and Applied Geophysics, **128**, 365–399.

Tromp, J., C. Tape, and Q. Liu, 2005, Seismic tomography, adjoint methods, time reversal and banana-doughnut kernels: Geophysical Journal International, **160**, 195–216.

Zhu, Y., and I. Tsvankin, 2006, Plane-wave propagation in attenuative transversely isotropic media: Geophysics, **71**, no.2, T17–T30.

Anisotropic waveform inversion for microseismic velocity analysis and event location

Oscar Jarillo Michel* and Ilya Tsvankin, Center for Wave Phenomena, Colorado School of Mines

SUMMARY

Waveform inversion (WI) is extensively used in reflection seismology and could provide improved velocity models and event locations for microseismic surveys. Here, we develop an elastic WI algorithm for anisotropic media designed to estimate the 2D velocity field along with the source parameters (location, origin time, and moment tensor). The gradient of the objective function is obtained with the adjoint-state method, which requires just two modeling simulations at each iteration. The current implementation is developed for P- and SV-waves in VTI (transversely isotropic with a vertical symmetry axis media). Synthetic testing for a vertical receiver array shows that WI can accurately recover all four relevant interval VTI parameters from the horizontal and vertical displacement components, if the initial model is sufficiently accurate and the source parameters are fixed at the correct values.

INTRODUCTION

For microseismic studies, velocity models can be built simultaneously with event location using anisotropic traveltime inversion (Grechka and Yaskevich, 2014). However, WI can potentially improve the resolution of velocity analysis and accuracy of event location because it operates with entire waveforms and could include multiples, scattered waves, etc. in addition to the direct arrivals.

In a previous publication (Jarillo Michel and Tsvankin, 2014), we employ the adjoint-state method to compute the gradient of the WI objective function with respect to the microseismic source location $\mathbf{x}^s$, origin time t_0, and moment tensor $\mathbf{M}$. Jarillo Michel and Tsvankin (2015) iteratively minimize the WI objective function and estimate the source parameters from 2D multicomponent microseismic data, with the VTI velocity model assumed to be known. Here, we extend this methodology to velocity analysis of microseismic data and apply it to estimation of the interval parameters of horizontally layered VTI media.

WAVEFORM-INVERSION METHODOLOGY

The algorithm operates with the elastic wave equation for a point source in a heterogeneous anisotropic medium:

$$\rho \frac{\partial^2 u_i}{\partial t^2} - \frac{\partial}{\partial x_j}\left(c_{ijkl}\frac{\partial u_k}{\partial x_l}\right) = -M_{ij}\frac{\partial[\delta(\mathbf{x}-\mathbf{x}^s)]}{\partial x_j}S(t) , \tag{1}$$

where $\mathbf{u}(\mathbf{x}, t)$ is the displacement field, t is time, c_{ijkl} is the stiffness tensor $(i, j, k, l = 1, 2, 3)$, $\rho(\mathbf{x})$ is density, $\mathbf{M}$, $\mathbf{x}^s$, and $S(t)$ are the source moment tensor, location, and time function, respectively, and $\delta(\mathbf{x} - \mathbf{x}^s)$ is the spatial δ-function;

summation over repeated indices is implied. The finite-difference code `sfewefdm` in MADAGASCAR is used to solve equation 1 for 2D heterogeneous VTI media.

The data residuals are measured by the ℓ_2-norm objective function $\mathcal{F}$ commonly used in WI:

$$\mathcal{F}(\mathbf{m}) = \frac{1}{2}\sum_{n=1}^{N}\|\mathbf{d}_{\mathrm{pre}}(\mathbf{m}, \mathbf{x}^{r_n}) - \mathbf{d}_{\mathrm{obs}}(\mathbf{x}^{r_n})\|^2 , \tag{2}$$

where $\mathbf{d}_{\mathrm{obs}}$ is the observed displacement and $\mathbf{d}_{\mathrm{pre}}(\mathbf{m})$ is the displacement simulated for the trial model $\mathbf{m}$. The wavefield excited by each microseismic event is recorded by N receivers positioned at $\mathbf{x}^{r_n}$ $(n = 1, 2, ..., N)$; the function $\mathcal{F}$ also involves summation over all available sources.

Although the examples shown below are for 2D models, in principle this methodology is applicable to 3D data from layer-cake VTI media. Indeed, if the source-receiver azimuth can be estimated from the polarization of the direct P-wave, the in-plane horizontal displacement component employed in our algorithm can be computed by a simple receiver rotation. Then the wavefields from sources at different azimuths can be inverted simultaneously using the proposed 2D method.

Model updating

The gradient of the objective function $\mathcal{F}$ with respect to the source parameters is discussed in Jarillo Michel and Tsvankin (2014, 2015). The WI algorithm introduced here is designed to also recover the anisotropic velocity model. The gradient of the objective function $\mathcal{F}$ with respect to the stiffness coefficients c_{ijkl} can be obtained using the adjoint-state method:

$$\frac{\partial \mathcal{F}}{\partial c_{ijkl}} = -\int_0^T \frac{\partial u_i}{\partial x_j}\frac{\partial \psi_k}{\partial x_l} , \tag{3}$$

where u and ψ are the forward and adjoint displacement fields, respectively. The derivatives of $\mathcal{F}$ with respect to the chosen model parameters m_n can be found from the chain rule:

$$\frac{\partial \mathcal{F}}{\partial m_n} = \sum_{ijkl}\frac{\partial \mathcal{F}}{\partial c_{ijkl}}\frac{\partial c_{ijkl}}{\partial m_n} . \tag{4}$$

The gradient for the source and velocity parameters can be computed from the same forward and adjoint wavefields generated by two finite-difference simulations. In the example below, the source parameters are fixed, which helps avoid parameter trade-offs. However, the algorithm is designed to perform sequential inversion where the source parameters are obtained first using the initial velocity model. Then the inverted source parameters are employed to update the velocity model, and the process continues in iterative fashion. The model is updated with the l−BFGS method (Byrd et al., 1995).

Signatures of P- and SV-waves in VTI media are described by

Anisotropic waveform inversion for microseismic velocity analysis and event location
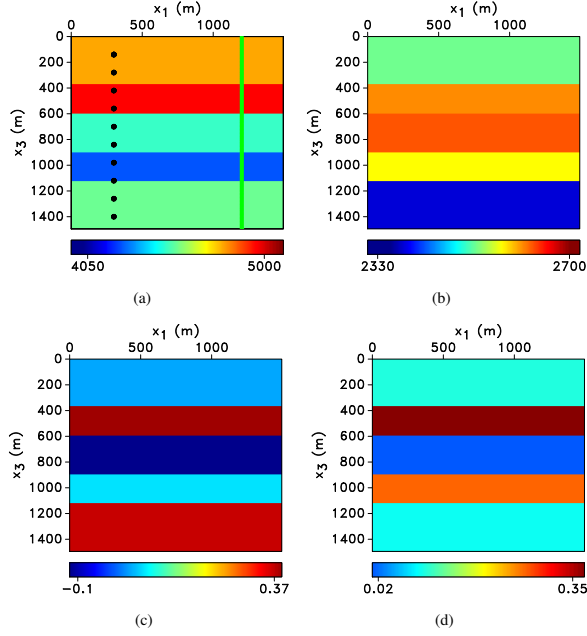

Figure 1: Sources (black dots) and receivers (magenta line) embedded in a layered VTI medium with the parameters (a) V_{hor}, (b) V_{S0}, (c) η, and (d) ϵ (the velocities are in m/s). The source mechanism is described by the moment-tensor elements $M_{11} = 0$, $M_{33} = 0$, and $M_{13} = 10^{10}$ N·m (i.e., it is a dip-slip source with a horizontal fault plane). The central frequency of the source signal is 20 Hz.


Figure 2: Actual (black), initial (magenta), and inverted (blue) parameters for the model in Figure 1: (a) V_{hor}, (b) V_{S0}, (c) η, and (d) ϵ (the velocities are in m/s). The profiles are plotted at $x_1 = 750$ m.

the vertical P- and S-wave velocities (V_{P0} and V_{S0}) and the anisotropy coefficients ϵ and δ. We parameterize the medium by $(V_{\mathrm{hor}}/V_{\mathrm{hor}_i})^2$, $(V_{S0}/V_{S0_i})^2$, $(1+2\eta)$, and $(1+2\epsilon)$, where V_{hor} is the P-wave horizontal velocity, η is the anellipticity parameter, and the subscript i stands for the initial value. The WI sensitivity analysis by Alkhalifah and Plessix (2014) shows that this parameterization is optimal for near-horizontal wave propagation typical for microseismic surveys.

SYNTHETIC EXAMPLE

We apply the algorithm to estimate the interval parameters of the horizontally layered (1D) VTI model from Figure 1. The inversion is carried out for a gridded 2D model with a spacing of 6 m and no smoothness constraints. The initial 1D model for all parameters is obtained by smoothing the actual fields in the vertical direction; in addition, V_{hor} in the middle layer is perturbed by 10%. The initial model produces no cycle skipping and the source parameters of all 10 microseismic events in the model are assumed to be known.

The inverted parameters V_{hor}, V_{S0}, η, and ϵ are close to the actual interval values (Figure 2). Indeed, V_{hor} should be well-constrained for the predominantly near-horizontal P-wave propagation in this experiment. As discussed by Alkhalifah and Plessix (2014), there are no trade-offs between V_{hor}, η, and ϵ for relatively large P-wave propagation angles with the symmetry axis.

In contrast, differences in the initial value of ϵ on the order of ± 0.1 lead to substantial errors in the inversion, which agrees with the results of Alkhalifah and Plessix (2014) for acoustic VTI media. Therefore, WI requires an accurate initial model for ϵ, which can be obtained from traveltime inversion.

ACKNOWLEDGMENTS

REFERENCES

Alkhalifah, T., and R. Plessix, 2014, A recipe for practical full-waveform inversion in anisotropic media: An analytical parameter resolution study: Geophysics, **79**, R91–R101.

Byrd, R. H., P. Lu, J. Nocedal, and C. Zhu, 1995, A limited memory algorithm for bound constrained optimization: SIAM Journal on Scientific Computing, **16**, 1190–1208.

Grechka, V., and S. Yaskevich, 2014, Azimuthal anisotropy in microseismic monitoring: A Bakken case study: Geophysics, **79**, KS1–KS12.

Jarillo Michel, O., and I. Tsvankin, 2014, Gradient calculation for waveform inversion of microseismic data in VTI media: Journal of Seismic Exploration, **23**, 201–217.

———, 2015, Estimation of microseismic source parameters by 2D anisotropic waveform inversion: Journal of Seismic Exploration, **24**, 379–400.

Anisotropic (VTI) elastic FWI: resolution analysis for walkaway VSP data
Olga Podgornova*, Scott Leaney, and Lin Liang, Schlumberger

Multi-parameter inversion

Multi-parameter full waveform inversion (FWI) of seismic data is known to have an issue of the parameters coupling, [1]. The origin of the coupling is low sensitivity (including none) of the data to certain distributions of medium properties, which can only be determined with high uncertainty or cannot be determined at all. Here, we establish ways of demonstrating that the spatial resolution and coupling between the physical parameters (wave velocity, density, anisotropy, etc.) are intertwined in case of finite frequency data. We analyze the coupling theoretically developing further the resolution analysis in the wavenumber domain [2], which is an extension of the conventional analysis of the radiation patterns, and compare theoretical predictions against numerical results for walkaway vertical seismic profiling (VSP) acquisition.

Resolution analysis in the wavenumber domain

Linearized multi-parameter inversion problem relates perturbations in the data δd with perturbations in the medium parameters δm_p as

$$\delta d\left(\mathbf{x}_s, \mathbf{x}_r, \omega\right) = \sum_p \int_{R^3} L_{m_p}(\mathbf{x}) \delta m_p(\mathbf{x}) d\mathbf{x}. \qquad (1)$$

The integral kernels L_{m_P} depend on the source and receivers coordinates $\mathbf{x}_s$ and $\mathbf{x}_r$, frequency ω, source wavelet, background parameters of the medium and parameterization m_P. For a plane-wave far-field approximation, homogeneous isotropic background and particular type of scattering (e.g. P-P, P-SV etc.), (1) can be transformed into the wavenumber domain [2]

$$\delta d^{AB}(\mathbf{k}, \omega) = \sum_p L_{m_p}^{AB}(\mathbf{k}, \omega) \delta \hat{m}_p(\mathbf{k}). \qquad (2)$$

The symbols A and B stand for the scattering type, $\mathbf{k}$ is the spatial wavenumber and $\delta \hat{m}_p(\mathbf{k})$ is the medium perturbation in the wavenumber domain. The relation between $\mathbf{k}$, ω and dip and scattering angles depends on the scattering type and takes the following forms:

$$\mathbf{k} = \omega\left(\frac{\gamma_s}{v_{P0}} + \frac{\gamma_r}{v_{P0}}\right), \ \mathbf{k} = \omega\left(\frac{\gamma_s}{v_{P0}} + \frac{\gamma_r}{v_{S0}}\right), \ etc. \qquad (3)$$

Here v_{P0}, v_{S0} are compressional and shear velocities of the background medium, γ_s and γ_r are unit directions between the imaging point and positions of the source and receiver and expressions of $L_{m_p}^{AB}$ are given in [2]. Directions γ_s, γ_r determine a scattering angle (angle between γ_s, γ_r) and dip angles (correspond to the direction of $\mathbf{k}$). Due to (3) the dependence on ω in (2) is equivalent to the dependence on the scattering angle.

For multi-frequency data, multiple scattering angles contribute to the same wavenumber providing different $L_{m_p}^{AB}$ coefficients and, so, resolve (some) parameters in (2). Different types of scattering have different sensitivity and, if combined together, they achieve better resolution than single type of scattering. Due to the limited illumination of the seismic acquisitions, the data lack some scattering angles and scattering types. Also, due to the finite frequency content of the data, only a subset of the scattering angles contribute to a particular wavenumber. For example, large scattering angles do not contribute to the large wavenumbers. These aspects underlie the spatial multi-parameter coupling.

Assembling all data contributing to the same wavenumber from all available scattering angles and scattering types we get a linear system

$$\delta \mathbf{d}(\mathbf{k}) = \mathbf{L}(\mathbf{k}) \delta \hat{\mathbf{m}}(\mathbf{k}). \qquad (4)$$

The spatial multi-parameter coupling can be analyzed through SVD of the matrix $\mathbf{L}$ (or $\mathbf{L}^* \mathbf{L}$) in (4).

Numerical Experiments

We consider a walkaway VSP acquisition with volumetric source (i.e. only P-P and P-SV scattering) for a one-layer model in a homogeneous isotropic background with $v_{P0} = 3000$ m/sec, $v_{S0} = 1700$ m/sec and density $\rho = 2$ g/cm³. We vary the depth of the layer, its thickness and its medium properties in different numerical experiments. Medium is parametrized by normalized density, compressional and shear velocities and Thomsen anisotropy parameters ε and δ.

The first experiment demonstrates a variation of the multi-parameter resolution with the scattering types. As Figures 1A and 1B show, contrasts of v_{S0} are structurally recovered up to the distance covered by P-P reflections while multi-parameter resolution degrades early with the loss of P-SV conversions and reflections. The lack of P-SV conversions affects the multi-parameter resolution more than the lack of P-SV reflections (compare Figures 1A and 1B). P-SV reflections and conversions are differentiated by the values of the scattering angles.

The second experiment demonstrates the spatial multi-parameter coupling at the area close to the receivers which is very well illuminated by both scattering angles and scattering types. To compare numerical results with the theory, we extract a vertical slice from the numerical result at a particular horizontal distance away from the well and transform it to the vertical wavenumber domain. Computing theoretical results, we only account for the scattering angles and scattering types that exist at the depth of the layer and distance of the slice. Figures 1A and 2B confirm the good quantitative agreement between

Anisotropic elastic FWI: resolution analysis for walkaway VSP data

theoretical predictions and numerical results. The exception is an area around zero wavenumber, $\mathbf{k} = 0$, which requires a separate theoretical treatment and is not discussed here. Singular values of $\mathbf{L}$ (Figure 2C) can be used as an estimate of the number of recoverable parameters at a particular spatial resolution. Preliminary analysis suggests

that four parameters can be recovered up to the spatial resolution of the converted P-SV waves. Higher spatial resolution compromises multi-parameter resolution. Sensitivity is also lost at low wavenumbers meaning that a good initial model is required.
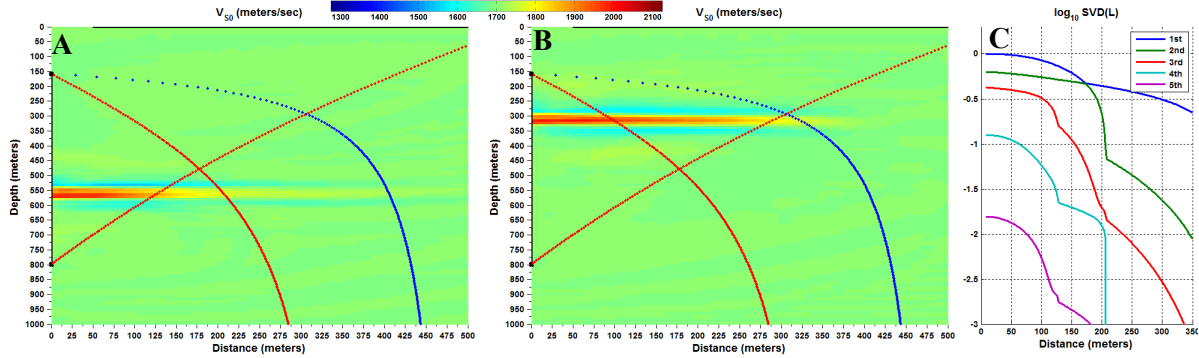

Figure 1. FWI results for the one-layer model with 40 m thickness v_{S0} contrast (25%): positioned at 560 m depth (A) and at 320 m depth (B). Only one parameter (v_{S0}) among five is shown. Coverage of the P-P reflections (blue dotted line) and P-SV reflections and transmissions (red dotted lines) are overlaid on the images. We do not plot limitations of the coverage due to the non-zero minimum source offset. Receivers cover depths between 160 m and 800 m, offsets of the sources are from 50 m till 970 m, source frequencies are 6Hz-60Hz. Singular values of $\mathbf{L}$ for the imaging point at 560 m depth depending on the horizontal distance away from the well (C). In (C), we neglect coupling between spatial and multi-parameter resolutions and consider only scattering angles and scattering types.
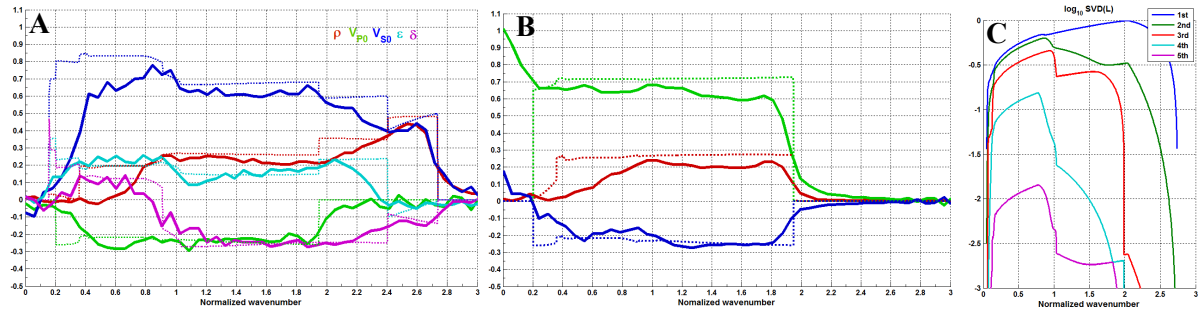

Figure 2. Theoretical (dotted) and numerical (solid) results for the spatial multi-parameter resolution for the horizontal layer perturbation (10%) of 10 m thickness. The layer is located at 545 m depth; results are compared at 40 m away from the well. We show results for the perturbation of v_{S0} (A) and v_{P0} (B) only; we also skip anisotropy parameters in B to simplify the plot. Acquisition parameters are as above, source frequencies are 9Hz-45Hz. Horizontal axis corresponds to the vertical wavenumber normalized by the smallest P-wavelength. Singular values of $\mathbf{L}$ (C).

Conclusions and discussion

We compared theoretical and numerical results of the spatial multi-parameter coupling in FWI for a walkaway VSP acquisition. Confirming a good agreement between these two, we consider a further use of the theory as a tool for the parameterizations study and/or estimation of the coupling in the inversion results. Theory also predicts some limits on the spatial resolution of the anisotropy parameters being the best near a vicinity of the receivers. Our current results do not account for the uncertainty in the source wavelet, non-linear and near field effects.

References

[1] Operto, S., Gholami, Y., Prieux, V., Ribodetti, A., Brossier, R., Metivier, L., and J. Virieux, 2013, A guided tour of multiparameter full-waveform inversion with multicomponent data: from theory to practice: The Leading Edge, 32(9).

[2] Podgornova, O., Leaney, S., and L. Liang, 2015, Analysis of resolution limits of VTI Anisotropy with full waveform inversion: SEG Technical program expanded abstracts.

Comparison of elastic stiffness and fracture model based approaches to FWI in HTI media

Morten Jakobsen, Department of Earth Science, University of Bergen

Introduction

The full waveform inversion (FWI) problem can generally be reduced to a sequence of linear inverse problems by using local optimization methods (Lee et al., 2010) or direct iterative inversion methods (Jakobsen and Ursin, 2015). However, each linearized inversion step is generally ill-posed, in the sense that some kind of regularization is generally required to find a stable and unique solution in the presence of model errors and noise. FWI in acoustic and anisotropic media share many of the same challenges, but the computational cost will obviously be larger in the anisotropic case than in the corresponding acoustic case. Also, there are often significant problems with cross-talk between the multiple model parameters that one needs to reconstruct in the anisotropic case (Lee et al., 2010). The problem with cross-talk can be potentially reduced by a reparameterization of the forward model (Lee et al., 2010; Kamath and Tsvankin, 2015), for example involving some kind of anisotropy parameters. However, the fact that one needs to reconstruct a relatively large number of model parameters for each grid block within a discretized seismic model also after a reparameterization involving anisotropy parameters represents a major challenge. If the seismic anisotropy is assumed to be caused by a single or multiple sets of aligned fractures then it may be a good idea to perform a FWI directly for the parameters of the fractures (e.g., fracture density) that determines all the independent components of the elastic stiffness tensors (Bansal and Sen, 2010; Pilskog et al., 2015; Jakobsen and Pilskog, 2016). This is because the number of unknown model parameters can then be significantly reduced, cross-talk effects will be significantly reduced and the parameters of the fratures represents a link to geological a priori information and applications within fractured reservoir engineering.

Born approximation for general anisotropic media

In the scattering-approach to seismic forward modelling in general anisotropic media (Jakobsen et al., 2015), one first decomposes the elastic stiffness tensor field of the actual medium into a suitable reference model with elastic stiffness tensor field $\mathbf{C}^{(0)}(\mathbf{x})$ and a corresponding stiffness perturbation field $\delta\mathbf{C}(\mathbf{x})$;

$$\mathbf{C}(\mathbf{x}) = \mathbf{C}^{(0)}(\mathbf{x}) + \delta\mathbf{C}(\mathbf{x}). \qquad (1)$$

The corresponding decomposition of the particle displacement vector field $\mathbf{u}(\mathbf{x})$ can be written as

$$\mathbf{u}(\mathbf{x}) = \mathbf{u}^{(0)}(\mathbf{x}) + \delta\mathbf{u}(\mathbf{x}), \qquad (2)$$

where $\mathbf{u}^{(0)}(\mathbf{x})$ is the particle displacement vector field in the reference model with elastic stiffness tensor field $\mathbf{C}^{(0)}(\mathbf{x})$ and $\delta\mathbf{u}(\mathbf{x})$ is the corresponding perturbation associated with $\delta\mathbf{C}(\mathbf{x})$. The Born approximation for the scattered wavefield $\delta\mathbf{u}(\mathbf{x})$ (Eaton and Stewart, 1994; Bansal and Sen, 2010) can be written in symbolic vector notation as (Jakobsen and Hudson, 2003)

$$\delta\mathbf{u}(\mathbf{x}) = -\int d\mathbf{x}' \nabla_s \mathbf{G}^{(0)}(\mathbf{x}, \mathbf{x}') : \delta\mathbf{C}(\mathbf{x}') : \nabla_s \mathbf{u}^{(0)}(\mathbf{x}') \qquad (3)$$

where $\mathbf{G}^{(0)}(\mathbf{x}, \mathbf{x}')$ is the elastic Green's function that gives the particle displacement at point $\mathbf{x}'$ due to a vector source at point $\mathbf{x}'$ in the reference model. The reference medium can in principle be selected arbitrarily as long as one knows the corresponding Green's function and the contrast is sufficiently small (Eaton and Stewart, 1994). The Green's function $\mathbf{G}^{(0)}(\mathbf{x}, \mathbf{x}')$ can be calculated using ray theory if the reference medium is sufficiently smooth. In general, however, it may be required to calculate the reference medium Green's function using a purely numerical approach (e.g., the finite difference method) or a volume integral equation method (Jakobsen and Hudson, 2003; Jakobsen et al., 2015).

Elastic stiffness based approach to FW in HTI media

For the special case of HTI media with the symmetry axis along the x_1 direction, one can (in 2D) decompose the elastic stiffness tensor perturbation field $\delta\mathbf{C}(\mathbf{x})$ as

$$\begin{aligned} \delta\mathbf{C}(\mathbf{x}) &= \mathbf{A}_1 \delta C_{11}(\mathbf{x}) + \mathbf{A}_2 \delta C_{33}(\mathbf{x}) \\ &+ \mathbf{A}_3 \delta C_{55}(\mathbf{x}) + \mathbf{A}_4 \delta C_{13}(\mathbf{x}), \end{aligned}$$

where $\mathbf{A}_r$ ($r = 1, ..., 4$) are constant 6×6 matrices where the elements are either 0, 1 or 2. From equations (3) and (4), it follows that the scattered wavefield is given by

$$\delta\mathbf{u}(\mathbf{x}) = \sum_{r=1}^{4} \int_D d\mathbf{x}' \mathbf{J}_r^{(0)}(\mathbf{x}, \mathbf{x}') \delta\mathbf{m}_r(\mathbf{x}'), \qquad (4)$$

where

$$\delta\mathbf{m}_1 = \delta\mathbf{C}_{11}, \ \delta\mathbf{m}_2 = \delta\mathbf{C}_{33}, \ \delta\mathbf{m}_3 = \delta\mathbf{C}_{55}, \ \delta\mathbf{m}_4 = \delta\mathbf{C}_{13}, \qquad (5)$$

and

$$\mathbf{J}_r^{(0)}(\mathbf{x}, \mathbf{x}') = \nabla_s \mathbf{G}^{(0)}(\mathbf{x}, \mathbf{x}') : \mathbf{A}_r : \mathbf{u}^{(0)}(\mathbf{x}'), \qquad (6)$$

represents the kernel of the Frechet functional derivative operator. After summing over discrete receivers, sources and frequencies and reorganization of the equations, the linear relation in equation (12) can be written in matrix form as

$$\delta\mathbf{d} = \mathbf{J}_1^{(0)} \delta\mathbf{m}_1 + \mathbf{J}_2^{(0)} \delta\mathbf{m}_2 + \mathbf{J}_3^{(0)} \delta\mathbf{m}_3 + \mathbf{J}_4^{(0)} \delta\mathbf{m}_4 \qquad (7)$$

where $\delta\mathbf{d}$ is a $N_d \times 1 = (3N_r N_s N_k) \times 1$ matrix containing the scattered wavefield data that one can observe at the receiver surface, $\mathbf{J}_r^{(0)}$ is a $N_d \times N$ matrix of Frechet derivatives; where N_r, N_s, N_k and N is the number of discrete receivers, sources, frequencies and grid blocks, respectively. The above equation can be rewritten exactly as

$$\delta\mathbf{d} = \mathbf{J}^{(0)} \delta\mathbf{m}, \qquad (8)$$

where $\mathbf{J}^{(0)} = \left[\mathbf{J}_1^{(0)}, \mathbf{J}_2^{(0)}, \mathbf{J}_3^{(0)}, \mathbf{J}_4^{(0)} \right]^T$ is a $N_d \times 4N$ matrix and $\delta\mathbf{m} = [\delta\mathbf{m}_1, \delta\mathbf{m}_2, \delta\mathbf{m}_3, \delta\mathbf{m}_4]$ is a $4N \times 1$ matrix containing the unknown model parameters (stiffness perturbations). The linearized seismic waveform inversion problem is to determine the vector with elastic stiffness perturbations from observations of the scattered wavefield data vector $\delta\mathbf{d}$.

Approaches to FWI in anisotropic media

We can use the Tikhonov regularization method to find an explicit least-squares solution (Jakobsen and Ursin, 2015):

$$\mathbf{m} = \mathbf{m}^{(0)} + \left[(\mathbf{J}^{(0)})^T \mathbf{J}^{(0)} + \lambda^2 \mathbf{I}_{4N} \right] (\mathbf{J}^{(0)})^T \left(\mathbf{d} - \mathbf{J}^{(0)} \mathbf{m}^{(0)} \right) \tag{9}$$

where $\mathbf{I}_{4N}$ is the $4N \times 4N$ unit matrix and λ is a regularization parameter. The reference model can be updated after each linearized inversion step using a generalized T-matrix approach to seismic modelling in anisotropic elastic media (Jakobsen et al., 2015). At each iteration, we use a combination of the L-curve method and a cooling scheme to estimate the optimal regularization parameter λ (see Jakobsen and Ursin, 2015).

Frature model based approach to FWI in HTI media

By using a Gassmann-consistent effective medium theory (Jakobsen and Pilskog, 2016), one can write

$$\delta \mathbf{C}(\mathbf{x}) = \mathbf{t}(\mathbf{x}) \varepsilon(\mathbf{x}), \tag{10}$$

where $\mathbf{t}$ is the so-called t-matrix and $\varepsilon(\mathbf{x}$ is the fracture density field that determines all the four elastic stiffness constants of a HTI medium (provided that one ones the storage porosity). It follows that the scattered wavefield is given by

$$\delta \mathbf{u}(\mathbf{x}) = \int_D d\mathbf{x}' \mathbf{J}_\varepsilon^{(0)}(\mathbf{x}, \mathbf{x}') \varepsilon(\mathbf{x}'), \tag{11}$$

where

$$\mathbf{J}_\varepsilon^{(0)}(\mathbf{x}, \mathbf{x}') = \nabla_s \mathbf{G}^{(0)}(\mathbf{x}, \mathbf{x}') : \mathbf{t}(\mathbf{x}') : \mathbf{u}^{(0)}(\mathbf{x}'), \tag{12}$$

represents the kernel of the Frechet functional derivative operator. After summing over discrete receivers, sources and frequencies and reorganization of the above equations, the linear relation in equation (11) can be written in matrix form as

$$\delta \mathbf{d} = \mathbf{J}_\varepsilon^{(0)} \varepsilon \tag{13}$$

where $\delta \mathbf{d}$ is a $N_d \times 1 = 3N_r N_s N_k \times 1$ matrix containing the scattered wavefield data that one can observe at the receiver surface, $\mathbf{J}_\varepsilon^{(0)}$ is a $N_d \times N$ matrix of Frechet derivatives. The matrix $\mathbf{J}_\varepsilon^{(0)}$ depends on the fracture density from the previous iteration, suggesting equation (13) is solved iteratively as detailed by Jakobsen and Pilskog (2016).

Numerical experpiments

We now consider the heterogeneous HTI (syncline) model in Figure 1 (top), consisting of 16 times 16 grid blocks (24 m in each direction). We assume 4 sources and 16 receivers uniformly distributed along a single line at the top of the model. The central frequency of the source (Ricker) wavelet is 7.5 Hz and we perform a simultaneous inversion of frequency domain data corresponding to 3, 6, 9, 12, 15 and 18 Hz. We add 1 percent random white Gaussien noise to the seismic waveform data to make the numerical experiment. Figure 1 middle and bottom shows the inverted stiffness models obtained using the elastic stiffness and fracture model based approaches to FWI in HTI media. Clearly, one can see that the inverted model obtained using the fracture model based approach is much closer to the true model than the inverted model obtained using the elastic stiffness based approach.
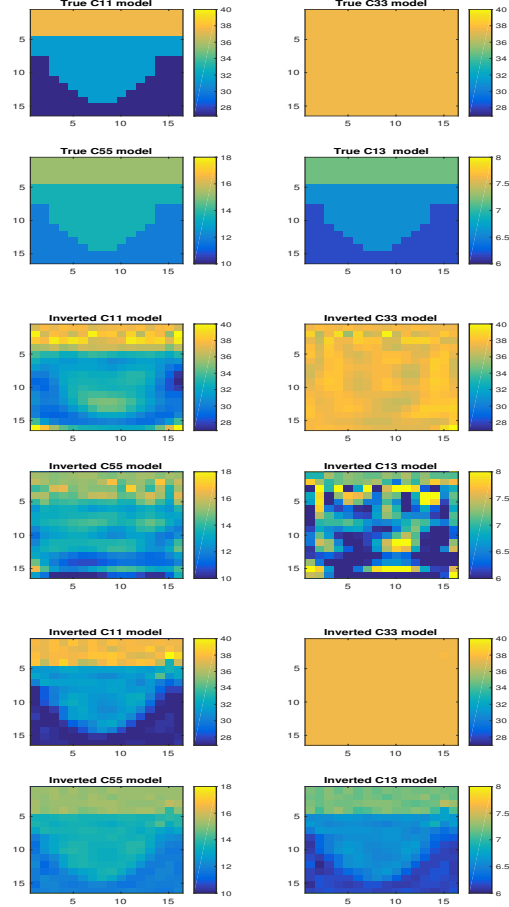

Figure 1: Comparison of the true stiffness model (top) with the elastic stiffness (middle) and fracture model (bottom) based approaches to FWI in (2D) HTI media.

Conclusion

The results of our numerical experiments suggest that the fracture model based approach to FWI in anisotropic media is superiour to the conventional stiffness based approach, but there is uncertainty associated with the underlying fracture model.

References

Bansal, R. and M. K. Sen, 2010, Ray-Born inversion for fracture paramerters, Geophys. J. Int., **180**, 1274-1288.

Eaton, D. W. S. and R. R., Stewart, 1994, Migration/inversion for transversely isotropic media, Geophys. J. Int., **119**, 667-683.

Jakobsen, M. and J. A. Hudson, 2003, Visco-elastic waves in rock-like composites. Studia Geophysica et Geodaetica, **47**, 793-826.

Jakobsen, M. and B. Ursin, 2015, Full waveform inversion in the frequency domain using direct iterative T-matrix methods, J. Geophys. Eng., **12**, 400-418.

Jakobsen, M., I. Pilskog, I. and M. Lopez, 2015, Generalized T-matrix approach to seismic modelling of fractured reservoirs and related anisotropic systems. Extended abstract, 77th EAGE meeting, Madrid.

Jakobsen, M. and I. Pilskog, 2016, Gassmann-consistent Born inversion for fracture density. Extended abstract, 78th EAGE meeting, Vienna.

Lee, H. Y., J., D. J. Koo, B. D. Min, B.D. Kwon, and H.S. Yoo, 2010, Frequency-domain elastic full waveform inversion for VTI media, Geophys. J. Int., **183**, 884-904.

Kamath, N. and I. Tsvankin, 2015, Sensitivity analysis for elastic full-waveform inversion in VTI media. Centre for Wave Phenomena report, CWP-805.

Pilskog, I., M., Lopez, M. and M. Jakobsen, 2015, Full waveform inversion for fracture parameters, Extended abstract, 77th EAGE meeting, Madrid.

Anisotropic attenuation in rocks: Theory, modelling and lab measurements

Václav Vavryčuk[1], Tomáš Svitek[2]*, Tomáš Lokajíček[2]

Affiliations:
[1] Institute of Geophysics, The Czech Academy of Sciences, Prague, Czech Republic
[2] Institute of Geology, The Czech Academy of Sciences, Prague, Czech Republic

Summary

Anisotropic attenuation affects seismic observations and complicates their interpretations. Its accurate determination is, however, difficult and needs extensive measurements of wavefields in many directions. So far, the travel time and amplitude decay of waves are usually measured along a sparse grid of propagation directions, and methods for inverting for anisotropic attenuation are not fully developed. In this paper, we present basic theory allowing a description and parameterization of general triclinic anisotropic attenuation. We develop and numerically test inversion schemes for determining the parameters of anisotropic attenuation. We present a lab facility that allows for measuring anisotropic attenuation using the P-wave ultrasonic sounding of spherical samples in 132 directions distributed regularly over the sphere. The applicability of the proposed inversion methods and the performance of the experimental setup are exemplified by determining triclinic anisotropic attenuation of the serpentinite rock from Val Malenco, Northern Italy. The ray velocity and ray attenuation were measured on a spherical sample of the rock with diameter of 45.5 mm at the room temperature and under two pressure levels: 0.1 and 20 MPa. The measurements confirmed that anisotropic attenuation is remarkably sensitive to confining pressure. Since cracks are closing with increasing pressure, attenuation decreases. However, changes in pressure can also induce changes in the directional variation of attenuation and a rotation of anisotropy axes.

Introduction

Anisotropic velocity and attenuation are efficiently described using a model of viscoelastic anisotropy. The viscoelastic parameters are complex valued and frequency dependent. Their real and imaginary parts describe elastic and attenuation anisotropy, respectively. The use of complex algebra allows for generalizing the theory developed for elastic anisotropy to viscoelastic anisotropy. The equations for waves in viscoelastic media are formally the same as in elastic media except for being complex. Implementing the complex algebra into equations is mathematically straightforward, but still some care is needed for understanding properly the physical meaning of all complex-valued quantities standing in the equations. The model of viscoelastic anisotropy has been successfully applied in theoretical studies of propagation of plane waves as well as of waves radiated by point sources. It was recognized that similarly to differentiating between the phase and ray velocities in elastic media, the phase and ray attenuation must be distinguished in attenuating media (Vavryčuk 2015). In this paper, we generalize theory of inversion for viscoelastic anisotropy developed by Vavryčuk (2015) to be applicable to measurements in lab or field experiments. We demonstrate how to calculate ray attenuation from amplitudes of signals propagated in anisotropic rocks and develop an iterative inversion method for parameters of viscoelastic anisotropy. The accuracy and robustness of the inversion is numerically tested. Finally, we demonstrate the determination of parameters of anisotropic attenuation on measurements of the serpentinite rock from Val Malenco, Northern Italy studied by Kern et al. (2015).

Method

Attenuation is usually determined from amplitude decay, however, this decay depends also on other factors. Therefore, we first determine elastic anisotropy of the rock from measurements of the ray velocity (Svitek et al. 2014). Second, we calculate the radiation pattern and geometrical spreading of elastic waves propagating in the rock. Third, we correct the measured amplitude decay of the signal for these two factors and normalize the corrected value to a unit ray length. The inversion for viscoelastic anisotropy is numerically tested on an example of the P wave propagating in a model of an orthorhombic viscoelastic medium. The synthetic velocity anisotropy is taken to correspond to the Torre Alfina xenolith with parameters taken from Pera et al. (2003, their Table 3). The velocity and attenuation values are used for calculating the complex phase velocity which is inverted for the weak anisotropy-attenuation parameters (WAA) of the medium. The inversion is performed using noise-free and noisy data. Noise is random with a uniform distribution. The noise level is different for the real and imaginary parts of the complex phase velocity c reflecting that the propagation velocity is usually measured with much higher accuracy than attenuation. The noise level for the real part of c varies from 0 to $\pm 3\%$ with step of 0.2%, and the level for the imaginary part of c varies from 0 to $\pm 15\%$ with step of 1%. To get statistically robust results, the random noise is generated 100 times and the results of the inversion are averaged over all noise realizations. Figure 1 shows a flowchart describing inversion process of measured data. We measured a spherical sample of diameter 45.5 mm of

Double click here to type your header

Figure 1 Flowchart of the inversion process
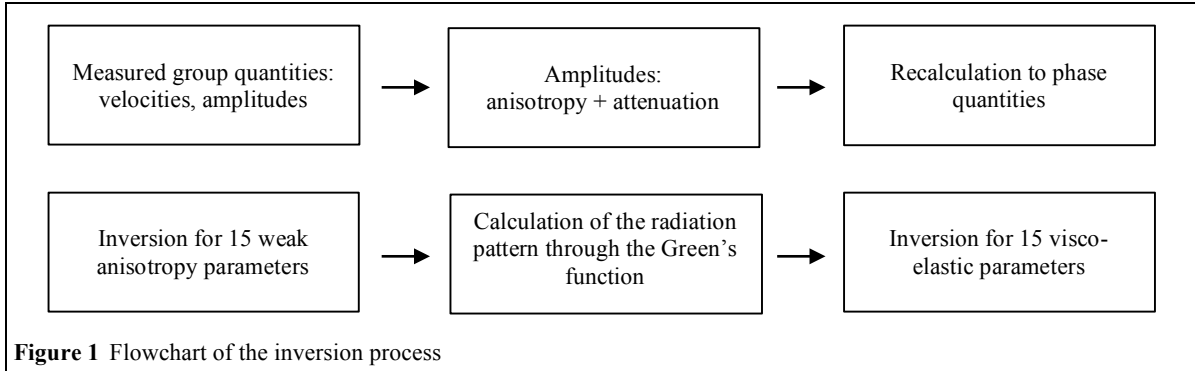
serpentinite from Val Malenco, Northern Italy (Kern et al., 2015). Data were measured in regular 15° grid providing 132 independent directions. Sensors with flat surface create with spherical surface of the sample a "quazi-point" contact. According to this condition we measure rather group (ray) quantities than phase quantities. Amplitudes of the signal include effects of anisotropy as well as attenuation. To separate these two effects, we first

recalculate group to phase quantities, invert for 15 weak anisotropy elastic parameters and through Green's function calculate radiation pattern. The next step is an inversion for visco-elastic parameters. The results of the inversion can be seen in Fig. 2 and 3. The predicted phase velocity, attenuation and Q-factor (Fig. 3) are very similar to the input phase data (Fig. 2) indicating that the inversion was successful.

References:

Kern, H., Lokajíček, T., Svitek, T. & Wenk, H.R., 2015. *Seismic anisotropy of serpentinite from Val Malenco, Italy*, J. Geophys. Res ., in press.

Pera, E., Mainprice, D. & Burlini, L., 2003. *Anisotropic seismic properties of the upper mantle beneath the Torre Alfina area (Northern Apennines, Central Italy)*, Tectonophysics ,370 , 11–30.

Svitek, T., Vavryčuk, V., Lokajíček, T. & Petružálek, M., 2014. *Determination of elastic anisotropy of rocks from P- and S-wave velocities: Numerical modelling and lab measurements*, Geophys. J. Int ., 199 (3), 1682-1697, doi: 10.1093/gji/ggu332.

Vavryčuk, V., 2015. *Determination of parameters of viscoelastic anisotropy from ray velocity and ray attenuation: Theory and numerical modeling*, Geophysics , 80 (3), C59-C71, doi: 10.1190/GEO2014-0355.1.
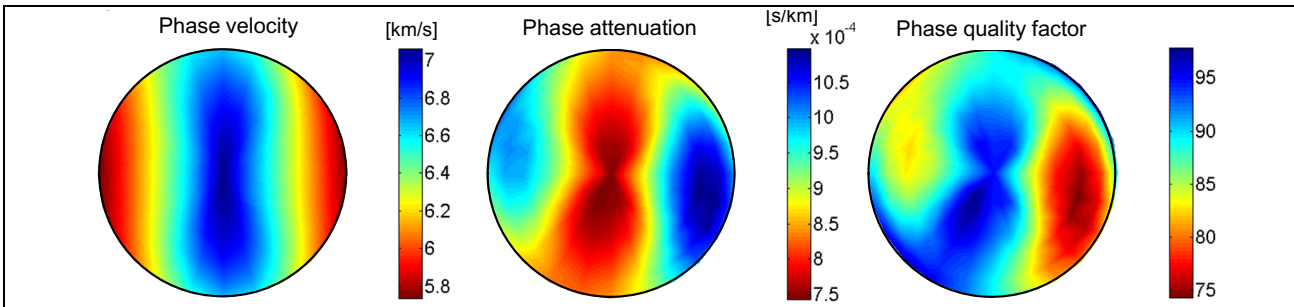
Figure 2 The phase velocity, attenuation and quality factor for the serpentinite sample at confining pressure of (a) 0.1 MPa and (b) 20 MPa. The phase quantities were calculated from the measured ray quantities and served as the input data for the inversion for parameters of viscoelastic anisotropy.
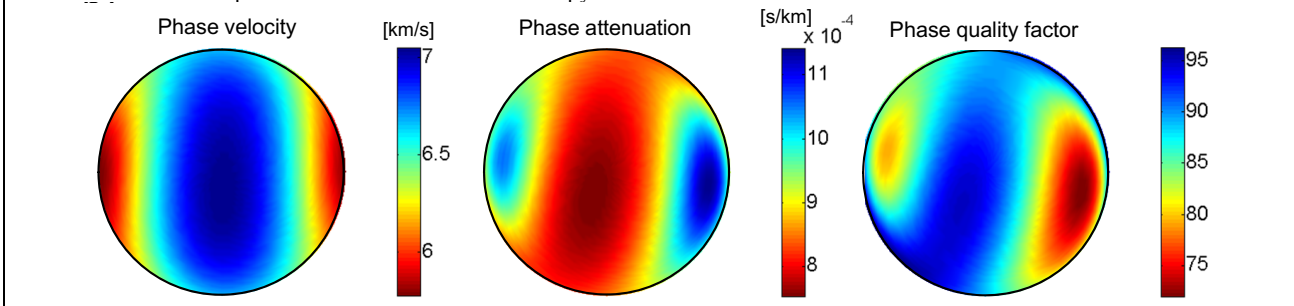
**Figure 3** The predicted phase velocity, attenuation and quality factor for the serpentinite sample at confining pressure of (a) 0.1 MPa and (b) 20 MPa. The phase quantities were calculated using the weak anisotropy-attenuation (WAA) parameters retrieved by the inversion.

Linear-Slip Model Revised—Part I: Shales

Tatiana Chichinina and Raul del Valle Garcia, Instituto Mexicano del Petróleo, México D.F.

We study feasibility of the Linear-Slip model application for rock physics and seismic exploration. The Linear Slip (LS) model developed by Schoenberg (1980; 1983) is an effective-medium anisotropy model for rocks with parallel micro-cracks (e.g. Schoenberg & Sayers, 1995). Only four independent stiffness-tensor components $\{C_{ij}\}$ totally identify the LS-model of transversely isotropic (TI) symmetry, in contrast to five necessary components inherent to the overall TI-model (e.g. Bakulin et al., 2000).

___The LS-model constraints on C_{13} and S_{13}___. The fifth stiffness-tensor component C_{13} ceases to be independent in the LS model, and turns into the following function of other components $\{C_{ii}\}$:

$$C_{13}{}^{LS} = \sqrt{C_{66}{}^2 - 2C_{33}C_{66} + C_{11}C_{33}} - C_{66}. \quad (1)$$

This restriction on the C_{13} for the LS model (of VTI-symmetry) can be rewritten in terms of the compliance-tensor components $\{S_{ij}\}$ as:

$$S_{13}=S_{12} \quad (2)$$

(e.g. Hsu & Schoenberg, 1993). The equality $S_{13}=S_{12}$ means also the equality $S_{31}=S_{21}$ due to the tensor symmetry $S_{ij}=S_{ji}$. The equality $S_{31}=S_{21}$ leads to the equality for Poisson's ratios $\nu_{13}=\nu_{12}$ (because of $S_{31}=-\nu_{13}/E_1$ and $S_{21}=-\nu_{12}/E_1$ in VTI rocks, e.g. Sayers (2013). Thus, the equality $\nu_{13}=\nu_{12}$ turns out to be a necessary condition for the feasibility of the LS model. However, actually in the overall VTI model, there must be *in*equality $\nu_{13}\neq\nu_{12}$. For example, for shale's rocks it should be the *in*equality $\nu_{13}>\nu_{12}$ (Yan et al., 2015). There is the *in*equality $\nu_{13}<\nu_{12}$ for thin-layered rocks (Sarout, 2016). Therefore, it turns out that the LS-model equality $\nu_{13}=\nu_{12}$ is not feasible for real TI rocks (Chichinina et al., 2015; 2016a).

___The physical sense of the compliances S_{31}, S_{21}___ (and/or Poisson's ratios ν_{13}, ν_{12}) becomes clear from the virtual experiment of uniaxial loading by σ_{11} (at horizontal axis x_1) of the VTI-rock-cylinder sample shown in Figures 1 and 2.
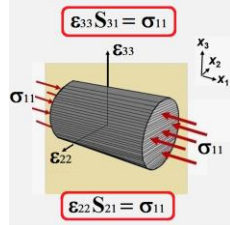

Figure 1. Uniaxial loading of horizontal rock-cylinder sample of VTI-symmetry, by the σ_{11}-stress. ε_{33} is the radial strain measured at the direction x_3 (normal to the cracks' planes); and ε_{22} is the strain parallel to the cracks' planes (in x_2-axis).

The LS-model condition, $\nu_{13}=\nu_{12}$, leads to *isotropic*-type equality of strains $\varepsilon_{33}=\varepsilon_{22}$, which is incomprehensible for the VTI-rocks, such as shale as an example (Chichinina et al., 2015, 2016a,b). Actually, because of the excess *compliances* of horizontal micro-cracks (shown by stretched springs in Fig.2,B) the strain ε_{33} at the normal-to-cracks axis x_3 should be greater than the parallel-to-cracks strain ε_{22} at the x_2. That is $\varepsilon_{33} > \varepsilon_{22}$ due to opening of micro-cracks under uniaxial loading σ_{11}. Actually, in shales the effective compliance tensor **S** is the sum ($\mathbf{S} = \mathbf{S^0} + \Delta\mathbf{S}$) of the host-rock compliance tensor $\mathbf{S^0}$, and the fracture-compliance tensor $\Delta\mathbf{S}$, which contains the excess compliances Z_N and Z_T for the horizontal micro-cracks in shales (e.g. Sayers, 1994, 1999, 2005, 2008, 2013, 2015).

___The deformation pattern predicted by the LS-model theory___ must be in a form of circle ($\varepsilon_{33}=\varepsilon_{22}$, shown in Fig.2, A). However, it is incomprehensible as it looks like an isotropy-type-deformation pattern that is contrary to the VTI-symmetry considered. Actually, in the VTI-model for fractured rocks, the deformation pattern should be in a form of ellipse ($\varepsilon_{33} > \varepsilon_{22}$), shown in Fig. 2, B. Thus, it turn out that the LS-model condition $S_{13}=S_{12}$ (that means $\varepsilon_{33} = \varepsilon_{22}$) were impossible and infeasible (Chichinina et al., 2015; 2016a).
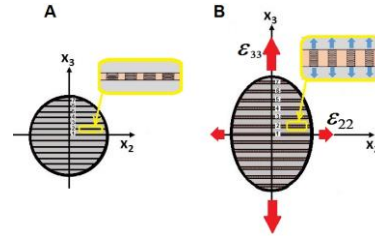

Figure 2. Cross section x_2x_3 of the *horizontal* VTI-rock-cylinder sample (shown in Fig.1) *before* (A) and *after* (B) uniaxial loading (by σ_{11}) along x_1-axis; the cross section (the plane x_2x_3) shown here is normal to the x_1-axis of loading. Red arrows show stress-induced radial deformations ε_{33} and ε_{22}, which are not equal, $\varepsilon_{33} > \varepsilon_{22}$, because of excess compliances of cracks (shown by stretched springs, all parallel to the VTI-symmetry axis x_3).

___Statistical analysis on C_{13} in real-rocks' data.___ We have studied the LS-model feasibility by testing the LS-model restriction on the C_{13}, eq.(1); we examined a number of published experimental data on elastic components $\{C_{ij}\}$ in shales' rocks (Thomsen (1986), Jakobsen & Johansen (2000), Wang (2002)) as shown in Fig.3. We have compared "true" elastic constant C_{13} found experimentally (from ultrasonic velocity measurements in shales' cores) with the theory-predicted constant $C_{13}{}^{LS}$ for the LS model (from eq.(1)), by estimating the relative difference between them as

$$\Delta C_{13}=(C_{13}{}^{LS} - C_{13})/C_{13}. \quad (3)$$

We found the deviation ΔC_{13} for shale rocks to be rather great: up to $\Delta C_{13}=100\%$ (shown in Fig. 3) (Chichinina et al., 2016a).

Linear-Slip Model Revised—Part I: Shales

Velocity patterns $V_P(\theta)$ and $V_{SV}(\theta)$. Given only four constants C_{11}, C_{33}, C_{44} and C_{66} (without C_{13}), we may reconstruct the velocities' patterns $V_{SH}(\theta)$, $V_P(\theta)$ and $V_{SV}(\theta)$, by use of the upper and lower bounds for C_{13} established by Yan et al. (2015): as $C_{13\_min} < C_{13} < C_{13\_max}$, where

$$C_{13\_max} = \sqrt{C_{33}(C_{11} - 2C_{66})}, \qquad (4)$$

$$C_{13\_min} = \sqrt{C_{33}(C_{11} - 2C_{66}) + C_{66}^2} - C_{66}. \qquad (5)$$
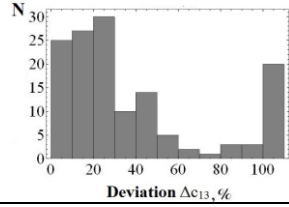

Figure 3. Histogram for N shale-rock samples, where N is the number of samples fallen in the certain interval of ΔC_{13}-deviation (shown at horizontal axis, in %). The deviation ΔC_{13} is defined by eq.(3).

Colored regions in Figure 4 show the area for all possible velocity patterns $V_P(\theta)$ and $V_{SV}(\theta)$ of P- and SV-waves.
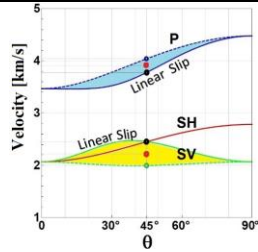

Figure 4. Phase velocities $V_P(\theta)$, $V_{SV}(\theta)$, and $V_{SH}(\theta)$, where θ is the wave–incidence angle relatively the VTI-symmetry axis (normal to fracture planes). All available values of $V_P(\theta)$, $V_{SV}(\theta)$ fell into the colored regions, with the bounds of C_{13} given by equations (4)–(5).

The input data (C_{11}, C_{33}, C_{44} and C_{66}) are taken from Sone & Zoback (2013) for shales Haynesville-1, P=20 MPa.

We found out that the formula for the lower bound C_{13_min} (eq. 5) coincides with the formula for $C_{13}{}^{LS}$ of the Linear-Slip model, eq. (1). Therefore, the velocity $V_P(\theta)^{LS}$ for the LS model coincides with the *lower-bound* velocity $V_P(\theta)_{min}$ (marked with the inscription "Linear Slip" in Figure 4):

$$V_P(\theta)^{LS} = V_P(\theta)_{min}.$$

(For the SV-wave velocity, $V_{SV}(\theta)^{LS} = V_{SV}(\theta)_{max}$.) Therefore, the LS-theory-predicted velocity pattern $V_P(\theta)^{LS}$ cannot provide the true velocity pattern $V_P(\theta)$ inherent to shales, because it represents only its' lower-bound velocity $V_P(\theta)_{min}$. The use of the LS-model-predicted constant $C_{13}{}^{LS}$ may lead to significant deviations in the estimates of $V_P(\theta)$, $V_{SV}(\theta)$ at all intermediate directions, i.e. between $\theta=0°$ and $\theta=90°$ (Chichinina et al., 2015, 2016a,b). Figure 5 shows $\Delta V_{P,SV}(\theta)$-velocity deviations as a function of ΔC_{13}-deviation. We estimated $\Delta V_{P,SV}(\theta)$ at the "middle angle" $\theta=45°$, as: $\Delta V_{P,SV45} = (V_{P,SV45} - V_{P,SV45}{}^{LS})/ V_{P,SV45}$. We found out that the ΔC_{13}-deviation affects more the $V_{SV}(\theta)$ than the $V_P(\theta)$ as shown in Fig.5.

The normal weakness Δ_N depends on the C_{13} by the following manner:

$$\Delta_N = 1 + (C_{13} - C_{33})/(2C_{66}) \qquad (6)$$

(for detail, see Chichinina et al., 2016c). Given the "true" constant C_{13}, one can estimate "true" Δ_N. However if the true C_{13} is unknown, one can use eq. (1) for the theory-

predicted $C_{13}{}^{LS}$, and obtain the theory-predicted $\Delta_N{}^{LS}$. We found out that this approach leads to erroneous result, because of the strong effect of the ΔC_{13}-deviation. It results in great relative difference $\partial(\Delta_N)$ between the real Δ_N and the theory-predicted $\Delta_N{}^{LS}$: $\partial(\Delta_N) = (\Delta_N - \Delta_N{}^{LS})/\Delta_N \cdot 100\%$, shown by green line in Fig. 5 (see also Chichinina et al., 2016c).
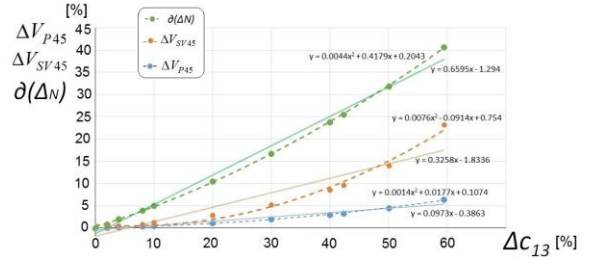

Figure 5. P-wave and SV-wave velocity deviations ΔV_{P45} and ΔV_{SV45} as a function of the deviation ΔC_{13} (eq.(3)). $\partial(\Delta_N)$-deviation of the normal weakness Δ_N is marked by green line.

Thomsen's (1980) parameter δ depends on C_{13}. By analogy with the relative difference $\partial(\Delta_N)$, we estimated the analogous difference $\Delta(\delta)$ in parameter δ as a function of ΔC_{13}, shown in Fig.6. Estimation of δ is affected by the deviation in C_{13} very much: the maximum $\Delta(\delta)$-deviation reaches 1400% .
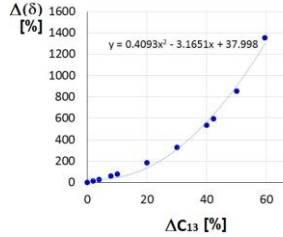

Figure 6. Deviation $\Delta(\delta)$ in Thomsen's parameter δ as a function of ΔC_{13}:
$$\Delta(\delta) = |(\delta^{LS} - \delta)/\delta^{LS}| \cdot 100\%.$$
Input data are the same as for Fig. 4 and Fig.5.

Conclusions

The LS-model constraint on the stiffness C_{13} (eq.1) is non-feasible for real rocks, and is always broken for shales as a certain example considered in this paper. Therefore, the use of the LS-model-predicted C_{13} can lead to inaccurate results in prediction of the $V_P(\theta)$- and $V_{SV}(\theta)$-velocities as well as in estimation of the normal weakness Δ_N and Thomsen's parameter δ. That in turn can lead to erroneous conclusions in fracture characterization of transversely isotropic hydrocarbon source rocks such as shales, for example, wrong crack-density estimation from inaccurate estimation of Δ_N. Moreover, it may lead to erroneous results of fluid-saturation analysis based on wrong estimate of the compliances' ratio Z_N/Z_T. The latter depends on estimation of the normal compliance Z_N, which in turn depends on the accuracy of Δ_N-estimation (for detail, see Chichinina et al., 2016c). In addition, it may cause erroneous results in estimation of Thomsen's parameter δ affected by the ΔC_{13}-deviation. The LS model works well only for the following two cases: the first is $\Delta_N=0$ (that is 100%-saturation of fluid, $\delta < 0$), and the second is $\Delta_N = \Delta_T$, which means $\delta = 0$.

References

Bakulin, A., V. Grechka, and I. Tsvankin, 2000, Estimation of fracture parameters from reflection seismic data—Part I: HTI model due to a single fracture set: Geophysics, **65**, 1788–1802.

Chichinina, T.I., I.R. Obolentseva, and G.A. Dugarov, 2015, Effective-medium anisotropic models of fractured rocks of TI symmetry: Analysis of constraints and limitations in Linear Slip model: 85th Annual International Meeting, SEG, Expanded Abstracts, 421–426.

Chichinina, T.I., I.R. Obolentseva, and G.A. Dugarov, 2016a, Critical analysis of theoretical basics of displacement-discontinuity model for media with oriented fractures: Tehnologii seismorazvedki (Seismic Technologies), N1, 31–43.

Chichinina, T.I., I.R. Obolentseva, and G.A. Dugarov, 2016b, Estimating applicability of the displacement-discontinuity model using experimental data on measurements of elastic-wave velocities: Seismic Technologies ("Tehnologii seismorazvedki", in Russian), No.2.

Chichinina, T., 2016c, Linear-Slip Model Revised—Part II: Estimation of Fracture Compliances: 17IWSA, Horseshoe Bay, Texas, September 18-23, 2016.

Hsu, C.-J., M. Schoenberg, 1993, Elastic waves through a simulated fractured medium: Geophysics, **58**, 964–977.

Jakobsen, M., T.A. Johansen, 2000, Anisotropic approximations for mudrocks: A seismic laboratory study: Geophysics, **65**, 1711–1725.

Sarout, J., 2016, Comment on "Physical constraints on c13 and δ for transversely isotropic hydrocarbon source rocks" by F. Yan, D.-H. Han and Q. Yao, *Geophysical Prospecting* 57, 393–411: Geophysical Prospecting (article first published online 2 February 2016).

Sayers, C.M., 1994, The elastic anisotropy of shales: Journal of Geophysical Research B 99, 767–774.

Sayers, C.M., 1999, Stress-dependent seismic anisotropy of shales: Geophysics, **64**, 93–98.

Sayers, C.M., 2005, Seismic anisotropy of shales: Geophysical Prospecting, **53**, 667-676.

Sayers, C.M., 2008, The effect of low aspect ratio pores on the seismic anisotropy of shales: 78th Annual International Meeting, SEG, Expanded Abstracts, 2750–2754.

Sayers, C.M., 2013, The effect of anisotropy on the Young's moduli and Poisson's ratios of shales: Geophysical Prospecting, **61**, 416–426.

Sayers, C.M. and Dasgupta, S., 2015, Elastic anisotropy of the Middle Bakken Formation: Geophysics, **80**, D23–D29.

Schoenberg, M., 1980, Elastic wave behavior across linear slip interfaces: J. Acoust. Soc. America, **68**, N5, 1516–1521.

Schoenberg, M., 1983, Reflection of elastic waves from periodically stratified media with interfacial slip: *Geophysical Prospecting,* **31,** 265–292.

Schoenberg, M., C.M. Sayers, 1995, Seismic anisotropy of fractured rock : Geophysics, **60**, 204–211.

Sone, H., M.D. Zoback, 2013, Mechanical properties of shale-gas reservoir rocks – Part I: Static and dynamic elastic properties and anisotropy: Geophysics, **78**, D381 –D392.

Thomsen, L., 1986, Weak elastic anisotropy: Geophysics, **51**, 1954–1966.

Wang, Z., 2002, Seismic anisotropy in sedimentary rocks, part 2: Laboratory data: Geophysics. **57**, 727–735.

Yan, F., D.-H. Han, Q.Yao, 2015, Physical constraints on c_{13} and δ for transversely isotropic hydrocarbon source rocks: Geophysical Prospecting, **57**, 393-411.

Linear-Slip Model Revised—Part II: Estimation of Fracture Compliances

Tatiana Chichinina and Raul del Valle Garcia, *Instituto Mexicano del Petróleo, México D.F.*

Summary

There are the normal and the tangential fracture compliances Z_N and Z_T used to be estimated from the velocity measurements in fractured rocks' samples [e.g. Hsu & Schoenberg, 1993; Sayers and Han, 2002; Angus et al. 2009; Lubbe et al. 2008; Verdon and Wustefeld, 2013; Choi et al., 2014; Yousef and Angus, 2016]. Accurate Z_N/Z_T-ratio estimation is important as a fluid-saturation indicator that is $Z_N/Z_T \rightarrow 1$ for dry (drained) cracks, and $Z_N/Z_T \rightarrow 0$ for fully saturated cracks (e.g. Hsu & Schoenberg, 1993; Bakulin et al., 2000).

In the Linear-Slip model, there is constraint on the stiffness-tensor component C_{13} (e.g. Hsu & Schoenberg, 1993):

$$C_{13}^{LS} = \sqrt{C_{66}^2 - 2C_{33}C_{66} + C_{11}C_{33}} - C_{66}. \tag{1}$$

This constraint leads to inaccurate estimation of fracture parameters such as the normal weakness Δ_N, and the normal compliance Z_N, as well as the compliances' ratio Z_N/Z_T. There is ΔC_{13}-deviation defined as

$$\Delta C_{13} = (C_{13}^{LS} - C_{13})/ C_{13}, \tag{2}$$

where C_{13} is the real constant obtained from the velocity measurements in a rock-core sample, and the C_{13}^{LS} is the theory-predicted constant, calculated from equation (1), e.g. Chichinina et al. (2015, 2016a, b, c). We revise accuracy of Δ_N- and Z_N/Z_T-estimation depending on the ΔC_{13}-deviation (shown in Figs.1-4), using published data of Hsu & Schoenberg (1993), and in addition, the data of Far (2011; 2014) from similar experiment with artificial fractured sample formed by compressed plexiglass plates.

In classic experiment of Hsu & Schoenberg (1993), the ΔC_{13}-deviation was small, with a maximum ΔC_{13}-deviation of ~4%, shown in Fig. 1 (by blue dashed line). Even in the case of these moderate ΔC_{13}-deviations, the estimation of the normal weakness Δ_N is not certain and unique, that is in contrast to the tangential weakness Δ_T (both shown in Fig.1). The tangential weakness Δ_T does not depend on C_{13} and therefore its estimation is unique and certain. The Δ_T is estimated as $\Delta_T = 1 - C_{44}/C_{66}$, $C_{44} = \rho V_{S0}^2$, and $C_{66} = \rho V_{SH90}^2$, where V_{S0} is the symmetry-axis shear-wave velocity at $\theta = 0°$ that is at the normal to fractures' planes; V_{SH90} is the SH-wave velocity at $\theta = 90°$.
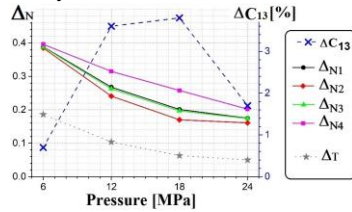

Figure 1. Normal weakness Δ_N estimated by 4 ways, eqs.(3)-(6), (colored solid lines), and the tangential weakness Δ_T (fine dotted

line with asterisks), versus pressure [MPa]. Blue dashed line (with crosses) shows the deviation ΔC_{13} (%), eq.(2), with its value given at the right-side scale axis. The data of Hsu & Schoenberg (1993) for the case of "dry cracks" (0%-saturation) is used.

However, the normal-weakness Δ_N-estimation is ambiguous, because of the C_{13}, which enters in it. The ΔC_{13}-deviation in C_{13}^{LS} implies inaccuracy in estimation of the normal weakness Δ_N (shown in Fig.1). Given stiffness tensor $\{C_{ij}\}$ for the LS model, the normal weakness Δ_N can be estimated by the following <u>four</u> different ways, depending on certain triplet combination: (C_{11},C_{33},C_{66}), or (C_{13},C_{33},C_{66}), or (C_{11},C_{33},C_{13}), or (C_{11},C_{66},C_{13}), which may enter in Δ_N:

$$\Delta_{N1} = \frac{1}{2C_{66}} \left[C_{66} - C_{33} + \sqrt{C_{66}^2 - 2C_{33}C_{66} + C_{11}C_{33}} \right], \tag{3}$$

$$\Delta_{N2} = 1 + (C_{13} - C_{33})/(2C_{66}), \tag{4}$$

$$\Delta_{N3} = \frac{C_{33}(C_{11} - C_{33})}{C_{33}C_{11} - C_{13}^2}, \tag{5}$$

$$\Delta_{N4} = \frac{(C_{11} - C_{13} - 2C_{66})(C_{13} + C_{66})}{2C_{66}(C_{11} - 2C_{66})}. \tag{6}$$

The first method for Δ_N–estimation (eq.(3)) is based on the LS-model restriction for C_{13}^{LS} (eq.(1)). This method is suitable only in the case, when the condition (1) for C_{13} is met; that means zero ΔC_{13}-deviation. All four methods give the same result in this case of $\Delta C_{13} = 0$. In fairness, we may note that our two ways (of the total four) in Δ_N-estimation are the same as those in the article of Hsu & Schoenberg (1993) (unfortunately their equations were written in an implicit form there). Thus, we have found two more ways of Δ_N–estimating (eq.(5) and eq.(6)) in addition to those two given by Hsu & Schoenberg (1993).

Given Δ_N (Fig.1), we can obtain the normal compliance Z_N as $Z_N = \Delta_N/C_{33}$, using $C_{33} = (\lambda + 2\mu)(1 - \Delta_N)$, or $C_{33} = \rho V_{P0}^2$, where V_{P0} is the P-wave velocity at $\theta = 0°$ that is at the normal to fractures' planes. The tangential compliance Z_T can be estimated as $Z_T = \Delta_T/C_{44}$, where $C_{44} = \mu(1 - \Delta_T)$ or $C_{44} = \rho V_{S0}^2$. Finally, we can estimate the normal-to-tangential-compliance ratio Z_N/Z_T by 4 ways, as shown in Figure 2. Thus, four different Δ_N-estimations (eqs. (3)-(6)) have led to four different estimates of Z_N/Z_T-ratio.
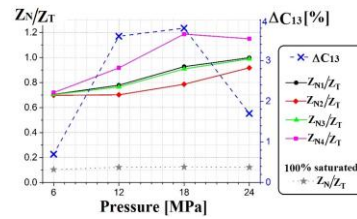

Figure 2. The normal-to-tangential-compliance ratio Z_N/Z_T estimated by four ways for dry-cracks' model (shown by solid

Linear-Slip Model Revised—Part II: Estimation of Fracture Compliances

line). The gray dotted line (with asterisks) denotes the ratio Z_N/Z_T at 100%-saturation (honey was used as a saturation fluid).

In the experiments of Far (2011, 2014), the plates'-stack models were used in two versions: 1-*the first model includes* penny-shaped rubber inclusions inserted between the plexiglass plates, and 2-*the second one* is the usual model of plates, which is similar to that of Hsu-Schoenberg (1993). Far (2011) carried out experiments with both models at two frequency ranges: the low frequency range of 90/120 kHz and the higher frequency range with f_{max}=480 kHz. Fig. 3 shows the larger deviations ΔC_{13} estimated for the model with inclusions (marked by triangles ▲ and ▼) than the model without inclusions (the latter marked by ■ and ♦). Therefore, we have obtained enormous dispersion in Δ_N- and Z_N- estimations in the model with inclusions, in comparison with the model without inclusions. Consequently, this leads to a conclusion that the Linear-Slip model is not suitable for the model with inclusions in the experiment of Far (2011). Whilst in the usual model of plates (without inclusions, f_{max}=480 kHz (♦)), we estimated even less ΔC_{13}-deviation (for the pressures P > 6.5MPa) than in the experiment of Hsu-Schoenberg (●) as shown in Fig.3.
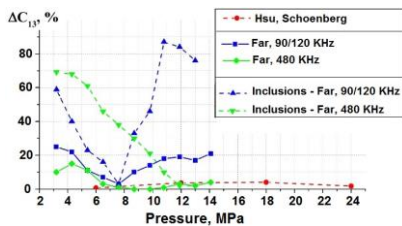
**Figure 3.** ΔC_{13}-deviation (defined by eq. (2)) estimated from the data on the velocity measurements in plexiglass-plate-stack models (Hsu & Schoenberg, 1993; Far, 2011). The notation "inclusions" in the legend means the model with rubber discs.

Given Δ_N estimated by four ways according to the formulas (3)-(6), we have four estimates of Z_N/Z_T, shown in Fig.4 for the model without inclusions, f_{max}=480 kHz.
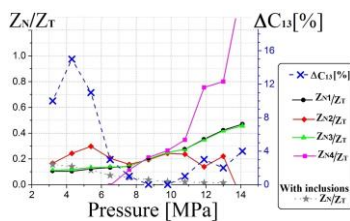

Figure 4. Z_N/Z_T estimated by 4 ways from the data of Far (2011), without inclusions, f_{max}=480KHz (colored solid lines with symbols, the notation is the same as in Figs. 1-2). Blue dashed line (with crosses) shows the deviation ΔC_{13} (%).The gray dotted line (with asterisks) denotes the ratio Z_N/Z_T estimated for the model with cracks filled with rubber inclusions (f_{max}=480KHz).

There were no any experiment by Far (2011) with fluid saturation, and therefore, for the comparison we have

inserted an additional chart obtained for the model with rubber inclusions, marked by gray dotted line with asterisks in Fig.4. By comparing Z_N/Z_T in these two experiments with filled cracks (by Hsu & Schoenberg (1993) and by Far (2011)) shown in Figure 2 and Figure 4, it becomes clear that the case of the cracks with rubber inclusions is somewhat similar to the case of honey-filled cracks. Actually, in both experiments, the Z_N/Z_T-ratio (Z_N/Z_T→0) is smaller than that in empty cracks (without infill) that is due to similar reduced bulk modulus K in rubber and honey, which is comparable with the shear modulus μ in the host rock. This is in a good agreement to the theory, according to which $(Z_N/Z_T)^{dry} > > (Z_N/Z_T)^{saturated}$ (e.g. Bakulin et al., 2000).

Conclusions

Given formulas (3)-(6), there are four ways in the Δ_N–estimation; these have resulted in four different Z_N-compliance estimates. Given four estimates of Z_N, we have obtained four different estimates for the compliances' ratio Z_N/Z_T from the input data on $\{C_{ij}\}$ for the experiment of Hsu & Schoenberg shown in Figure 2, (as well as four different Z_N/Z_T-estimations for Far´s experiment shown Figure 4). These four Z_N/Z_T–estimations coincide only when the deviation ΔC_{13} goes to zero: ΔC_{13}→0.

In real rocks, because of the great ΔC_{13}-deviation estimated by the analysis of rock-samples data (e.g. Chichinina et al. 2016-a, b, c), the uncertainty in Z_N/Z_T-estimation may result in inaccuracy in fluid-saturation prediction. In seismic exploration, it may lead to ambiguity in distinguishing gas from water in fractures as an example. Following the theory, Z_N/Z_T should go to zero for water-saturated cracks, Z_N/Z_T→0, and Z_N/Z_T→1 for gas-filled cracks; however, there is great dispersion found out in Z_N/Z_T-estimation that makes infeasible an accurate prediction of the crack infill. That is to say, there is no single solution in the problem of estimating of the normal fracture weakness Δ_N (and the Z_N) from a given LS-stiffness tensor $\{C_{ij}\}$ because of the inherent LS-stiffness-tensor inconsistency.

Despite the well-established practice of the LS-model usage for identification and characterization of naturally fractured reservoirs (e.g. Bakulin et al., 2000) as well as gas-shale plays (Sayers, 1999, 2005, 2008, 2013), we recommend its application *with great precaution*. Based on the infeasible and unjustified condition for the C_{13}, eq. (1), the Linear-Slip model is flawed. The limitation on the C_{13} is incorrect for majority of real rocks, moreover, it is contradictory to the physical sense of elastic and geomechanics properties of TI rocks (Chichinina et al., 2015, 2016-a,b,c). Presented examples have confirmed our general conclusion on impracticability of the LS-model application in estimation of the fracture compliance Z_N as well as the Z_N/Z_T-ratio for seismic fracture characterization.

Linear-Slip Model Revised—Part II: Estimation of Fracture Compliances

References

Angus, D.A., J.P. Verdon, Q.J. Fisher, and J.-M. Kendall, 2009, Exploring trends in microcrack properties of sedimentary rocks: An audit of dry-core velocity-stress measurements: Geophysics, **74**, N.5, E193–E203.

Bakulin, A., V. Grechka, and I. Tsvankin, 2000, Estimation of fracture parameters from reflection seismic data—Part I: HTI model due to a single fracture set: Geophysics, **65**, 1788–1802.

Chichinina, T.I., I.R. Obolentseva, and G.A. Dugarov, 2015, Effective-medium anisotropic models of fractured rocks of TI symmetry: Analysis of constraints and limitations in Linear Slip model: 85th Annual International Meeting, SEG, Expanded Abstracts, 421–426.

Chichinina, T., 2016-a, Linear-Slip Model Revised—Part I: Shales: 17IWSA, Horseshoe Bay, Texas, September 18-23, 2016.

Chichinina, T.I., I.R. Obolentseva, and G.A. Dugarov, 2016-b, Critical analysis of theoretical basics of displacement-discontinuity model for media with oriented fractures: Seismic Technologies ("Tehnologii seismorazvedki", in Russian), No.1, 31–43.

Chichinina, T.I., I.R. Obolentseva, and G.A. Dugarov, 2016-c, Estimating applicability of the displacement-discontinuity model using experimental data on measurements of elastic-wave velocities: Seismic Technologies ("Tehnologii seismorazvedki", in Russian), No.2.

Choi, M.-K., A. Bobet, and L.J. Pyrak-Nolte, 2014, The effect of surface roughness and mixed-mode loading on the stiffness ratio $\kappa x / \kappa z$ for fractures: Geophysics, **79**, N.5, D319–D331.

Far, M., 2011, Seismic characterization of naturally fractured reservoirs: PhD Thesis. University of Houston.

Far, M., J.J.S. Figueiredo, R.R.Stewart, J.P. Castagna, D-H. Han, N. Dyaur, 2014, Measurements of seismic anisotropy and fracture compliances in synthetic fractured media: Geophys. J. Int., **197**, No. 3, 1845–1857.

Hsu, C.-J., M. Schoenberg, 1993, Elastic waves through a simulated fractured medium: Geophysics, **58**, 964–977.

Lubbe, R., J. Sothcott, M.H. Worthington and C. McCann, 2008, Laboratory estimates of normal and shear fracture compliance: Geophysical Prospecting, **56**, 239–247.

Sayers, C.M., 1999, Stress-dependent seismic anisotropy of shales: Geophysics, **64**, 93–98.

Sayers C.M., 2005, Seismic anisotropy of shales: Geophys. Prosp. **53**, 667-676.

Sayers, C.M., 2008, The effect of low aspect ratio pores on the seismic anisotropy of shales: 78th Annual International Meeting, SEG, Expanded Abstracts, 2750–2754.

Sayers C.M., 2013, The effect of anisotropy on the Young's moduli and Poisson's ratios of shales: Geophys. Prosp., **61**, 416–426.

Sayers, C.M. and D.-H. Han, 2002, The effect of pore fluid on the stress-dependent elastic wave velocities in sandstones, SEG International Exposition and 72nd Annual Meeting. Salt Lake City.

Verdon, J.P. and A. Wustefeld, 2013, Measurement of the normal/tangential fracture compliance ratio (*ZN/ZT*) during hydraulic fracture stimulation using S-wave splitting data: Geophysical Prospecting, **61** (Suppl. 1), 461–475.

Yousef, B.M., D.A. Angus, 2016, When do fractured media become seismically anisotropic? Some implications on quantifying fracture properties: Earth and Planetary Science Letters, **444,** 150–159.

An acoustic eikonal equation for attenuating, orthorhombic media

Qi Hao*, NTNU; Tariq Alkhalifah, KAUST

Summary

We have presented an acoustic eikonal equation governing the complex-valued traveltime of P-waves in attenuating, orthorhombic media. The eikonal equation has been solved by the combination of perturbation theory and Shanks transform. For a horizontal, attenuating orthorhombic layer, the imaginary part of the complex-valued reflection traveltime has the non-hyperbolic behavior.

Introduction

For an attenuating, orthorhombic medium, the complex-valued traveltime is expressed by $t = t_R + it_I$, where "i" denotes the imaginary unit, t_R and t_I denote its real and imaginary parts.

The combination of Tsvankin's (1997) and Zhu and Tsvankin's (2006) notations entirely describe an attenuating, orthorhombic medium. If we use only P-waves, as is done in practical cases, however, we may consider the acoustic assumption that the P-wave velocity and attenuation are independent of the shear-wave velocity parameter υ_{S0} defined in Tsvankin's (1997) notation. By setting υ_{S0} zero, some shear-wave parameters from Tsvankin's (1997) notation and Zhu and Tsvankin's (1997) disappear in the P-wave attenuating eikonal equation. This means that we may use fewer parameters to describe the P-wave traveltime in attenuating orthorhombic media.

For an attenuating orthorhombic medium under the acoustic assumption, its non-attenuating reference may be appropriately characterized by the modified Alkhalifah's (2003) notation, which includes the velocity υ_{P0} of vertically propagating P-waves, the normal moveout (NMO) velocities υ_{n1} and υ_{n2} defined in the [y, z] and [x, z] symmetry planes, the anellipticity parameters η_1, η_2 and η_3 defined in the [y, z], [x, z] and [x, y] symmetry planes. Besides, we also use the following parameters from Zhu and Tsvankin's (2007) notation: the attenuation coefficient A_{P0} of P-waves propagating along z-axis, the fractional differences ε_{Q1} and ε_{Q2} between the attenuation coefficients, defined in the y- and z-directions, and defined in the x- and z-directions; the second-order derivatives δ_{Q1}, δ_{Q2} and δ_{Q3} of the P-wave attenuation coefficient, defined in the [y, z], [x, z] and [x, y] symmetry planes, respectively.

The acoustic eikonal equation

For attenuating, orthorhombic media with the symmetry planes orthogonal to the Cartesian coordinates, we derive the eikonal equation under the acoustic assumption,

$$\begin{vmatrix} c_{11}\tau_{,x}^2 - 1 & c_{12}\tau_{,x}\tau_{,y} & c_{13}\tau_{,x}\tau_{,z} \\ c_{12}\tau_{,x}\tau_{,y} & c_{22}\tau_{,y}^2 - 1 & c_{23}\tau_{,y}\tau_{,z} \\ c_{13}\tau_{,x}\tau_{,z} & c_{23}\tau_{,y}\tau_{,z} & c_{33}\tau_{,z}^2 - 1 \end{vmatrix} = 0 , \tag{1}$$

where the subscript "," denotes the spatial derivative; for example, $\tau_{,x}$ denotes the partial derivative of complex-valued traveltime τ with respect to x variable; c_{ij} are density-normalized stiffness coefficients,

$$c_{11} = \upsilon_{n2}^2(1 - 2ik(1 + \varepsilon_{Q2}))(1 + 2\eta_2) , \tag{2}$$

$$c_{12} = \upsilon_{n1}\upsilon_{n2}\eta_{xy}(1 - 2ik(1 + \varepsilon_{Q2})) - ik\delta_{Q3}(1 + \varepsilon_{Q2})\frac{\upsilon_{n2}^3(1 + 2\eta_2)^2}{\upsilon_{n1}\eta_{xy}} , \tag{3}$$

$$c_{13} = \upsilon_{P0}\upsilon_{n2}(1 - 2ik) - ik\delta_{Q2}\frac{\upsilon_{P0}^3}{\upsilon_{n2}} , \tag{4}$$

$$c_{22} = \upsilon_{n1}^2(1 - 2ik(1 + \varepsilon_{Q1}))(1 + 2\eta_1) , \tag{5}$$

$$c_{23} = \upsilon_{P0}\upsilon_{n1}(1 - 2ik) - ik\delta_{Q1}\frac{\upsilon_{P0}^3}{\upsilon_{n1}} , \tag{6}$$

$$c_{33} = \upsilon_{P0}^2(1 - 2ik) , \tag{7}$$

with

$$k = \frac{A_{P0}}{1 - A_{P0}^2} , \quad \eta_{xy} = \sqrt{\frac{(1 + 2\eta_1)(1 + 2\eta_2)}{1 + 2\eta_3}} . \tag{8}$$

From equation 1, we obtain the acoustic eikonal equation in the [x, z] plane of an attenuating, transversely isotropic medium,

$$A\tau_{,x}^2 + B\tau_{,z}^2 + C\tau_{,x}^2\tau_{,z}^2 = 1 , \tag{9}$$

with

$$A = \upsilon_n^2(1 - 2ik(1 + \varepsilon_Q))(1 + 2\eta) , \tag{10}$$

$$B = \upsilon_{P0}^2(1 - 2ik) , \tag{11}$$

$$C = \frac{\upsilon_{P0}^2}{\upsilon_n^2}((1 - 2ik)\upsilon_n^2 - ik\delta_Q\upsilon_{P0}^2)^2 \\ - \upsilon_{P0}^2\upsilon_n^2(1 - 2ik)(1 - 2ik(1 + \varepsilon_Q))(1 + 2\eta) \tag{12}$$

where υ_n denotes the NMO velocity, η denotes the anellipticity parameter, ε_Q and δ_Q are the attenuation-anisotropy parameters.

The approximate solution

We adopt a perturbation method to solve equation 1. The vector of perturbation parameters is defined as

$$\boldsymbol{\ell} = (\eta_1, \eta_2, \eta_3, \varepsilon_{Q1}, \delta_{Q1}, \varepsilon_{Q2}, \delta_{Q2}, \delta_{Q3})^T , \tag{13}$$

to represent the trial solution to equation 1,

$$\tau = \tau_0 + \sum_{i=1}^{8} \tau_i \ell_i + \sum_{i,j=1; i \le j}^{8} \tau_{ij} \ell_i \ell_j . \tag{14}$$

An acoustic eikonal equations for attenuating, orthorhombic media

From equations 1 and 14, we derive the following equations for the traveltime coefficients τ_0, τ_i (i=1,…,8) and τ_{ij} (i,j=1,…,8, and $i \leq j$),

$$\upsilon_{n2}^2 \tau_{0,x}^2 + \upsilon_{n1}^2 \tau_{0,y}^2 + \upsilon_{P0}^2 \tau_{0,z}^2 = \frac{1}{1-2ik} \quad , \qquad (15)$$

$$\upsilon_{n2}^2 \tau_{0,x}\tau_{i,x} + \upsilon_{n1}^2 \tau_{0,y}\tau_{i,y} + \upsilon_{P0}^2 \tau_{0,z}\tau_{i,z} = f_i(\tau_0) , \qquad (16)$$

$$\upsilon_{n2}^2 \tau_{0,x}\tau_{ij,x} + \upsilon_{n1}^2 \tau_{0,y}\tau_{ij,y} + \upsilon_{P0}^2 \tau_{0,z}\tau_{ij,z} = f_{ij}(\tau_0,\tau_1,...,\tau_8) . \quad (17)$$

Applying Shanks transform to equation 14 leads to

$$\tau = T_0 + \frac{T_1^2}{T_1 - T_2} \quad , \qquad (18)$$

with

$$T_0 = \tau_0 \quad , \quad T_1 = \sum_{i=1}^8 \tau_i \ell_i \quad , \quad T_2 = \sum_{i,j=1; i \leq j}^8 \tau_{ij}\ell_i\ell_j \quad . \qquad (19)$$

Figures 1 and 2 illustrate that equation 19 is accurate for homogeneous, attenuating, orthorhombic media with strong attenuation and attenuation anisotropy.

A horizontal, attenuating, orthorhombic layer

Assuming $A_{P0} \ll 1$, the real-part t_R of the traveltime is independent of A_{P0} and all attenuation-anisotropy parameters. For a horizontal, attenuating, orthorhombic reflector, we obtain the expansion of the imaginary part t_I,

$$t_I^2(r,\alpha) = A_{P0}^2 \left(t_0^2 + \frac{r^2}{\upsilon_Q^2(\alpha)} - \frac{2\eta_Q(\alpha)r^4}{t_0^2 \upsilon_Q^4(\alpha)} \right) , \qquad (20)$$

where t_0 denotes the two-way zero-offset traveltime in the non-attenuating reference; r denotes the radial source-receiver offset; $\upsilon_Q(\alpha)$ and $\eta_Q(\alpha)$ are functions of acquisition azimuth α, describing the azimuthal NMO velocity and anellipticity for the time t_I / A_{P0}; $\upsilon_Q(\alpha)$ is given by

$$\frac{1}{\upsilon_Q^2(\alpha)} = \frac{\sin^2\alpha}{\upsilon_{Q1}^2} + \frac{\cos^2\alpha}{\upsilon_{Q2}^2} \quad , \qquad (21)$$

with

$$\upsilon_{Q1} = \frac{\upsilon_{P0}(1+2\delta_1)}{\sqrt{1+2\delta_1+2\delta_{Q1}}} \quad , \quad \upsilon_{Q2} = \frac{\upsilon_{P0}(1+2\delta_2)}{\sqrt{1+2\delta_2+2\delta_{Q2}}} , \qquad (22)$$

where υ_{Q1} and υ_{Q2} are the NMO velocities for t_I / A_{P0} along y- and x-axes, respectively; δ_1 and δ_2 are the Thomsen parameters defined in the $[y, z]$ and $[x, z]$ symmetry planes of a non-attenuating, orthorhombic media. Figure 3 shows an example of the azimuthal variations of NMO velocities and anellipticities for t_R and t_I / A_{P0}.

Conclusions

The acoustic eikonal equation describes the complex-valued traveltime of P-waves in attenuating, orthorhombic media. The combination of a perturbation method and Shanks transform provides an accurate solution to the acoustic eikonal equation for homogeneous, attenuating, orthorhombic media. For a horizontal attenuating orthorhombic layer, the imaginary part of complex-valued traveltime as a function of the acquisition azimuth and the source-receiver offset has a non-hyperbolic behavior.

References
Alkhalifah, T., 2003, An acoustic wave equation for orthorhombic anisotropy: Geophysics, **68**, 1169–1172.
Tsvankin, I., 1997, Anisotropic parameters and P-wave velocity for orthorhombic media: Geophysics, **62**, 1292-1309.
Zhu, Y., and I. Tsvankin, 2007, Plane-wave attenuation anisotropy in orthorhombic media: Geophysics, **72**(1), D9-D19.
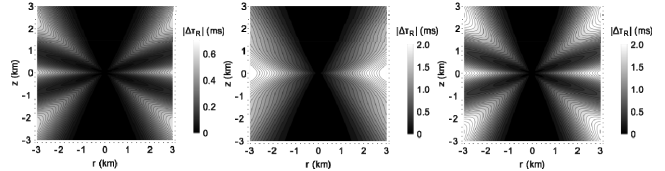
Figure 1. Absolute errors in the real part of the complex-valued traveltime from equation 18 for a homogeneous, attenuating orthorhombic medium. The plots correspond to propagation azimuths 0 (left), $\pi / 4$ (middle) and $\pi / 2$ (right). The source is located at the origin of Cartesian coordinate system. The lateral coordinate r denotes the radial distance. The model parameters are $\upsilon_{P0} = 3km / s$, $\upsilon_{n1} = 2.846km / s$, $\upsilon_{n2} = 3.29km / s$, $\eta_1 = 0.28$, $\eta_2 = 1.67$, $\eta_3 = 0.23$, $A_{P0} = 0.025$ (corresponding to quality factor equal to 20), $\varepsilon_{Q1} = 0.66$, $\delta_{Q1} = 0.52$, $\varepsilon_{Q2} = -0.33$, $\delta_{Q2} = 0.98$, and $\delta_{Q3} = 0.94$.
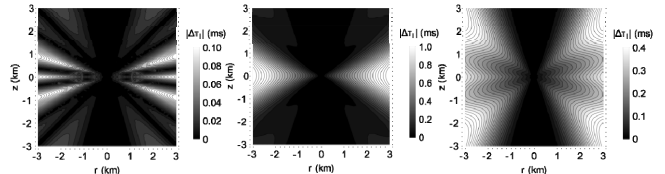

Figure 2. Similar to Figure 1, but for the imaginary part of the complex-valued traveltime.
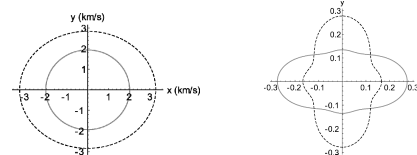
Figure 3. The azimuthal variation of the NMO velocities (left) and anellipticities (right) for t_R (dashed black lines) and t_I / A_{P0} (solid gray lines).

Inversion of P-wave VSP traveltimes in homogeneous weakly and moderately anisotropic media

Ivan Pšenčík[1] and Bohuslav Růžek[1]

[1]*Institute of Geophysics, Acad.Sci. of CR, Boční II, 141 31 Praha 4, Czech Republic*

1 Introduction

We study if, under what conditions, and to which extent, it is possible to retrieve information about weak to moderate anisotropy from P-wave traveltime data, assuming homogeneity of an anisotropic medium. We consider a vertical seismic profiling (VSP) experiment, which provides a good angular illumination of the medium. The use of the weak-anisotropy parameterization of the model reduces to 15 the number of the so-called weak-anisotropy (WA) parameters describing the most general P-wave anisotropy. We study effects of traveltime approximation, varying noise level and the experiment configuration on the quality of the recovery of the WA parameters. We show that the used parameterization of the model allows even the reconstruction of the phase-velocity surface of the studied medium.

2 Inversion formula

Our inversion scheme is based on the simplifying assumption that the ray-velocity $\mathbf{v}(\mathbf{N})$ and phase-velocity $\mathbf{c}(\mathbf{n})$ vectors are equal. Here $\mathbf{N}$ and $\mathbf{n}$ are *ray* and *phase* vectors, unit vectors parallel to the ray- and phase-velocity vectors. In this approximation the squared ray velocity $v(\mathbf{N})$ reads (Pšenčík and Farra, 2005):

$$\alpha_0^2\Big(1 + 2(\epsilon_x N_1^4 + \epsilon_y N_2^4 + \epsilon_z N_3^4 + \delta_x N_2^2 N_3^2 + \delta_y N_1^2 N_3^2 + \delta_z N_1^2 N_2^2)$$
$$+4[(\epsilon_{15}N_3 + \epsilon_{16}N_2)N_1^3 + (\epsilon_{24}N_3 + \epsilon_{26}N_1)N_2^3 + (\epsilon_{34}N_2 + \epsilon_{35}N_1)N_3^3$$
$$+(\chi_x N_1 + \chi_y N_2 + \chi_z N_3)N_1 N_2 N_3]\Big) = v^2(\mathbf{N}) = c^2(\mathbf{n}) = r^2/t^2 \ . \tag{1}$$

Here, ϵ_x, ϵ_y, ϵ_z, δ_x, δ_y, δ_z, χ_x, χ_y, χ_z, ϵ_{15}, ϵ_{16}, ϵ_{24}, ϵ_{26}, ϵ_{34} and ϵ_{35} are the sought WA parameters and N_i are components of the known ray vector $\mathbf{N}$, specifying the source-receiver direction. α_0 is the P-wave velocity of a reference isotropic medium. It is introduced to define the WA parameters, equation (1) is *independent* of α_0. If the ray velocity $v(\mathbf{N})$ is asumed to be known, linear inversion can be used, if the source-receiver distance r and traveltime t are assumed to be known, non-linear inversion must be used.

3 Synthetic tests

We consider a homogeneous model of tilted orthorhombic symmetry. Two VSP configurations are considered with sources on the surface distributed along profiles or randomly. In each of these configurations, we calculate exact traveltimes using the program package ANRAY (Gajewski and Pšenčík, 1990). These traveltimes with added Gaussian noise are used in equation (1) for the inversion of WA parameters. Figure 1 shows results of such an inversion for the profile (left) and random (right) distribution of sources. Superiority of the random distribution of sources is clearly visible. In Figure 2, relative differences between estimated and exact values of phase-velocity surfaces are shown. The estimated values of the phase velocity $v(\mathbf{n})$ are obtained from equation (1) with estimated values of WA parameters (crosses in Figure 1). Again, superiority of the random distribution of sources is visible.

4 Conclusions

Although we use very rough approximation for the ray velocity, $v(\mathbf{N}) = c(\mathbf{n})$, the use of traveltime data with random noise leads to satisfactory estimates of WA parameters. As shown in the presented examples,

even tilted orthorhombic symmetry should be treated as general anisotropy. When weak-anisotropy approximation is used, it means that 15 P-wave WA parameters must be considered. Although based on the weak-anisotropy approximation, the inversion scheme can be used even for moderate anisotropy. Anisotropy of the above-presented medium was around 25%. The above tests indicate clear superiority of the random distribution of sources. Next planned steps are the generalization of the inversion scheme to inhomogeneous anisotropic media, estimates of the type of anisotropic symmetry from inverted WA parameters, use of the S waves in the inversion process.
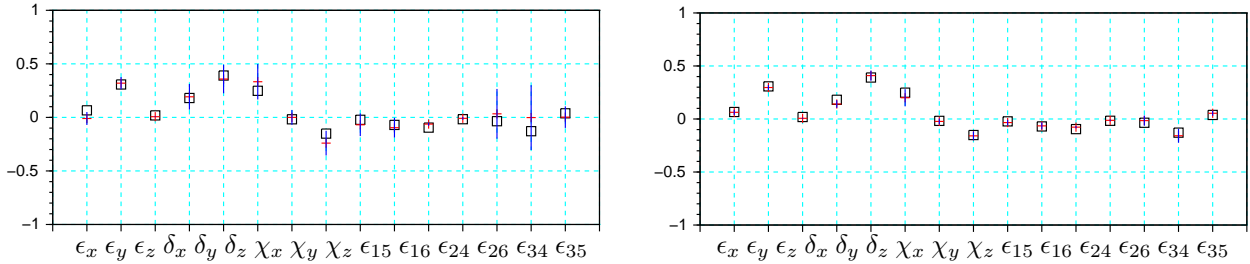

Figure 1: Results of the inversion of traveltimes with 0.005s noise generated by 50 sources distributed along 5 profiles (left) and randomly distributed (right) on the surface of the model, and recorded by 4 receivers in the borehole. Open squares: exact values of WA parameters, crosses: estimated values of WA parameters, error bars represent square roots of diagonal elements of the covariance matrix.
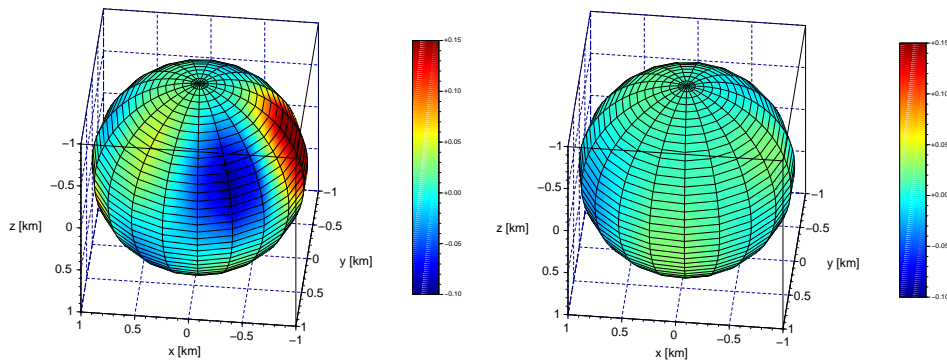

Figure 2: Relative differences between estimated (equation (1)) and exact phase velocity surfaces. WA parameters used in equation (1) are estimated from inverted traveltime data with 0.005s noise, generated by 50 sources distributed along 5 profiles (left) and randomly distributed (right) on the surface of the model.

Acknowledgements

References

Gajewski, D., and I. Pšenčík, 1990. Vertical seismic profile synthetics by dynamic ray tracing in laterally varying layered anisotropic structures. *J. Geophys. Res.*, **95**, 11301–11315.

Pšenčík, I., and Farra, V., 2005. First-order ray tracing for qP waves in inhomogeneous weakly anisotropic media. *Geophysics*, **70**, D65–D75.

Gradient computation for VTI acoustic wavefield tomography

Vladimir Li[1], Hui Wang[1], Ilya Tsvankin[1], Esteban Díaz[1] & Tariq Alkhalifah[2]
[1]*Center for Wave Phenomena, Colorado School of Mines*
[2]*King Abdullah University of Science and Technology*

SUMMARY

Wavefield tomography can handle complex subsurface geology better than ray-based techniques and, ultimately, provide a higher resolution. Here, we implement forward and adjoint wavefield extrapolation for VTI (transversely isotropic with a vertical symmetry axis) media using a generalized pseudospectral operator that employes a separable approximation of the P-wave dispersion relation. This operator is employed to derive the gradients of the differential semblance optimization (DSO) and modified image-power objective functions. We also obtain the gradient expressions for the data-domain objective function, which can incorporate borehole information necessary for stable VTI velocity analysis. These gradients are compared to the ones obtained with a space-time finite-difference (FD) scheme for a system of coupled wave equations. Whereas the kernels computed with the two wave-equation operators are similar, the pseudospectral method is not hampered by the imprint of the shear-wave artifact. Numerical examples also show that the modified image-power objective function produces cleaner gradients than the more conventional DSO operator.

SEPARABLE P-MODE APPROXIMATION

Anisotropic wavefield tomography is typically implemented under the pseudoacoustic assumption originally proposed by Alkhalifah (1998). Acoustic modeling in TI media can be performed with space-time FD schemes applied to coupled second-order equations (Fletcher et al., 2009). Generalized pseudospectral methods provide an alternative way to propagate only P-waves without the shear-wave artifacts. Separable P-mode dispersion-relation approximations for TI media are described in Du et al. (2014).

Pseudospectral methods are designed to evaluate the spatial wavefield derivatives in the wavenumber domain. Anisotropic extrapolation requires approximate dispersion relations with separable wavenumber and model-parameter terms. Employing the first-order Padé expansion, the P-wave separable dispersion relation for VTI media is obtained as (Schleicher and Costa, 2015):

$$\omega^2 = (1+2\varepsilon)V_{P0}^2 k_x^2 + V_{P0}^2 k_z^2 - 2(\varepsilon - \delta)V_{P0}^2 \frac{k_x^2 k_z^2}{k_x^2 + k_z^2}$$
$$\times \left[1 - 2\varepsilon \frac{k_x^2}{k_x^2 + k_z^2} + 2(\varepsilon - \delta) \frac{k_x^2 k_z^2}{(k_x^2 + k_z^2)^2}\right], \quad (1)$$

where k_z and k_x are the vertical and horizontal wavenumbers.

IMAGE-DOMAIN OBJECTIVE FUNCTIONS

Extended images are produced by retaining the correlation lags between the source and receiver wavefields in the output. The general imaging condition can be formulated as follows (Sava and Vasconcelos, 2011):

$$I(\mathbf{x}, \lambda, \tau) = \sum_{e,t} W_s(\mathbf{x} - \lambda, t - \tau) W_r(\mathbf{x} + \lambda, t + \tau), \quad (2)$$

where $I(\mathbf{x}, \lambda, \tau)$ is the extended image, W_s and W_r are the source and receiver wavefields, respectively, λ is the space lag, and τ is the time lag. Nonzero-lag energy can be used to update the migration velocity model by applying the DSO operator (Symes and Carazzone, 1991). For the horizontal space-lag extended image I, the DSO objective function has the form:

$$J_{DSO} = \frac{1}{2}\|\lambda_x \, I(x, z, \lambda_x)\|_{\ell_2}^2, \quad (3)$$

where λ_x is a penalty operator. Another commonly used (stack-power) objective function measures zero-lag energy:

$$J_{ST} = \frac{1}{2}\|I(x, z, \lambda_x = 0)\|_{\ell_2}^2. \quad (4)$$

Zhang and Shan (2013) propose a "partial" image power objective function that combines the criteria in equations 3 and 4 without the need to find optimal weights for J_{DSO} and J_{ST}:

$$J_{PST} = -\frac{1}{2}\|H(\lambda_x) I(x, z, \lambda_x)\|_{\ell_2}^2, \quad (5)$$

where H is a Gaussian operator centered at zero-lag.

GRADIENT COMPUTATION USING THE ADJOINT-STATE METHOD

Here, we employ the adjoint-state method (Plessix, 2006) to obtain the gradient expressions. For waveform inversion of reflection data, Alkhalifah and Plessix (2014) suggest to define the model vector as $\mathbf{m} = \{V_{\text{nmo}}, \eta, \delta\}$. The source- and receiver-side gradients of the partial image power objective function (equation 5) are found as:

$$\frac{\partial J}{\partial \delta} = \sum_{e,\tau} K(\tau) \frac{2V_{\text{nmo}}^2}{(1+2\delta)^2} k_z^2 u_i \star a_i$$

$$\frac{\partial J}{\partial \eta} = -\sum_{e,\tau} K(\tau) \, 2V_{\text{nmo}}^2 \frac{k_x^4}{k_x^2 + k_z^2} u_i \star a_i$$

$$\frac{\partial J}{\partial V_{\text{nmo}}} = -\sum_{e,\tau} K(\tau) 2V_{\text{nmo}} \left[k_x^2 u_i \star a_i + \frac{k_z^2}{1+2\delta} u_i \star a_i + \right.$$

$$\left. 2\eta \frac{k_x^4}{k_x^2 + k_z^2} u_i \star a_i\right], \, i = s, r,$$

$$(6)$$

where i denotes either the source or receiver side.
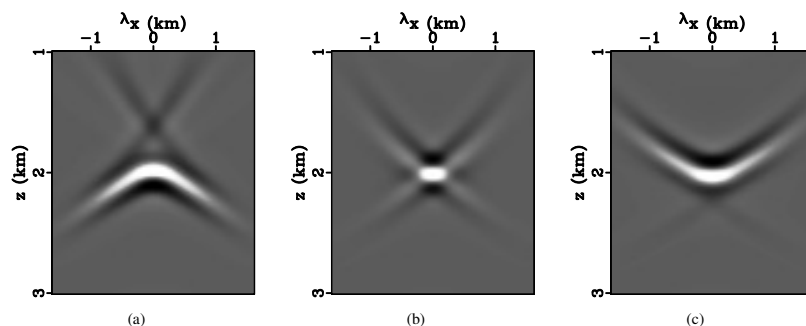
Figure 1: Space-lag CIGs for a horizontal VTI layer computed at $x = 4$ km using the pseudospectral extrapolator with (a) $\eta = 0$, (b) $\eta = 0.15$ (actual value), and (c) $\eta = 0.3$.
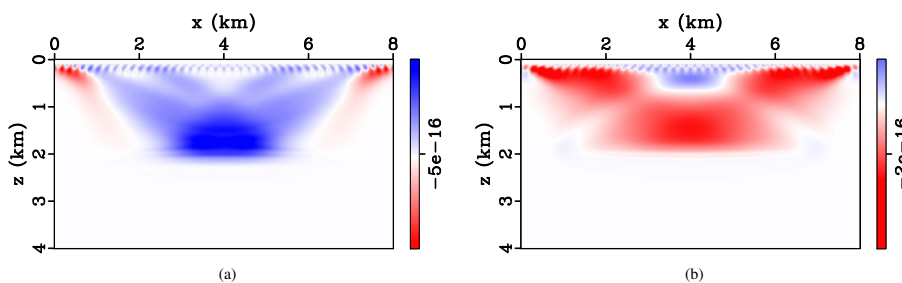

Figure 2: Gradients of the partial image-power function (equation 5) computed using the pseudospectral extrapolator for (a) $\eta = 0$ and (b) $\eta = 0.3$.

SYNTHETIC EXAMPLE

The medium parameters are specified on a rectangular grid, and the density is assumed to be constant. We compute the η-gradient in the image domain using reflection data. The model includes a horizontal interface beneath a homogeneous VTI layer with $V_{nmo} = 2$ km/s, $\eta = \delta = 0.15$, and a thickness of 2 km. We generate horizontal-space-lag extended images (Figure 1) and obtain the η-gradients for understated and overstated values of η. The η-errors induce residual energy in extended images (Figure 1) that has a linear ("V"-like) shape typical for near-horizontal interfaces (Sava and Alkhalifah, 2012; Li et al., 2015). Due to the aperture truncation, the extended images also contain considerable residual energy, which can introduce bias in the image-domain objective function and lead to false model updates.

The gradient of the DSO objective function for the understated η-field is strongly influenced by the kinematic artifacts in the extended image. The contribution of the artifact is even larger than that of the residual induced by the η-error because the artifact is located closer to the physical sources and receivers. The partial-image power objective function (equation 5) significantly reduces the influence of the artifact and produces cleaner gradients (Figure 2).

REFERENCES

Alkhalifah, T., 1998, Acoustic approximations for processing in transversely isotropic media: Geophysics, **63**, 623–631.

Du, X., P. J. Fowler, and R. P. Fletcher, 2014, Recursive integral time-extrapolation methods for waves: A comparative review: Geophysics, **79**, T9–T26.

Fletcher, R. P., X. Du, and P. J. Fowler, 2009, Reverse time migration in tilted transversely isotropic (TTI) media: Geophysics, **74**, WCA179–WCA187.

Li, V., I. Tsvankin, and T. Alkhalifah, 2015, 102, *in* Analysis of RTM extended images for VTI media: 519–524.

Plessix, R.-E., 2006, A review of the adjoint-state method for computing the gradient of a functional with geophysical applications: Geophysical Journal International, **167**, 495–503.

Sava, P., and T. Alkhalifah, 2012, Anisotropy signature in extended images from reverse-time migration: SEG, Technical Program Expanded Abstracts, 1–6.

Sava, P., and I. Vasconcelos, 2011, Extended imaging conditions for wave-equation migration: Geophysical Prospecting, **59**, 35–55.

Schleicher, J., and J. C. Costa, 2015, A separable strong-anisotropy approximation for pure qp wave propagation in TI media, *in* SEG Technical Program Expanded Abstracts: 685, 3565–3570.

Symes, W. W., and J. J. Carazzone, 1991, Velocity inversion by differential semblance optimization: Geophysics, **56**, 654–663.

Zhang, Y., and G. Shan, 2013, 937, *in* Wave-equation migration velocity analysis using partial stack-power maximization: 4847–4852.

Numerical Ray Tracing in 1D Triclinic Layered Media

Igor Ravve* and Zvi Koren, Paradigm Geophysical

Summary

We present practical aspects of numerical ray tracing for pure-mode and converted waves in 1D triclinic layered media. Tilted Orthorhombic (TOR) layer parameters are internally transformed into triclinic parameters. The model parameters are assumed piecewise-constant, and there is no need to solve differential equations. Starting with a given reflection point, we first solve the forward "shooting" problem: For a given opening angle between the incidence and reflection phase velocities, and a slowness azimuth, we compute the surface offset, its azimuth and the traveltime. We then solve the inverse "two-point ray tracing" problem, where for a given surface offset and its azimuth, we find the subsurface opening angle, the phase azimuth and the traveltime.

Introduction

We consider triclinic anisotropic layers which can also be obtained from, for example, Tilted Orthorhombic (TOR) layers. TOR medium is defined by nine elastic properties of the medium and three orientation parameters, which may be Euler angles of successive rotation ZYZ. Elastic properties are normally specified in the local orthorhombic (ORT) frame of reference and include compressional velocity v_P along local x_3 axis, parameter $f = 1 - v_{S\chi}^2 / v_P^2$, where $v_{S\chi}$ is the "vertical" shear velocity polarized in local x_1, and seven Thomsen-style parameters $\delta_1, \delta_2, \delta_3, \varepsilon_1, \varepsilon_2, \gamma_1, \gamma_2$. By applying the Bond (1943) transform, we rotate the stiffness matrix from the local to global axes, resulting with 21 elastic coefficients (triclinic anisotropic layers). First, we split the opening angle in two parts: incident and reflected. For a medium where the reflection plane is not the plane of symmetry, these two angles are not equal even for pure-mode wave. The opening angle yields also the horizontal slowness. Note that for a given ray pair, the horizontal slowness and its azimuth are the same for all layers of the package. Next, for each layer, we compute the slowness surface $p_3(p_1, p_2)$. This surface and its partial derivatives make it possible to compute the Cartesian components of the ray velocity which, in turn, yield the contribution of this layer into the two offset components and the traveltime. The layers are passed twice: for up-going and down-going waves. We consider all six types of waves: pure-mode P, S1 and S2, and converted P-S1, P-S2 and S1-S2, where S1 and S2 are fast and slow shear, respectively, i.e., we distinguish two shears by the magnitudes of their phase velocities rather than by their polarization. The inverse "two-point ray tracing" problem is solved numerically by Newton method.

Splitting of Opening Angle

The opening angle γ_{phs} is defined as that between the phase velocity (or slowness) directions of the incidence and reflection rays at a given subsurface point on a reflection surface. From Snell's law, both of them and the normal to the reflection surface are in the same plane, so that

$$\theta_{\text{phs}}^{\text{in}} + \theta_{\text{phs}}^{\text{re}} = \gamma_{\text{phs}} \qquad . \tag{1}$$

where $\theta_{\text{phs}}^{\text{in}}$ and $\theta_{\text{phs}}^{\text{re}}$ are the incidence and reflection angles, respectively. The two rays are assumed emerging from the reflection point. Thus, their azimuths differ by π. The azimuth of the reflection ray is ψ_{phs}, and the azimuth of the incidence ray is $\psi_{\text{phs}} + \pi$. Due to Snell's law, the horizontal slowness p_h of the two rays is identical,

$$\frac{\sin\theta_{\text{phs}}^{\text{in}}}{v_{\text{phs}}^{\text{in}}\left(\theta_{\text{phs}}^{\text{in}}, \psi_{\text{phs}} + \pi\right)} = \frac{\sin\theta_{\text{phs}}^{\text{re}}}{v_{\text{phs}}^{\text{re}}\left(\theta_{\text{phs}}^{\text{re}}, \psi_{\text{phs}}\right)} = p_h \qquad . \tag{2}$$

Eventually, we compute the Cartesian components of horizontal slowness, which are identical for all layers,

$$p_1 = p_h \cos\psi_{\text{phs}} \ , \qquad p_2 = p_h \sin\psi_{\text{phs}} \qquad . \tag{3}$$

Slowness Surface

The Slowness surface is a continuous function that defines the vertical slowness component given two horizontal components, $p_3(p_1, p_2)$. It is defined by the eigenvalue equation of Christoffel matrix for a triclinic medium with 21 independent stiffness coefficients, where the magnitude and the direction of the phase velocity are replaced by,

$$v_{\text{phs}}^2 = \frac{1}{p_1^2 + p_2^2 + p_3^2} \ , \quad n_i = \frac{p_i}{\sqrt{p_1^2 + p_2^2 + p_3^2}} \qquad . \tag{4}$$

The vanishing determinant "explodes" in 950 monomials which can be grouped by identical powers of p_1, p_2, p_3, and this leads to only 50 coefficients that depend on the stiffness components alone. The vertical slowness is given by a sixth-order polynomial equation,

$$A_6 p_3^6 + A_5 p_3^5 + A_4 p_3^4 + A_3 p_3^3 + A_2 p_3^2 + A_1 p_3 + A_0 = 0 \ , \tag{5}$$

where the coefficients A_k depend on p_1, p_2, except A_6 which is constant. Equation 5 may have up to six real roots,

Numerical Ray Tracing in 1D Triclinic Layered Media

or one or more complex conjugate pairs. As the horizontal slowness increases, first the P-wave roots become evanescent, then S1 and finally S2. The number of real roots is always even, where in each pair there is a root corresponding to up-going and down-going waves. Most often vertical slowness of the up- and down-going waves has different signs, but there may be also a case with the two roots of the same sign that belong to the same wave type. Still, one of them is up-going and another down-going. The corresponding vertical components of the ray velocity will necessarily have opposite signs. To compute the ray velocity components, we will need also derivatives of the slowness surface,

$$\frac{\partial p_3}{\partial p_i} = -\frac{\frac{\partial A_5}{\partial p_i}p_3^5 + \frac{\partial A_4}{\partial p_i}p_3^4 + \frac{\partial A_3}{\partial p_i}p_3^3 + \frac{\partial A_2}{\partial p_i}p_3^2 + \frac{\partial A_1}{\partial p_i}p_3 + \frac{\partial A_0}{\partial p_i}}{6A_6 p_3^5 + 5A_5 p_3^4 + 4A_4 p_3^3 + 3A_3 p_3^2 + 2A_2 p_3 + A_1}$$

$$i = 1,2 \tag{6}$$

The computation of the coefficient's derivatives A_k is straight forward as they are polynomials of p_1, p_2. Roots of the smallest slowness magnitude correspond to P-wave, medium to S1 shear and largest to S2.

Ray Velocity, Offset and Traveltime

The slowness surface and its derivatives yield the ray velocity components (Grechka et al., 1997),

$$v_{\text{ray},1} = \frac{-\partial p_3 / \partial p_1}{p_3 - p_1 \cdot \partial p_3 / \partial p_1 - p_2 \cdot \partial p_3 / \partial p_2} ,$$

$$v_{\text{ray},2} = \frac{-\partial p_3 / \partial p_2}{p_3 - p_1 \cdot \partial p_3 / \partial p_1 - p_2 \cdot \partial p_3 / \partial p_2} , \tag{7}$$

$$v_{\text{ray},3} = \frac{1}{p_3 - p_1 \cdot \partial p_3 / \partial p_1 - p_2 \cdot \partial p_3 / \partial p_2} .$$

We consider both rays emerging from the reflection point, so they both may be considered up-going, provided we take in account that their phase azimuths differ by π. After the ray velocity is computed we find the one-way contributions of the given layer into the offset and traveltime,

$$\frac{h_i}{\Delta z} = \frac{v_{\text{ray},i}^{\text{re}}}{v_{\text{ray},3}^{\text{re}}} , \quad \frac{t}{\Delta z} = \frac{1}{v_{\text{ray},3}^{\text{re}}} , \quad i = 1,2 \quad , \tag{8}$$

where Δz is the layer thickness.

Inversion: Two-Point Ray Tracing

The inverse two-point ray tracing problem considers that the offset components are specified while the opening angle, the phase azimuth and the traveltime are to be found. We solve a set of two nonlinear equations by Newton method, where the right sides of the equations are the offset components, and the unknowns are the opening angle and the slowness azimuth. Before the inversion, we perform a

forward shooting for a large number of rays (given their γ_{phs} and ψ_{phs}), and we record the offset components of the nodes on the surface. The take-off angles are discretized with a spherical spiral nodes (Koren and Ravve, 2012), where γ_{phs} and ψ_{phs} of the ray pairs change continuously along a 1D line on the spherical surface, and equal areas on the sphere are related to each spiral node. Next we apply Delaunay triangulation, and the surface nodes become vertices of the triangles. To find the initial guess for a given offset h_1, h_2, we find the triangle that contains this point inside and the area coordinates l_1, l_2, l_3, $l_1 + l_2 + l_3 = 1$. The latter are then used as weights for the linear interpolation. The convergence of the two-point ray tracing is relatively fast for pure-mode P-waves and slower for P-S1 and P-S2 converted waves. For pure-mode S1 and S2 or converted wave S1-S2, the convergence is rather slow, and more rays have to be shot for the initial guess. Still, the numerical simulations show that for shear waves, there may be shadow zones or poorly illuminated regions even for 1D layered triclinic medium.

Synthetic Example

We prepared a synthetic example for 10-layer TOR model with specified layer properties, thickness and orientation angles, and we computed forward (shooting) and inverse (two-point) ray tracing for pure-mode P and converted P-S1, P-S2 and S1-S2 waves. We do not list the table with the layer properties and the simulation results as they are too long for this abstract.

Conclusions

We developed and tested a method for forward (shooting) and inverse (two-point) numerical ray tracing in 1D TOR and triclinic layered media for all types of pure-mode and converted waves.

References

Bond, W., Jan. 1943, The mathematics of the physical properties of crystals, The Bell System Technical Journal, 1-72.

Grechka, V., I. Tsvankin, and J. Cohen, 1997, Generalized Dix equation and analytic treatment of normal-moveout velocity for anisotropic media: SEG Expanded Abstracts, 1246-1249.

Koren, Z., and I. Ravve, 2012, System and method for full azimuth angle domain imaging in reduced dimensional coordinate systems, Patent US 8120991B2.

Vector imaging of the decomposed elastic wave modes for 3D heterogeneous TI media

Jiubing Cheng* and Chenlong Wang, School of Ocean and Earth Science, Tongji University

SUMMARY

3D seismic imaging of multicomponent data involves many complexities and challenges, especially in anisotropic media. We discuss a vector imaging approach that honors the elastic effects of 3D primary reflections in heterogeneous transverseley isotropic (TI) media. Elastic reverse-time migration (ERTM) examples will demonstrate the validaty and advantages of this approach.

INTRODUCTION

Seismic waves propagate through the earth media as a superposition of compressional (P) and shear (S) waves. Recording both wave modes through multicomponent seismic acquires more information related to rock properties and thus allows better subsurface imaging and reservoir characterization. As the industry turns towards higher-risk conventional and unconventional hydrocarbon reservoirs, multicomponent seismic shall play more significant role than before.

Generally, multicomponent data are separated into single mode seismograms and then processed as scalar and acoustic pressure fields. This may lose significant information that indicates lithology and fluid properties due to ignoring some important elastic effects and unsuccessful P/S separation. Elastic Kirchhoff and wave-equation migration have shown some promise (Kuo and Dai, 1984; Sun and McMechan, 1986). However, the cross-talks of different body-wave modes make it challenging to obtain physically interpretable images, unless mode decoupling is achieved before imaging. Based on the theory of Helmholtz decomposition, the propagating elastic waves are generally separated into scalar P-wave and vector S-wave fields using divergence and curl operators, e.g., Xie and Wu (2005); Yan and Sava (2008). Nevertheless, the inconformity of the separated P and S modes causes difficulties for imaging the converted waves, especially in 3D cases. To exploit the decoupled P and S modes, Du et al. (2014) suggested a scalarization of the vector S-wave fields, and Duan and Sava (2015) suggested a vectorization of the scalar P-wave fileds. These operations are also necessary to correct polarity reversal on the images of the converted waves.

Generally, anisotropic P- and S-waves don't polarize parallel or perpendicular to wave vector. So, decoupling the wave modes involves more complexities in anisotropic media. Dellinger and Etgen (1990) presented anisotropic P/S separation in propagating elastic waves using divergencelike and curllike operators. Their method had been extended to obtain pure-mode scalar and vector fields for each mode in TI media(Yan and Sava, 2009; Zhang and McMechan, 2010). Fast algorthims have been presented to improve the efficiency of mode separation for heterogeneous TI media (Cheng and Fomel, 2014). Based upon these progresses, Wang et al. (2015, 2016) presented new scalar and vector imaging conditions for the decou-

pled wave modes in heterogeneous TI media. Here we supplement some physical insights for the vector imaging condition and demonstrate its advantages with 3D synthetic examples.

METHODOLGY

As shown in Figure 1, we confine our discussion to P-wave incidence, although the approach works for S-wave or mixed-mode incidence. The converted SV-wave in the TI layer will split into two S (S1 & S2) modes with different phase velocities when it leaves the local interface. For a successful ERTM, mode decoupling is a prerequisite to obtain physically interpretable images. The far-field body-waves can be separated into pure modes according to their polarization directions (Dellinger and Etgen, 1990; Zhang and McMechan, 2010). Unlike the well-behaved P mode, the S modes do not consistently polarize as a function of the propagation direction in anisotropic media. For TI media, however, they can be designated as SV and SH waves, which have consistent polarization, except in the direction of symmetry-axis (Winterstein, 1990).

We first decompose the propagated wavefields into single-mode vector fileds using (Cheng and Fomel, 2014):

$$\mathbf{u}_m(\mathbf{x}) = \int e^{i\mathbf{k}\mathbf{x}} \mathbf{a}_m(\mathbf{x},\mathbf{k})[\mathbf{a}_m(\mathbf{x},\mathbf{k}) \cdot \tilde{\mathbf{u}}(\mathbf{k})]d\mathbf{k}, \quad m \in \{P, SV, SH\},$$
(1)

in which $\mathbf{k}$ denotes the wave vector, $\tilde{\mathbf{u}}(\mathbf{k})$ represents the total elastic wavefield in wavenumber-domain, $\mathbf{a}_m(\mathbf{x},\mathbf{k})$ stands for the normalized polarization vector, and $\mathbf{u}_m(\mathbf{x})$ the decomposed vector field of the given mode at spatial location $\mathbf{x}$. We solve the Christoffel equation to get the polarization vector of P-wave, and then obtain the polarization vectors of SV and SH modes using the P-SV-SH polarization orthogonality. Polar angle-based tapering is also applied to mitigate the kiss singularity (Yan and Sava, 2012).

Then we apply a cross-correlation imaging condition to the decomposed source and receiver wavefields in vector form:

$$I_{mn}(\mathbf{x}) = \frac{1}{\gamma} \int_0^{t_{max}} [\mathbf{u}_m^s(\mathbf{x},t) \cdot \mathbf{u}_n^r(\mathbf{x},t)]dt,$$
(2)

with the scale factor γ given by

$$\gamma = \int_0^{t_{max}} [\mathbf{e}_m^s(\mathbf{x},t) \cdot \mathbf{e}_n^r(\mathbf{x},t)][\mathbf{u}_m^s(\mathbf{x},t) \cdot \mathbf{u}_m^s(\mathbf{x},t)]dt,$$
(3)

to balance the migration amplitudes. $\mathbf{e}_m^s$ and $\mathbf{e}_n^r$ denote the unit polarization vectors of the source and receiver wavefields, $\mathbf{u}_m^s$ and $\mathbf{u}_m^s$, respectively.

Because the mode decomposition preserves the amplitude, phase and polarization of P and S components as the total elastic wavefields, this vector imaging condition produces more accurate images for all reflected waves. Thanks to the polarity information from the polarizations of the decoupled incident and reflected waves, this imaging condition naturally avoids polarity reversal for converted wave imaging.

# Vector imaging of the decoupled elastic waves
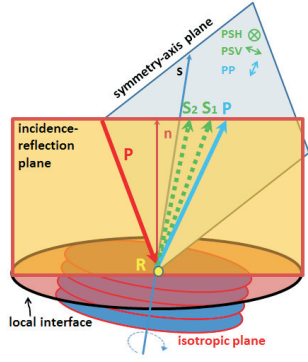
Figure 1: Reflected elastic waves of pure P-wave incidence at a local interface in a 3D TI media. Vectors **s** and **n** denote the symmetry axis and interface normal. Note that the SV and SH modes polarize in and orthogonal to the symmetry-axis plane, respectively.

EXAMPLES

A small three-layer VTI model is used to demonstrate the 3D vector imaging approach. The first layer is a homogeneous VTI medium with $v_{p0} = 2000$ m/s, $v_{s0} = 1328$ m/s, $\varepsilon = 0.05$, $\delta = 0.03$ and $\gamma = 0.02$. The second is a homogeneous isotropic medium, with $v_p = 2300$ m/s and $v_s = 1628$ m/s. The third is also a homogeneous VTI medium, with $v_{p0} = 2600$ m/s, $v_{s0} = 1928$ m/s, $\varepsilon = 0.10$, $\delta = 0.06$ and $\gamma = 0.04$. On the surface, we trigger nine exploding sources symmetrically distributed like a 3×3 array around the center with a minimum offset of 50*m*. iFor ERTM, we image the reflected PP, PSV and PSH waves, with the help of efficient mode decomposition algorithm (Cheng and Fomel, 2014). Despite of the artifacts due to the aperture limitation and imcomplete boundary condition, this algorithm produces good images for all primary reflections. We will demonstrate other examples including the application to 3D horizontal transversely isotropic (HTI) models on the conference.

CONCLUSION

Accurate and efficient mode decomposition helps us to obtain high-quality ERTM results for all primary reflections in anistropic media. The vector imaging condition produce more accurate migrated images and automatically avoid polarity reversal for imaging of the converted waves. This anisotropic ERTM approach shows good potential for full-wave imaging, anisotropic velocity analysis, and reservoir charactorization.

ACKNOWLEDGEMENTS

(a) psvv

(b) pshv

(c) psvsum

(d)

(e)
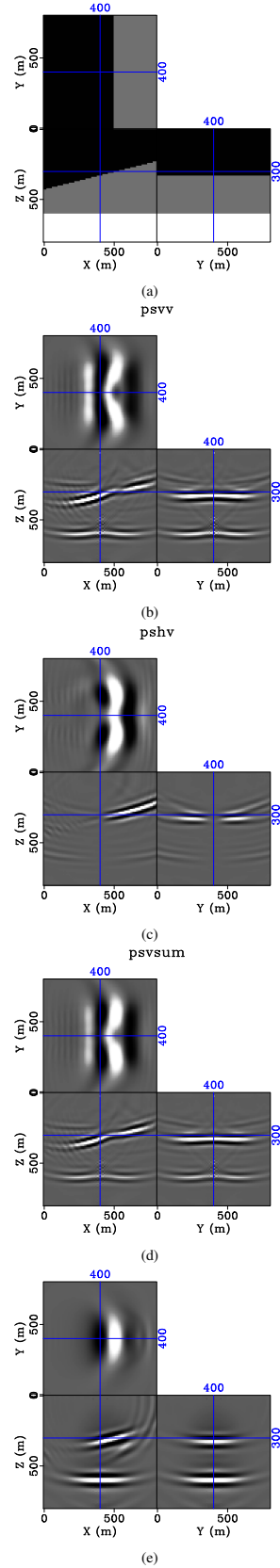
Figure 2: ERTM of a three-layer VTI model: (a) geometry of the model; (b) PSV, (c) PSH, (d) PS and (e) PP images.

17th International Workshop on Seismic Anisotropy

Vector imaging of the decoupled elastic waves

REFERENCES

Cheng, J. B., and S. Fomel, 2014, Fast algorithms of elastic wave mode separation and vector decomposition using low-rank approximation for anisotropic media: Geophysics, **79**, C97–C110.

Dellinger, J., and J. Etgen, 1990, Wavefield separation in two-dimensional anisotropic media: Geophysics, **55**, 914–919.

Du, Q., X. Gong, M. Zhang, Y. Zhu, and G. Fang, 2014, 3d ps-wave imaging with elastic reverse-time migration: Geophysics, **79**, S173–S184.

Duan, Y., and P. Sava, 2015, Scalar imaging condition for elastic reverse-time migration: Geophysics, **80**, S127–S136.

Kuo, J., and T. Dai, 1984, Kirchhoff elastic wave migration for the case of noncoincident source and receiver: Geophysics, **49**, 1223–1238.

Sun, R., and G. A. McMechan, 1986, Pre-satck reverse-time migration for elastic waves with application to synthetic offset vertical seismic profiles: Proceesings of the IEEE, **74**, 457–465.

Wang, C., J. Cheng, and A. B., 2015, Imaging condition for converted waves based on decoupled elastic wave modes: , 85rd Annual International Meeting, SEG, Expanded Abstracts, ?

Wang, C. L., J. B. Cheng, and B. Arntsen, 2016, Scalar and vector imaging based on wave mode decoupling for elastic reverse time migration in isotropic and TI media: Geophysics, acceptence pending.

Winterstein, D. F., 1990, Velocity anisotropy terminology for geophysicists: Geophysics, **55**, 1070–1088.

Xie, X. B., and R. S. Wu, 2005, Multicomponent prestack depth migration using the elastic screen method: Geophysics, **70**, S30–S37.

Yan, J., and P. Sava, 2008, Isotropic angle-domain elastic reverse-time migration: Geophysics, **73**, S229–S239.

———, 2009, Elastic wave-mode separation for VTI media: Geophysics, **74**, WB19–WB32.

———, 2012, Elastic wave mode separation for tilted transverse isotropic media: Geophysical prospecting, **60**, 29–48.

Zhang, Q., and G. A. McMechan, 2010, 2d and 3d elastic wavefield vector decomposition in the wavenumber domain for vti media: Geophysics, **75**, D13–D26.

69